

Master Thesis

Radiation Shielding Analysis of
Martian Regolith Simulant MGS-1
and Polymers

K. Johnson

Master Thesis

Radiation Shielding Analysis of Martian Regolith Simulant MGS-1 and Polymers

by

K. Johnson

to obtain the degree of Master of Science
at the Delft University of Technology,
to be defended publicly on Tuesday, November 30, 2021 at 02:00 PM.
at the Delft University of Technology.

Student number:	4279557		
Project duration:	May 31, 2021 – November 30, 2021		
Thesis committee:	Dr. A. Menicucci,	TU Delft,	Main supervisor
	Dr. Y. Tang,	TU Delft,	Supervisor
	Prof.dr. E.K.A. Gill,	TU Delft,	Committee chair
	Dr. D.M. Stam,	TU Delft,	External examiner

An electronic version of this thesis is available at <http://repository.tudelft.nl/>.

Cover image from *ESA, 2014* (cropped).

Preface

This thesis concludes my master Space Flight at the Aerospace Engineering faculty of the Technical University of Delft. Although space radiation was a fairly new topic to me when I started my thesis, I became genuinely interested in it. It is a fascinating topic that should be recognized and talked about more, certainly in light of the accelerated plans to send humans to the Moon and Mars, even considering colonization at some point. I have truly enjoyed working on this topic and I am eager to see what is next.

I would like to thank my supervisors, Alessandra and Yinglu. They have given me great support and advice based on their knowledge and expertise. I really appreciate our weekly meetings where I felt a sincere interest in what I did. I would also like to thank Kunal Masania and the Shaping Matter Lab research group for letting me use the filament maker and providing me with tools and materials. I also greatly appreciate the assistance of Lucas Biesterveld from 3devo, who has helped me solve many encountered issues with the filament maker. Lastly, I want to express my deep and sincere thanks to my girlfriend and parents in particular. You have all supported me, not only during my thesis, but throughout my whole time as a student. I would not be standing here without all of your help and support. I am grateful to have you by my side.

Kim Johnson
Delft, November 2021

Abstract

This document outlines the analysis of radiation dose reduction of the Mars Global Simulant (MGS-1) and various polymers. The dose reduction is derived from the measured dose of a detector in a shielded and unshielded situation, and represents how much radiation is absorbed by the shield. First, the integral fluxes of all particles impinging on the Martian surface are determined, including secondary radiation neutrons. Using OLTARIS (NASA, 2010), short for On-Line Tool for the Assessment of Radiation in Space, and based on the Galactic Cosmic Rays (GCR) flux during the five past solar minima in 1965, 1977, 1987, 1997 and 2010, the average contribution to the total integral flux experienced on the Martian surface for neutrons is 82.10%, 16.98% for protons, 0.88% for helium and 0.04% for heavy ions. The particle contributions during 11 historical Solar Particle Events (SPE) are also determined, but the dose reduction is analysed for the GCR case, which is simulated using the FLUKA (Fluktuierende Kaskade) software. The dose reduction from monochromatic 740 MeV neutron and 1 GeV proton, helium, carbon, oxygen, silicon and iron beams is assessed for shield thicknesses up to 400 cm. The performance of MGS-1 is analyzed with respect to 17 polymers, liquid hydrogen, water, aluminium and lead. MGS-1 dose reductions were in line with several polymers, confirming the applicability of MGS-1 and Martian regolith as a radiation shielding material. Assessing different density values of an MGS-1 shield concluded that higher densities for thick shields have significantly higher dose reductions. For the MGS-1 bulk density of 1.29 g/cm³, the dose reductions are 51.15%, 82.38%, 99.75%, 93.53%, 95.59%, 97.92% and 99.09% for neutrons, protons, helium, carbon, oxygen, silicon and iron, respectively. For the reported density of 2.49 g/cm³, this is respectively 91.80%, 99.22%, 99.97%, 99.28%, 99.50%, 99.76% and 99.89%. The inclusion of a polymer middle or inner layer to the MGS-1 shield only lead to marginal gains in dose reduction and are thus not significantly beneficial. However, an inner polymer layer could contribute to the absorption of harmful lower energy neutrons.

Next, a half-spherical habitat with a 250 cm MGS-1 shield is used to assess a simplified GCR case during a solar minimum that is the average of the five aforementioned historical GCR cases. The absorbed dose is measured from three water detectors, called phantoms. These represent the human body and are placed in the habitat center, further from the center and near to the habitat wall. Radiation beams with the energy spectra of the chosen particles from OLTARIS are applied to the habitat and resulting dose reductions for all phantoms are above 95%, even close to 100% for the selected heavy ions. Combining all selected particle types results in a dose reduction per day of 98.28% for the phantom in the center, 93.31% for the phantom near the wall and 96.79% for the phantom further from the center. Expressed in normalized dose, which is the dose of the detector in the shielded situation divided by the unshielded one, this is $0.0172 \pm 1.81\%$, $0.0669 \pm 2.29\%$ and $0.0324 \pm 2.14\%$, respectively. Values lower than 1 indicate a reduction, while values higher than 1 indicate a dose increase.

Lastly, a composite 3D printing filament, consisting of PLA (Polylactic Acid) polymer pellets and sieved MGS-1 particles, was successfully produced. An average concentration of ~88.3wt% and ~11.7wt% for PLA and MGS-1 was attained, respectively, but varied locally throughout the filament. Density measurements of different filament segments lead to values of 1.24 g/cm³, 1.36 g/cm³, 1.39 g/cm³ and 1.52 g/cm³ for higher MGS-1 concentrations, respectively. At high MGS-1 concentrations, the filament became very fragile and prone to breaking. From the composite filament, samples were successfully 3D printed using an FDM (Fused Deposition Modeling) printer, which confirmed the feasibility of producing the filament, as well as 3D printing with it. However, additional research is required to develop methods that increase the filament density, while retaining its structural integrity. Furthermore, polymer samples of PETG (Polyethylene Terephthalate, Glycol modified), PLA and LCP (Liquid Crystal Polymer) were 3D printed, with varying the layer height and material flow that is extruded by the nozzle. The densities decreased significantly when the material flow was decreased and generally, all samples had lower densities than the filament itself. When the layer height was increased, little to no changes in density were observed. Over-extruding the material, by increasing the material flow, may lead to higher densities, which is preferred for a radiation shield. However, more research is required in the context of density effects associated with scaling up 3D printing for the construction of habitats.

Contents

List of Figures	ix
List of Tables	xii
List of Acronyms	xii
1 Introduction	1
1.1 Research Objective and Research Questions	1
1.2 Report Outline	2
2 Simulation Methodology	3
2.1 FLUKA Software and Flair GUI	3
2.1.1 Brief Introduction to FLUKA	3
2.2 Verification of the FLUKA Software by Plot Comparisons	5
2.3 Comparing Different Primaries and Seeds in FLUKA.	7
3 Article Draft	11
4 Additive Manufacturing of an MGS-1/Polymer Composite	51
4.1 Rationale for Additive Manufacturing of the Composite	51
4.2 Preparation	51
4.3 Filament Making and 3D Printing	53
4.4 Effect on Filament Density of Different Print Settings for Polymers	54
5 Conclusions and Recommendations	57
5.1 Conclusions.	57
5.2 Recommendations	59
A MGS-1 Fact Sheet	63
B Dose Reduction Tables for Varying Number of Primaries and Seeds	65
C Dose Reduction Tables for All Assessed Materials	69
D Dose Reduction Plots for All Assessed Materials for Varying Shield Thicknesses	77
E Dose Reduction Plots for All Assessed Materials for Varying Area Densities	81
F Dose Reduction Tables for an MGS-1 Shield	85

List of Figures

2.1	Representation of FLUKA in the flair GUI.	4
2.2	ASCII file example of one cycle of a simulation run.	4
2.3	Comparison between BNL measured data (<i>Brookhaven National Laboratory, n.d.</i>) and FLUKA simulations for (a),(b) protons, (c),(d) carbon and (e),(f) iron monochromatic radiation beams. The relative LET versus shield thickness is plotted for (a),(c) and (e) while the relative absorbed dose is plotted for (b),(d) and (f). LET and absorbed dose are relative to the first observed value with zero shield thickness.	6
2.4	Comparison between plots from Durante and Cucinotta, 2011 and FLUKA simulations for (a),(b) silicon, (c),(d) chlorine, (e),(f) titanium and (g),(h) iron monochromatic radiation beams. All plots are normalized to the first observed absorbed dose at shield depth = 0 g/cm ²	7
2.5	Dose reduction from a 500 MeV monochromatic neutron beam for an MGS-1 shield with 1.29 g/cm ³ density and a thickness range of 0-400 cm for 5k, 10k and 50k primaries.	8
2.6	Dose reduction from a 500 MeV monochromatic neutron beam for an MGS-1 shield with 1.29 g/cm ³ density and a thickness range of 0-400 cm for different randomized seeds.	9
2.7	Close-up of the dose reduction from a 500 MeV monochromatic neutron beam for an MGS-1 shield with 1.29 g/cm ³ density and a thickness range of 0-100 cm for different randomized seeds.	9
4.1	(a) 3D printing of a Martian habitat (<i>AI SpaceFactory, 2019</i>) and (b) collecting Martian regolith (<i>NASA, 2020</i>).	51
4.2	(a) The <i>NEXT 1.0 - advanced</i> filament maker (<i>3devo, 2021</i>) and (b) a Prusa MK2 FDM printer.	52
4.3	(a) The <i>Haver EML Digital Plus</i> sieve shaker and (b) the three MGS-1 batches after sieving.	52
4.4	(a) Sieved MGS-1 particles and PLA pellets, and (b) the produced MGS-1/PLA composite filament.	53
4.5	(a) Different concentrations of MGS-1 and PLA as derived by the color, and (b) filament strands with differing concentrations to measure the density, ranging from low (S1) to high (S4) MGS-1 weight fractions.	53
4.6	Successfully 3D printed samples using the MGS-1/PLA filament.	54
4.7	(a) All 3D printed sample cubes and filament strands with labels in accordance with Tables 4.2 and 4.3. Samples A1-4 and B1-4 are PETG, samples C1-4 and D1-4 are PLA, and sample E1-4 is LCP. (b) The <i>Mettler Toledo AB204-S</i> density meter using Archimedes' principle for measuring the cube samples.	55
4.8	(a) Top view of the cubic samples with indicated print features and (b) 3D printed LCP samples with labels in accordance with Table 4.3.	56
A.1	Fact sheet (January 2021) of Martian regolith simulant MGS-1 (<i>ExolithLab, 2020</i>).	64
D.1	The dose reduction (%) with respect to shield thickness (cm) for (a),(b),(c),(d) 740 MeV neutron and (e),(f),(g),(h) 1 GeV proton beams.	78
D.2	The dose reduction (%) with respect to shield thickness (cm) for 1 GeV (a),(b),(c),(d) helium and (e),(f),(g),(h) carbon beams.	79
E.1	The dose reduction (%) with respect to area density (g/cm ²) for (a),(b),(c),(d) 740 MeV neutron and (e),(f),(g),(h) 1 GeV proton beams.	82
E.2	The dose reduction (%) with respect to area density (g/cm ²) for 1 GeV (a),(b),(c),(d) helium and (e),(f),(g),(h) carbon beams.	83

List of Tables

2.1	Dose reduction of an MGS-1 shield with a thickness range of 20-400 cm for 5k, 10k and 50k primaries.	8
4.1	Measured densities, based on Archimedes' principle, of the MGS-1/PLA filament strands.	54
4.2	Measured density values of the PETG and PLA 3D printed samples. The density is expressed in g/cm^3	55
4.3	Measured density values of the LCP 3D printed samples. The density is expressed in g/cm^3	56
B.1	Effect of the number of primaries and different seeds for 500 MeV neutron beams on the dose reduction of an MGS-1 shield with 1.29 g/cm^3 density and a thickness range of 20-200 cm. 5k, 10k and 50k represents 5000, 10000 and 50000 primaries, respectively, while s1-5 denotes different randomized seeds. D_{norm} is the normalized dose, $E_{D_{\text{norm}}}$ is the error of the normalized dose and δD is the dose reduction.	66
B.2	Effect of the number of primaries and different seeds for 500 MeV neutron beams on the dose reduction of an MGS-1 shield with 1.29 g/cm^3 density and a thickness range of 220-400 cm. 5k, 10k and 50k represents 5000, 10000 and 50000 primaries, respectively, while s1-5 denotes different randomized seeds. D_{norm} is the normalized dose, $E_{D_{\text{norm}}}$ is the error of the normalized dose and δD is the dose reduction.	67
C.1	Dose reduction from 740 MeV neutron beams of all assessed materials with a shield thickness range of 20-100 cm. D_{norm} is the normalized dose, $E_{D_{\text{norm}}}$ is the error of the normalized dose and δD is the dose reduction.	70
C.2	Dose reduction from 740 MeV neutron beams of all assessed materials with a shield thickness range of 120-200 cm. D_{norm} is the normalized dose, $E_{D_{\text{norm}}}$ is the error of the normalized dose and δD is the dose reduction.	71
C.3	Dose reduction from 1 GeV proton beams of all assessed materials with a shield thickness range of 20-100 cm. D_{norm} is the normalized dose, $E_{D_{\text{norm}}}$ is the error of the normalized dose and δD is the dose reduction.	72
C.4	Dose reduction from 1 GeV proton beams of all assessed materials with a shield thickness range of 120-200 cm. D_{norm} is the normalized dose, $E_{D_{\text{norm}}}$ is the error of the normalized dose and δD is the dose reduction.	73
C.5	Dose reduction from 1 GeV helium beams of all assessed materials with a shield thickness range of 20-100 cm. D_{norm} is the normalized dose, $E_{D_{\text{norm}}}$ is the error of the normalized dose and δD is the dose reduction.	74
C.6	Dose reduction from 1 GeV carbon beams of all assessed materials with a shield thickness range of 20-100 cm. D_{norm} is the normalized dose, $E_{D_{\text{norm}}}$ is the error of the normalized dose and δD is the dose reduction.	75
F.1	Effect of the density for 740 MeV neutron and 1 GeV proton, helium, carbon, oxygen, silicon and iron beams on the dose reduction of an MGS-1 shield with a thickness range of 20-100 cm. D_{norm} is the normalized dose, $E_{D_{\text{norm}}}$ is the error of the normalized dose and δD is the dose reduction.	86
F.2	Effect of the density for 740 MeV neutron and 1 GeV proton, helium, carbon, oxygen, silicon and iron beams on the dose reduction of an MGS-1 shield with a thickness range of 120-200 cm. D_{norm} is the normalized dose, $E_{D_{\text{norm}}}$ is the error of the normalized dose and δD is the dose reduction.	87

F.3	Effect of the density for 740 MeV neutron and 1 GeV proton, helium, carbon, oxygen, silicon and iron beams on the dose reduction of an MGS-1 shield with a thickness range of 220-300 cm. D_{norm} is the normalized dose, $E_{D_{\text{norm}}}$ is the error of the normalized dose and δD is the dose reduction.	88
F.4	Effect of the density for 740 MeV neutron and 1 GeV proton, helium, carbon, oxygen, silicon and iron beams on the dose reduction of an MGS-1 shield with a thickness range of 320-400 cm. D_{norm} is the normalized dose, $E_{D_{\text{norm}}}$ is the error of the normalized dose and δD is the dose reduction.	89

List of Acronyms

ABS	Acrylonitrile Butadiene Styrene
ALARA	As Low As Reasonably Achievable
ASA	Acrylonitrile Styrene Acrylate
BLEO	Beyond Low-Earth Orbit
BNL	Brookhaven National Laboratory
CERN	European Organization for Nuclear Research ¹
CME	Coronal Mass Ejections
COC	Cyclic Olefin Copolymer
ESA	European Space Agency
FDM	Fused Deposition Modeling
FFF	Fused Filament Fabrication
flair	FLUKA Advanced Interface
FLUKA	Fluktuierende Kaskade
GCR	Galactic Cosmic Rays
GEANT4	Geometry And Tracking
GUI	Graphical User Interface
HETC-HEDS	High-Energy Transport Code-Human Exploration and Development in Space
HZE	High-energy protons and high charge (Z) and Energy nuclei
HZETRN	High Z and Energy Transport
ICRP	International Commission on Radiological Protection
JAXA	Japan Aerospace Exploration Agency
LArC	Langley Research Center
LCP	Liquid Crystal Polymer
LEO	Low-Earth Orbit
MC	Monte Carlo
MGS-1	Mars Global Simulant
MI	Material Index
MSL	Mars Science Laboratory
NASA	National Aeronautics and Space Administration

¹Originally: Conseil Européen pour la Recherche Nucléaire

NCRP	National Council on Radiation Protection and Measurements
NSRL	NASA Space Radiation Laboratory
OLTARIS	On-Line Tool for the Assessment of Radiation In Space
PC	Polycarbonate
PE	Polyethylene
PEEK	Polyether Ether Ketone
PEI	Polyetherimide
PEKK	Polyetherketoneketone
PET	Polyethylene Terephthalate
PHITS	Particle and Heavy Ion Transport code System
PI	Polyimide
PLA	Polylactic Acid
PMMA	Poly(methyl methacrylate
POM	Polyoxymethylene
PP	Polypropylene
PS	Polystyrene
PVC	Polyvinyl Chloride
RAD	Radiation Assessment Detector
REID	Risk of Exposure Induced Death
SEM	Standard Error of the Mean
SPE	Solar Particle Events
TID	Total Ionizing Dose
WSL	Windows Subsystem for Linux

Introduction

With the acceleration of planned human mission initiatives to Mars, the space radiation environment is one of the biggest challenges to face. Until now, most human space missions took place in an orbit around Earth where they are protected by the magnetosphere and atmosphere against adverse space radiation, with the exception of the relatively short lunar missions by the Apollo program. Outside of these spheres, space radiation manifests itself to its fullest extent as well as on the Martian surface where the surface and atmosphere even induce detrimental secondary radiation. The need for radiation protection becomes more pressing than ever as mission duration times and radiation exposure will increase. Much research on these topics have been done and are ongoing, but there are still significant knowledge gaps. There is a need for more in-situ measurements to increase the accuracy and reliability of Martian radiation environment predictions. The introduction to the topic is documented more elaborately in the first section of the article draft in Chapter 3.

1.1. Research Objective and Research Questions

The research objective is stated as:

« to assess the radiation shielding properties of Martian regolith simulant MGS-1 and polymers by analyzing the dose reduction in terms of absorbed dose of the particle spectrum on the Martian surface during a galactic cosmic ray or solar particle event »

The research objective is supported by the following main research question:

What is the most feasible regolith simulant and polymer composite that results in maximal dose reduction of space radiation?

The main research question is subdivided into the following sub-questions:

- 1. How should the radiation shielding capability be assessed and verified?*
- 2. How is space radiation characterized and how should it be applied to the use case?*
- 3. How should the polymer selection process be carried out in terms of radiation shielding capabilities?*

Furthermore, two additional research questions are introduced regarding additive manufacturing of a polymer with MGS-1 by means of 3D printing:

- 4. How is the polymer chosen to be used as the filament for 3D printing?*
- 5. Which material properties of the 3D print are relevant and how are these evaluated?*

1.2. Report Outline

The remainder of the report is set out as follows:

- Chapter 2 discusses the FLUKA software as well as a brief description how it is used throughout the work. Additionally, the software is verified by comparing reproduced plots with two references.
- Chapter 3 presents an article draft that covers the main focus of this thesis, being the dose reduction analysis using Martian regolith simulants MGS-1 and polymers. In this chapter, Section 1 provides the introduction to the topic, discussing the radiation environment in space and on Mars, the biological radiation effects on humans and the protection as well as shielding against radiation. Section 2 specifies the preparations and collected data required for the simulations. The simulations and corresponding dose reduction results are outlined in Section 3, while the radiation shielding of a simplified Mars habitat is documented in Section 4. Lastly, conclusions and the main recommendation are given in Sections 5 and 6, respectively.
- Chapter 4 takes a closer look at additive manufacturing by means of 3D printing a produced composite filament consisting of MGS-1 regolith and PLA polymer.
- Chapter 5 provides the conclusions and recommendations related to the research questions.

2

Simulation Methodology

This chapter covers the methodology in terms of carrying out the FLUKA/flair simulations and how the resulting data is processed. This methodology is a brief explanation on how to work with the software. Furthermore, the influence of generated seeds and number of primaries is assessed, and the software is verified by comparing it with data and simulations from external sources.

2.1. FLUKA Software and Flair GUI

For the analysis of radiation dose reduction, simulations were performed using the FLUKA particle transport code developed by CERN (European Organization for Nuclear Research¹). In general, radiation transport code models are used to model the interactions between particles and matter that are either based on deterministic or Monte Carlo (MC) methods. Deterministic transport codes use Boltzmann transport equations and take atomic and nuclear collisions into account, that ultimately change the energy and type of the projectile species (*Durante and Cucinotta, 2011*). Deterministic transport codes are computationally less demanding but are usually limited to simple shielding geometries. MC methods are more complex transport codes that are computationally demanding. Besides FLUKA, other examples of transport codes are SHIELD, GEANT4, PHITS, HETC-HEDS for MC methods and HZETRN which uses a deterministic method.

2.1.1. Brief Introduction to FLUKA

FLUKA is well-known for radiation protection and detector simulation studies (*Schetakis et al., 2020*). It is used in conjunction with *flair* which is the Graphical User Interface (GUI) where amongst others, radiation beam types, geometries and materials can be specified, as well as carrying out simulations and obtaining many different types of results. Instead of referring to FLUKA and *flair* separately, FLUKA is used hereafter to refer to the use of FLUKA in the *flair* GUI. FLUKA is free for academic use and the FLUKA and *flair* versions used are 4.1-1 and 3.1-1.3, respectively. Installation is straightforward from the online documentation and can run on both Linux and Windows, which requires the Windows Subsystem for Linux (WSL).

After installation, the interface shown in Figure 2.1 is seen. From this figure, label A represents the five main tabs. The tabs required for setting up and running simulations are *Input*, *Geometry*, *Run* and *Plot*. *Input* is where all the information prior to the simulations is entered by means of *cards*. Examples of such *cards* are the geometry of the shield and Martian habitat, the particle type of the beam and its energy, the materials and composition of the structures and environment, and the radiation quantity (e.g. absorbed dose). FLUKA allows to add user-defined materials and composites such as Martian regolith simulant MGS-1, using the bulk chemistry shown in Appendix A.

¹Originally: Conseil Européen pour la Recherche Nucléaire

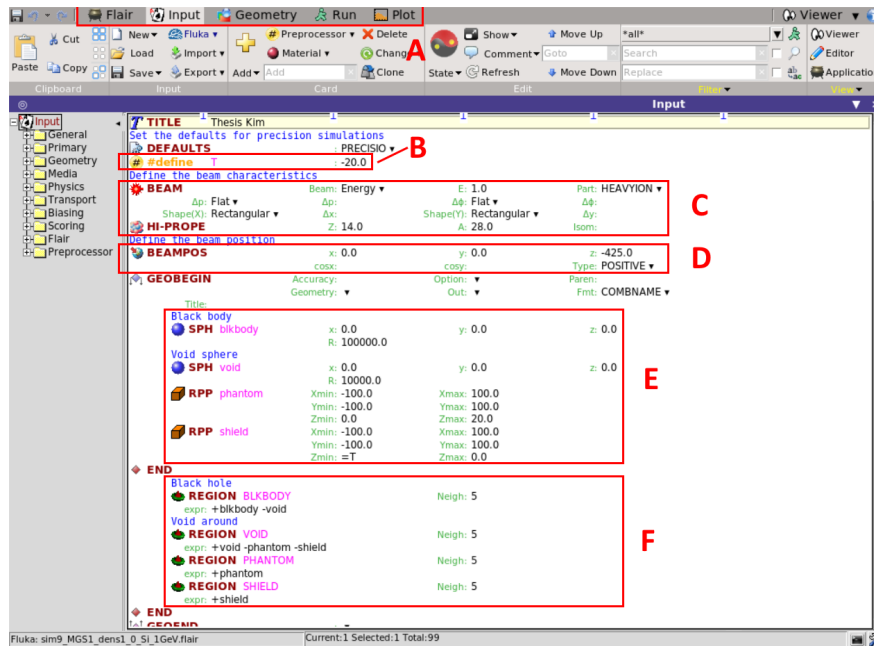


Figure 2.1: Representation of FLUKA in the flair GUI.

Once all the necessary input cards have been defined, simulations can be run. The number of cycles per simulation run is five by default. When all cycles and hence one simulation is completed, a file is created that contains all data points of the user-defined radiation quantity such that it can be plotted. Furthermore, another file is created that displays the value of the radiation quantity in a specified region for each cycle. Only the value of the selected radiation quantity is important and an example is highlighted in Figure 2.2. Since separate runs - each consisting of five cycles - are needed for every assessed variable (e.g. shield thickness, material, energy level, type of radiation particle, etc.), processing all these simulations is very time consuming. Based on the simulation configurations in Chapter 3, an example is given; if (i) seven particle types (neutrons, protons, helium, carbon, oxygen, silicon and iron) are assessed for (ii) a shield thickness between 20 cm and 400 cm in increments of 20 cm, for (iii) one material with two different densities, at (iv) one energy level and for (v) five cycles, means that $7 \times 20 \times 2 \times 1 \times 5 = 1400$ files are generated and must be retrieved. Retrieving these values manually is highly inefficient and for this reason a script was created using MS Excel Power Query which extracts only the necessary values from these runs. Consequently, the process becomes much more automated and time-saving. All values retrieved from MS Excel Power Query and the subsequent required calculations are consequently saved in MS Excel. The subsequent calculations are further elaborated in Section 2.1 of Chapter 3.

```

sim1_MGS1_dens1_29_pro_energies_400cm002_fort - Notepad
File Edit Format View Help

***** Thesis Kim *****

DATE: 10/25/21, TIME: 22:53:23

Total number of particles followed      10000, for a total weight of  1.0000E+04

1
Region  binning n.  2  "DoseAsc  ", generalized particle n.  228
  1 bins corresponding to the region sets:
from region  3 to region  3 in step of  1 regions, or
from region  0 to region  0 in step of  1 regions, or
from region  0 to region  0 in step of  1 regions
Data follow in an array A(ir), format (1(5x,1p,10(1x,e11.4)))

accurate deposition along the tracks requested
6.6857E-04

```

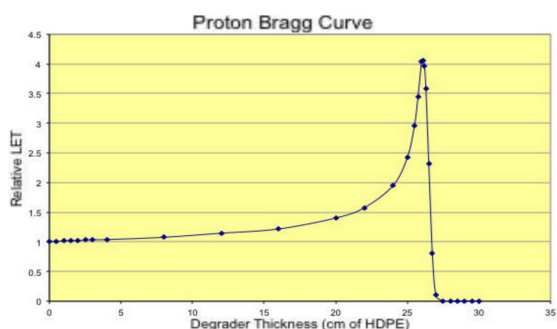
Figure 2.2: ASCII file example of one cycle of a simulation run.

If one wishes to get started with FLUKA, it is strongly recommended to make use of the available FLUKA exercises as this provides the necessary knowledge and experience. These exercises and corresponding lectures per topic can be found on [CERN Indico website](#). Furthermore, the [FLUKA User Forum](#), [FLUKA manual](#), [flair manual](#) and [documentation](#) can be consulted for help.

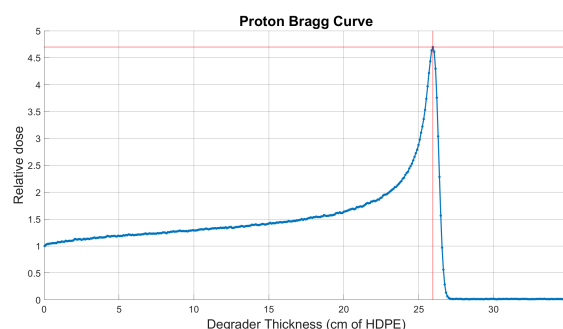
2.2. Verification of the FLUKA Software by Plot Comparisons

To check whether the FLUKA installation was successful and works as intended, several exercises of the given FLUKA documentation were made and compared with the given solutions and plots. These results matched those of the solutions and were the first confirmation that it was installed successfully. Furthermore, two independent external sources were found that contained sufficient information to recreate those in FLUKA, which are rather simple radiation beam and shield scenarios from *Brookhaven National Laboratory, n.d.* (BNL) and *Durante and Cucinotta, 2011*. This way, by recreating and comparing the FLUKA results with those from the references, the correct installment and operation of FLUKA verified.

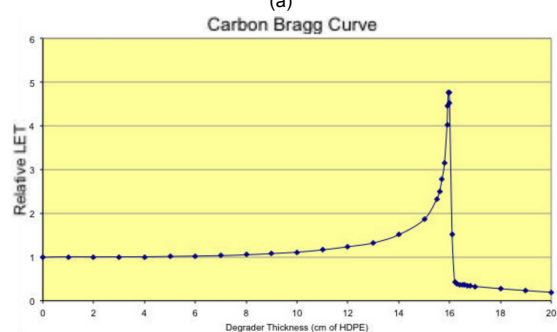
The BNL plots include monochromatic 205 MeV proton, 292.7 MeV carbon and 962.8 MeV iron beams as well as high-density polyethylene shields with a density of $\rho=0.97 \text{ g/cm}^3$ at given thicknesses. These plots are compared with the equivalent FLUKA runs in Figure 2.3. It can be seen that the shapes, which represent the propagation of the respective radiation beam through the shield, from the FLUKA and BNL plots are nearly identical. Also, the shield thickness at which the peak of the radiation propagation occurs is almost identical. This is $\sim 26 \text{ cm}$ for protons, $\sim 16 \text{ cm}$ for carbon and $\sim 25 \text{ cm}$ for iron. These characteristic peaks are called Bragg curves and are discussed in Section 3.3 of Chapter 3. Differences are observed in the y-values between the FLUKA and BNL plots, this could be partially because the BNL plots use another radiation quantity, being the relative LET (Linear Energy Transfer) normalized to water. For the FLUKA plots, the radiation quantity is the normalized absorbed dose (i.e. normalized to the first observed absorbed dose at zero shield thickness). These differences could also be related to statistical errors, as well as differences in used atomic weight of particles for example. Lastly, the differences can also be attributed to the software; where the BNL plots are based on actual measurements of the NASA Space Radiation Laboratory (NSRL), the FLUKA plots are a result from simulations. There are always differences between actual and simulated results, as can be seen in Figure 2.4 as well. However, most importantly is the shape of the radiation propagation in the shield which is almost identical as mentioned previously.



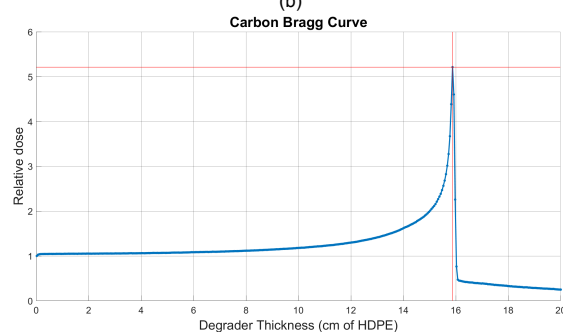
(a)



(b)



(c)



(d)

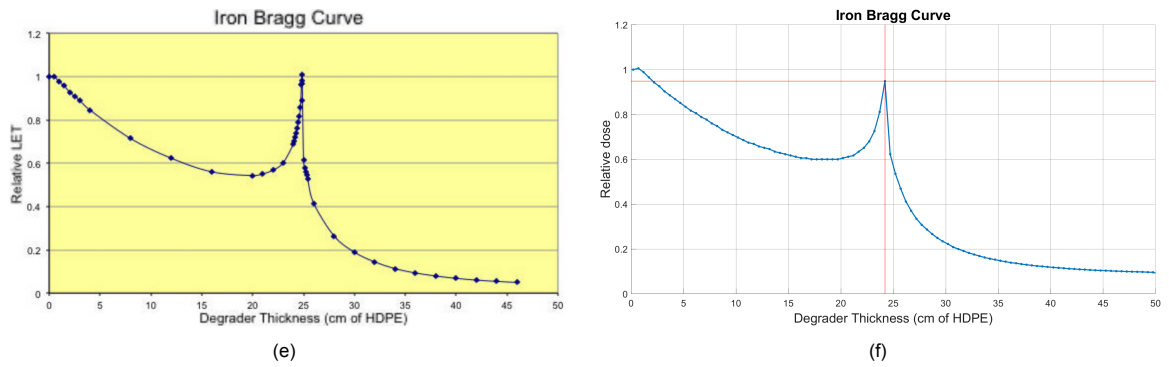
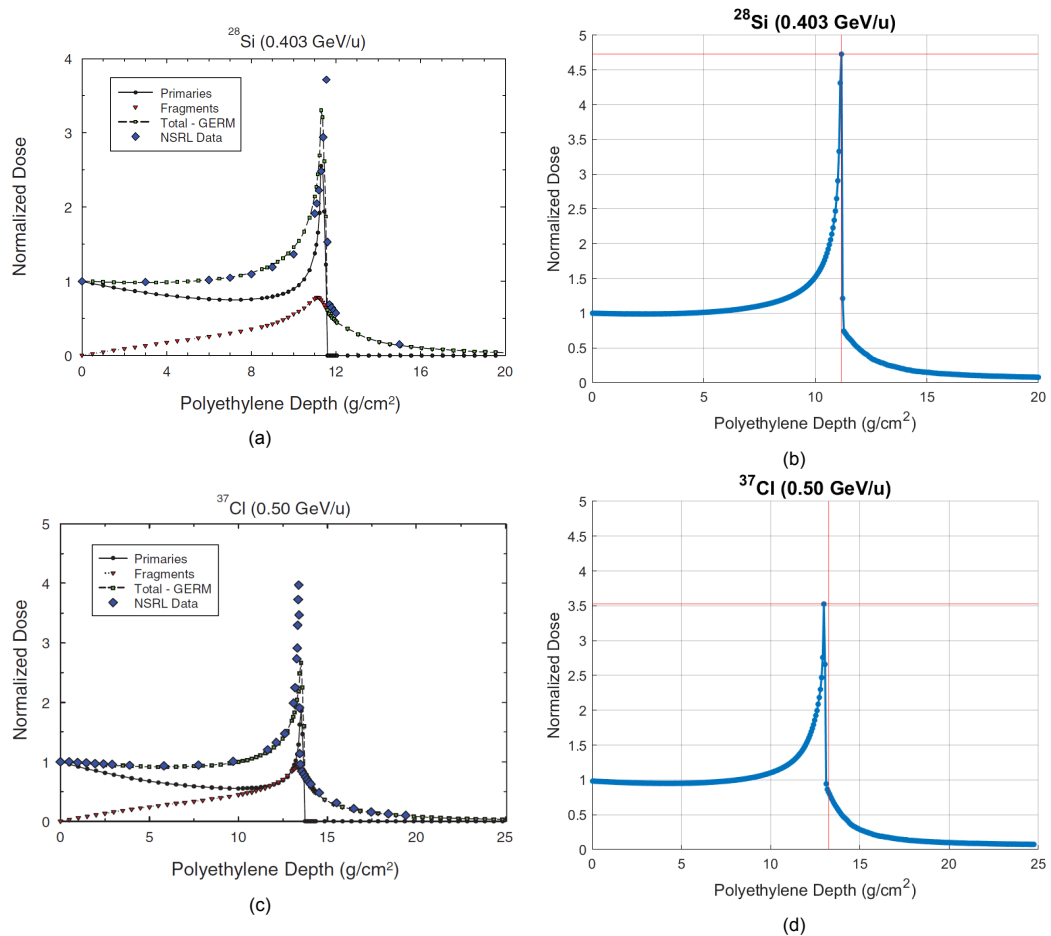


Figure 2.3: Comparison between BNL measured data (*Brookhaven National Laboratory, n.d.*) and FLUKA simulations for (a),(b) protons, (c),(d) carbon and (e),(f) iron monochromatic radiation beams. The relative LET versus shield thickness is plotted for (a),(c) and (e) while the relative absorbed dose is plotted for (b),(d) and (f). LET and absorbed dose are relative to the first observed value with zero shield thickness.

The comparison between FLUKA simulations and the second source is shown in Figure 2.4. Here, for the plots from *Durante and Cucinotta, 2011* themselves, a comparison was made between NSRL measurements and GERMCODE. GERMCODE is a Galactic Cosmic Ray (GCR) event-based risk model based on MC transport codes. Between these, differences in the height of the peaks are observed but the shapes are very similar. The radiation propagation through the shield is by means of normalized dose and polyethylene depth in g/cm^2 , which is achieved when the shield thickness is multiplied by its density. Although the peak coordinates differ slightly when comparing the FLUKA plots with those, the shapes are again almost identical. Following from these two different sources, the correct functioning of FLUKA is verified.



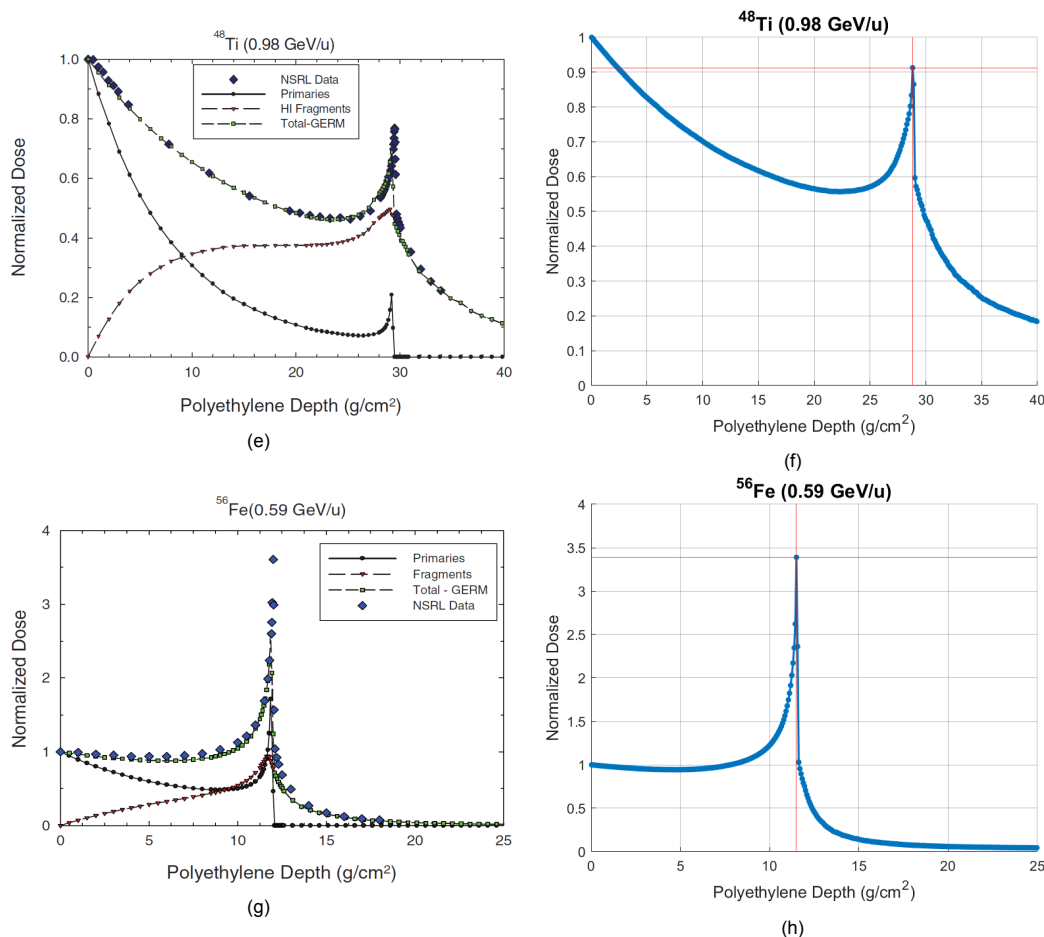


Figure 2.4: Comparison between plots from Durante and Cucinotta, 2011 and FLUKA simulations for (a),(b) silicon, (c),(d) chlorine, (e),(f) titanium and (g),(h) iron monochromatic radiation beams. All plots are normalized to the first observed absorbed dose at shield depth = 0 g/cm².

2.3. Comparing Different Primaries and Seeds in FLUKA

As mentioned before, FLUKA uses by default five cycles per run with 5,000 primaries, i.e. the defined number of particle beams. A minimum of five cycles is recommended such that a normal distribution is simulated correctly (Vlachoudis, 2008). Increasing the number of primaries also reduces the statistical error. In combination with this, the influence of a default or random seed is also investigated. A seed is a number that initializes a random number sequence used for the simulation runs (Ferrari et al., 2021). Runs using different seeds and different primaries are done with monochromatic 500 MeV neutron beams. When no specific seed is inserted by the user, FLUKA uses a default seed number of 54217137.

First, different numbers of primaries are assessed. These are the default value of 5,000 primaries, as well as 10,000 and 50,000 primaries. The dose reduction versus shield thickness of MGS-1 is shown in Figure 2.5. From this figure, it can be seen that the blue curve representing 5,000 primaries is positioned slightly above the others, especially for the first ~120 cm. The dose reductions for 10,000 and 50,000 primaries are quite similar. Table 2.1 shows the dose reduction of the same MGS-1 shield for all cases with increasing thickness. This table shows that the dose reduction values for 10k and 50k primaries are close to each other, while for 5k there is a slight offset. Concerning the corresponding error values, Appendix B shows that the errors for 50k primaries are smaller than for 10k and 5k primaries. Between the latter two, the differences are smaller. However, it is important to note that the dose reduction of 5k primaries is still more offset with respect to the other two.

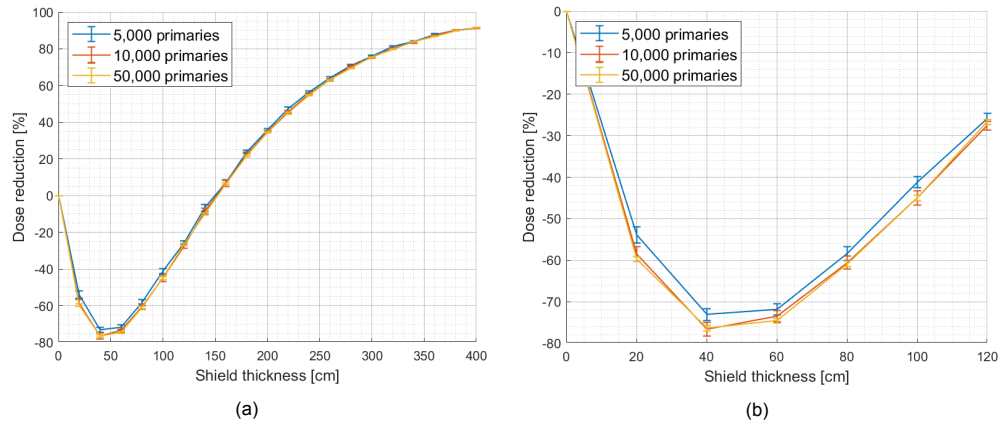
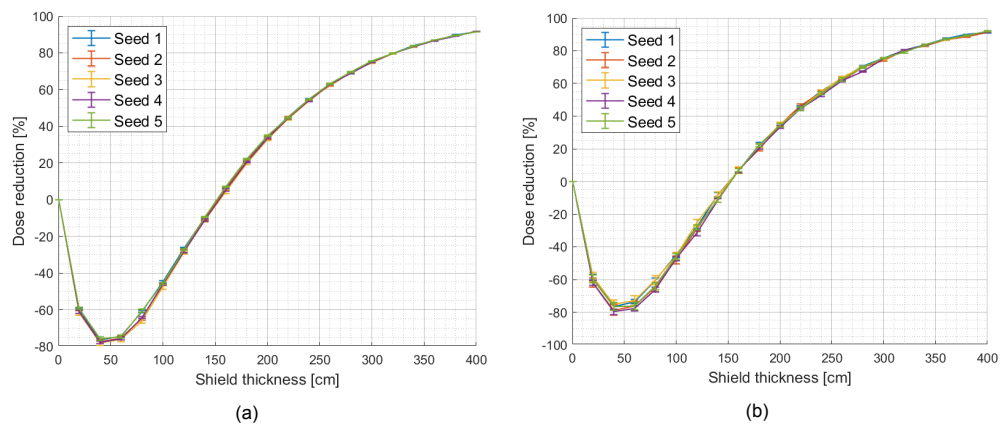


Figure 2.5: Dose reduction from a 500 MeV monochromatic neutron beam for an MGS-1 shield with 1.29 g/cm^3 density and a thickness range of 0-400 cm for 5k, 10k and 50k primaries.

Table 2.1: Dose reduction of an MGS-1 shield with a thickness range of 20-400 cm for 5k, 10k and 50k primaries.

Thickness [cm]	20	40	60	80	100	120	140	160	180	200
5k primaries	-54%	-73%	-72%	-58%	-41%	-26%	-7%	7%	24%	36%
10k primaries	-59%	-77%	-73%	-61%	-45%	-28%	-8%	7%	22%	35%
50k primaries	-60%	-76%	-75%	-61%	-45%	-27%	-10%	6%	22%	35%
Thickness [cm]	220	240	260	280	300	320	340	360	380	400
5k primaries	47%	56%	64%	71%	76%	81%	84%	88%	90%	91%
10k primaries	46%	55%	63%	71%	75%	80%	84%	87%	90%	91%
50k primaries	45%	55%	63%	69%	76%	80%	84%	87%	90%	91%

Furthermore, different seeds and their resulting dose reductions are also compared. Seed 1 represents the default FLUKA seed of 54217137. All other seeds are randomly selected creating a random value smaller than 9×10^8 . These randomly selected seeds are always unique, thus no two equal values are used. Random seed allocations are run for 5k, 10k and 50k primaries to see if the number of primaries also results in differing results. This is shown in Figures 2.6c, 2.6b and 2.6a respectively, while Figures 2.7c, 2.7b and 2.7a are close-ups of the first 100 cm of the shield. From these figures, it is seen that most of the different seeds do not result in considerable changes in dose reduction. Lower numbers of primaries, as well as using different random seeds, lead to bigger variations in dose reduction. This is observed especially in the first ~100 cm of the shield.



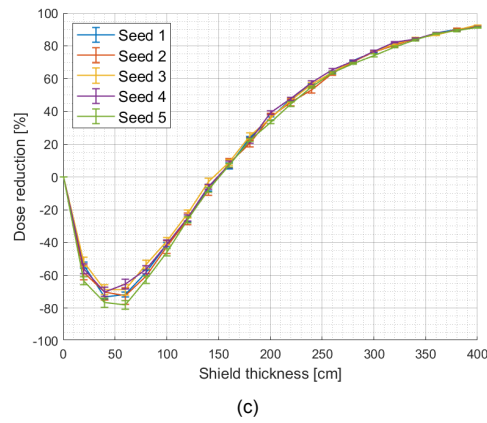


Figure 2.6: Dose reduction from a 500 MeV monochromatic neutron beam for an MGS-1 shield with 1.29 g/cm^3 density and a thickness range of 0-400 cm for different randomized seeds.

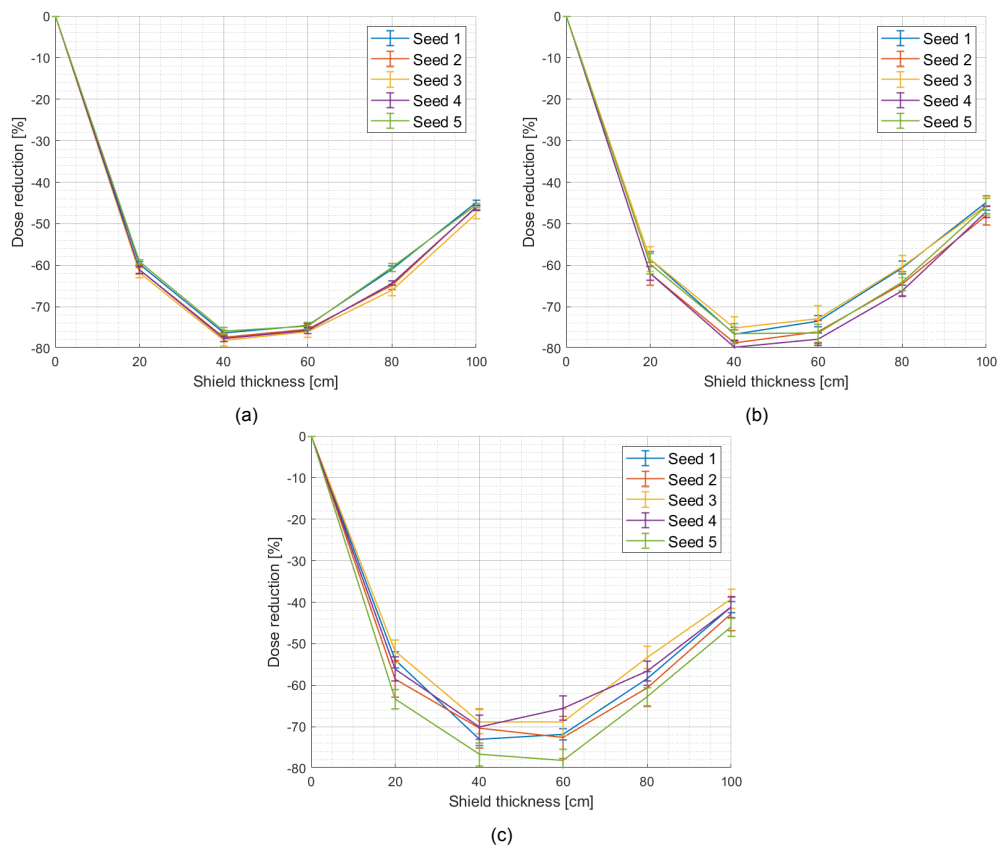


Figure 2.7: Close-up of the dose reduction from a 500 MeV monochromatic neutron beam for an MGS-1 shield with 1.29 g/cm^3 density and a thickness range of 0-100 cm for different randomized seeds.

From these results, it was decided to continue with 10k primaries for the reason that this is sufficiently close to 50k primaries runs because its differences are rather insignificant, due to the small statistical errors. Choosing 50k primaries significantly increases the required computational power as well as the simulation run times. Furthermore, randomizing the seed number does not change dose reduction results for 10k primaries to such an extent that these become unrepresentative. For this reason, the default seed number is used for all simulation runs, such that it can be recreated and compared in future work.

3

Article Draft

Radiation Shielding Analysis of Martian Regolith Simulant MGS-1 and Polymers

K. Johnson

Master thesis student, email: k.johnson@student.tudelft.nl

Department of Space Engineering, Section of Space Systems Engineering,
Delft University of Technology, Kluyverweg 1, 2629 HS Delft, The Netherlands

Abstract

This article outlines the analysis of radiation dose reduction of the Mars Global Simulant (MGS-1) and various polymers. The dose reduction is derived from the measured dose of a detector in a shielded and unshielded situation, and represents how much radiation is absorbed by the shield. First, the integral fluxes of all particles impinging on the Martian surface are determined, including secondary radiation neutrons. Using OLTARIS (NASA, 2010), short for On-Line Tool for the Assessment of Radiation in Space, and based on the Galactic Cosmic Rays (GCR) flux during the five past solar minima in 1965, 1977, 1987, 1997 and 2010, the average contribution to the total integral flux experienced on the Martian surface for neutrons is 82.10%, 16.98% for protons, 0.88% for helium and 0.04% for heavy ions. The particle contributions during 11 historical Solar Particle Events (SPE) are also determined, but the dose reduction is analysed for the GCR case, which is simulated using the FLUKA (Fluktuerende Kaskade) software. The dose reduction from monochromatic 740 MeV neutron and 1 GeV proton, helium, carbon, oxygen, silicon and iron beams is assessed for shield thicknesses up to 400 cm. The performance of MGS-1 is analyzed with respect to 17 polymers, liquid hydrogen, water, aluminium and lead. MGS-1 dose reductions were in line with several polymers, confirming the applicability of MGS-1 and Martian regolith as a radiation shielding material. Assessing different density values of an MGS-1 shield concluded that higher densities for thick shields have significantly higher dose reductions. For the MGS-1 bulk density of 1.29 g/cm³, the dose reductions are 51.15%, 82.38%, 99.75%, 93.53%, 95.59%, 97.92% and 99.09% for neutrons, protons, helium, carbon, oxygen, silicon and iron, respectively. For the reported density of 2.49 g/cm³, this is respectively 91.80%, 99.22%, 99.97%, 99.28%, 99.50%, 99.76% and 99.89%. The inclusion of a polymer middle or inner layer to the MGS-1 shield only lead to marginal gains in dose reduction and are thus not significantly beneficial. However, an inner polymer layer could contribute to the absorption of harmful lower energy neutrons. Next, a half-spherical habitat with a 250 cm MGS-1 shield is used to assess a simplified GCR case during a solar minimum that is the average of the five aforementioned historical GCR cases. The absorbed dose is measured from three water detectors, called phantoms. These represent the human body and are placed in the habitat center, further from the center and near to the habitat wall. Radiation beams with the energy spectra of the chosen particles from OLTARIS are applied to the habitat and resulting dose reductions for all phantoms are above 95%, even close to 100% for the selected heavy ions. Combining all selected particle types results in a dose reduction per day of 98.28% for the phantom in the center, 93.31% for the phantom near the wall and 96.79% for the phantom further from the center. Expressed in normalized dose, which is the dose of the detector in the shielded situation divided by the unshielded one, this is $0.0172 \pm 1.81\%$, $0.0669 \pm 2.29\%$ and $0.0324 \pm 2.14\%$, respectively. Values lower than 1 indicate a reduction, while values higher than 1 indicate a dose increase.

Keywords: radiation shielding, dose reduction, absorbed dose, galactic cosmic rays (GCR), solar particle events (SPE), FLUKA, Martian regolith, Mars global simulant (MGS-1)

1 Introduction

1.1 Radiation in space

Space radiation and its biological impact on humans is one of the greatest challenges to face (*Durante and Cucinotta, 2011*) in terms of human spaceflight and eventually colonization on the Moon and Mars. It poses a big threat and is becoming more pressing with the increased and accelerated efforts towards space exploration by national space agencies, private companies and industries. Space radiation is not

only hazardous to humans, but also to electronics and materials that could ultimately lead to degradation and failure in performance (Abuali Galehdari and Kelkar, 2016). The most adverse radiation is ionizing radiation, which possesses such high energies that it can remove electrons from atoms and result in increased positive charges of those atoms (NASA, 2019). This is because these unstable particles radiate high levels of energy in order to become stable again. Radiation in the heliosphere originates from two sources: Galactic Cosmic Rays (GCR) and Solar Particle Event(s) (SPE). The magnetosphere of the Earth shields almost all GCR (Genta, 2017) but also contains trapped particles, making it another source of radiation. The lack of an atmosphere on the Moon and the very thin atmosphere of Mars (Kading and Straub, 2015), which only offers minimal protection against space radiation (De Angelis et al., 2004), allows radiation to interact with the upper layers of the surface and the atmosphere, if present. These interactions of primary radiation with the surface and atmosphere induce secondary radiation, which mostly consists of neutrons.

GCR has its origins from outside the solar system, but primarily from within the Milky Way (Rais-Rohani, 2005) and are thought to be created by supernovae (Abuali Galehdari and Kelkar, 2016). The GCR composition is shown in Table 1. Estimating the energy range of GCR has always been challenging, which is explained by the differences between several sources: 10 MeV to 10 GeV according to Nambiar and Yeow, 2012, less than 1 MeV up to hundreds of TeV reported by Allkofer, 1975 and 10 MeV up to several TeV stated in NCRP, 1989.

Table 1: Composition of galactic cosmic rays.

Protons	Helium*	Heavy ions**	Source
87%	12%	1%	<i>Simpson, 1983</i>
91%	8%	1%	<i>Genta, 2017</i>
~89%	~9%	~2%	<i>Wilson et al., 1993</i>
85%	14%	1%	<i>Nambiar and Yeow, 2012</i>
*also called alpha particles			
**also called HZE ions, i.e. high (H) atomic number (Z) and energy (E)			

Table 1 shows that heavy ions, which are the heavier elements with atomic number $Z=3$ and higher, represent only 1% of the GCR flux. However, they should not be neglected because radiation from HZE ions has a high kinetic energy, is highly ionizing and penetrating, and causes extensive biological damage (Rapp, 2006; Rask et al., 2008a). The GCR flux has an anticorrelation with the periodic solar activity of about 11 years in the heliosphere (Norbury et al., 2019), meaning that the GCR intensity is highest when the solar activity is at a minimum. This is because the solar magnetic field is weakest at a solar minimum, resulting in less shielding of GCR particles (Rask et al., 2008a) and its radiation dose can differ 40% between a solar minimum and maximum (Berger et al., 2020).

An SPE occurs when charged particles are blasted into space as a result of sporadic major eruptions and explosions on the Sun, and mainly consists of electrons and protons. These events can either be solar flares or coronal mass ejections (CME), or combination of both. Solar flares are instantaneous events that excessively increase the radiation flux for a short period of time. Although SPE energies are lower than for GCR, they are still a considerable threat. There are also rare cases of extreme SPE where radiation fluxes become exceptionally high, which should not be ignored because they are harmful to astronauts (Guo et al., 2019), and usually one or two extreme SPE take place each solar cycle. Moreover, they are highly unpredictable and therefore increase the risk of hazardous consequences (Zeitlin and La Tessa, 2016). Unlike GCR, no clear relationship between solar activity and SPE has yet been found (Gabriel, 2000), but they appear to happen near solar maxima (Rapp, 2006).

As mentioned before, secondary radiation is the result of interactions between primary radiation with a planetary surface and atmosphere (Figure 1), but also with shields, habitat materials, etc. Secondary

radiation can easily pass through shields that are too thin and can consequently radiate inside habitats. Secondary neutrons can therefore cause extensive biological damage, potentially even more harmful to humans, materials and electronics than primary radiation (*Meurisse et al., 2020; Rask et al., 2008b*). They are uncharged particles that can penetrate deeply into materials and interact with atomic nuclei (*Cucinotta, 2014; Nambiar and Yeow, 2012*).

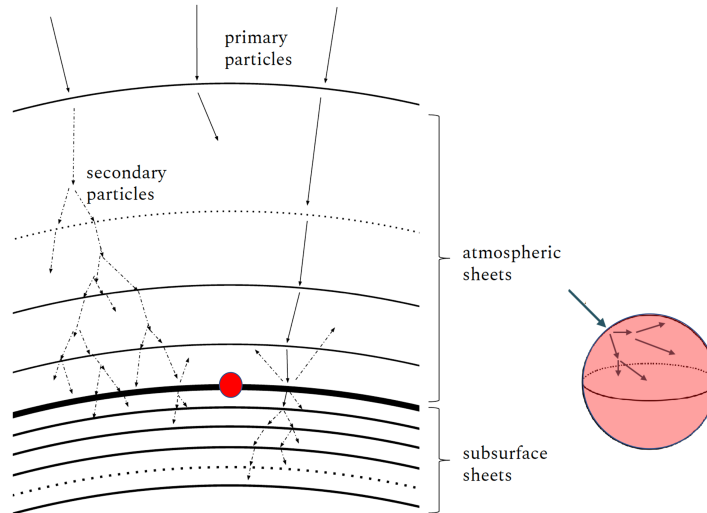


Figure 1: Propagation of secondary radiation as a result of interactions between primary radiation and the Martian surface and atmosphere (*Röstel et al., 2020*).

1.2 Effects of radiation on humans

Future human missions to the Moon and Mars will have longer mission times, meaning that astronauts will be longer exposed to space radiation without the protection of the magnetosphere and atmosphere of the Earth. Although research about space radiation has steadily increased in recent years, the biological effects of space radiation on the human body are not yet fully understood (*Chancellor et al., 2018*). This is partly due to the lack of experimental data outside the safe environment of the Earth. Long-term effects of space radiation beyond the magnetosphere and atmosphere of the Earth have not been sufficiently studied because of the lack of long-term human missions outside these spheres. Space agencies such as NASA, ESA and JAXA have specified career dose limits that represent the maximum amount radiation an astronaut can be exposed to during the career. For NASA, the career limit is based on Risk of Exposure Induced Death (REID); the total exposure to radiation must remain below 3% REID (*Cucinotta, Kim, Chappell, et al., 2013*). This value is determined in such a way that the exposure level of the astronaut remains below 3% of REID from a fatal cancer with a confidence level of 95% (*Cucinotta, Kim, and Ren, 2006; Mukherjee et al., 2017*). One limitation is that these career dose limits were originally established for Low-Earth Orbit (LEO) missions but are exactly the same for missions Beyond Low-Earth Orbit (BLEO) missions, as decided during the National Council on Radiation Protection and measurements (NCRP) in 2015. Recently, however, NASA and ESA recognized the need and began reassessing its radiation exposure limits as reported in *Niiler, 2021, Skibba, 2021* and *Walsh et al., 2019*. This emphasizes that the knowledge of space radiation effects on humans is in serious need of improvements and advances as pointed out by *McKenna-Lawlor et al., 2015* and *Chancellor et al., 2018*.

Some of the known consequences of radiation exposure for humans can be divided into two categories, being short and long-term effects. Short-term effects result from heavy exposure in a short period of time, for example during an SPE. This includes nausea, vomiting fatigue, central nervous system diseases, and impaired motor functionality and behaviour. Long-term effects are the result of prolonged radiation exposure and are more applicable to GCR. Such effects include higher risks of cancer, cataract, vision impairment and degenerative cardiac diseases (*Mars, 2018*). In terms of long missions and even permanent habitation on Mars and the Moon, these short and long-term effects are a major concern.

1.3 Protection and shielding against radiation

Radiation shielding is a straightforward and feasible method to reduce radiation. Simply put, a shield has the function to maximize the absorption of incoming radiation as much as possible (More et al., 2021). Two ways of shielding from radiation can be achieved by means of active and passive shielding. Active shielding involves generating electromagnetic fields that deflect space radiation (Durante and Cucinotta, 2011). Examples of such shields are: electrostatic fields, plasma shields and magnetic fields (Adams et al., 2005; Spillantini et al., 2007; Townsend, 2001). Passive shielding is done by the use of materials that absorb space radiation through interactions between the radiation particles and the shield material. Polymers in particular, such as polyethylene, are attractive materials for shielding due to their high hydrogen content (Guetersloh et al., 2006; Simonsen and Nealy, 1991), and have long been proven to be more effective than aluminium. Aluminium is traditionally used for spacecraft structures, but compared to polyethylene, it is heavy, has only a limited efficiency against radiation, and can even induce secondary particles (Nambiar and Yeow, 2012; Wozniak et al., 2017). The reason why aluminium is often used is because of its good strength and strength-to-weight ratio. The shielding capability of aluminium and polyethylene in terms of dose reduction per unit thickness in g/cm^2 is shown in Figure 2, along with other reference materials. Designing space structures for radiation protection is not an easy task as there are many other aspects involved as well, e.g. micrometeorite protection, being able to handle space and planetary temperatures, and structural integrity of the material.

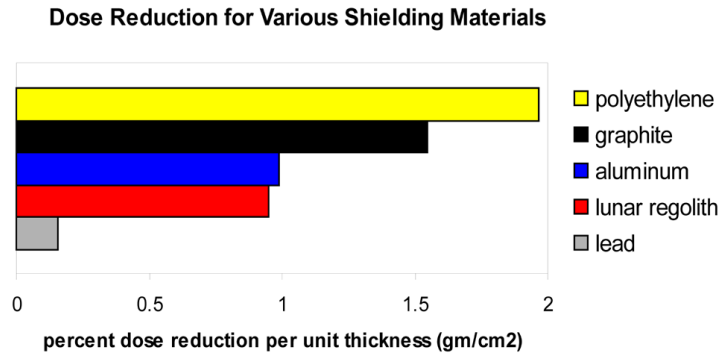


Figure 2: Dose reduction per unit thickness for various shielding materials (Heilbronn, Miller, and Zeitlin, 2019).

When designing for maximal radiation shielding, its associated risks and uncertainties should follow the fundamental principle of *As Low As Reasonably Achievable*, or ALARA in short. Fully shielding against space radiation is not realizable and therefore, maximum reduction should be pursued as much as possible (Battiston et al., 2012). It is not feasible to fully protect astronauts against all radiation, especially for long-term missions. ALARA translates into allowable radiation doses that can be received while staying below the 3% of REID.

The application of radiation shields proves to be a highly complex problem because the chosen material and thickness of the shield strongly influence the radiation absorption. For example, if a shield becomes thicker, the dose reduction decreases at some point, resulting in reduced shielding capabilities (Guetersloh et al., 2006). In other words, the largest radiation absorption takes place at the outermost layers of a shield and the dose reduction decreases exponentially deeper into the shield (Zeitlin, Guetersloh, Heilbronn, Miller, et al., 2008). The thickness of a shield should also be carefully determined. If the shield is too thin, it may not protect sufficiently against primary radiation but a shield that is too thick can lead to secondary radiation (Benaroya and Bernold, 2008). However, it is thought that a considerably thick shield should suffice to attenuate all or most secondary radiation.

It should also be noted that excessively thick shields are less feasible due to practical limitations. In the long term, passive shielding alone is not sufficient enough to provide abundant protection against space radiation. Ultimately, active shielding against radiation should be considered if the technologies exist and are feasible. Currently, however, they are still underdeveloped and unrealistic at a greater

scale, let alone to realize them on the Moon or Mars. Another way to reduce radiation absorption might be by taking medical and nutritional supplements that mitigate the effects of ionizing radiation (*Rask et al., 2008b*). In conclusion, a combination of all aforementioned methods should be opted to keep radiation doses ALARA and below the radiation limits. This is also recognized by *Battiston et al., 2012* and *Vuolo, Giraud, et al., 2016*.

2 Simulation preparations and data collection

2.1 Selection of radiation quantity

Many quantities exist to evaluate the effects of radiation. The three radiation quantities related to dose are absorbed dose, equivalent dose and effective dose. Absorbed dose, or dose in short, is a physical quantity and directly measurable, while equivalent dose and effective dose are protection quantities (*Ministry of the Environment, 2013*). Absorbed dose (D) is the accumulated energy in an absorbing material per unit mass by all radiation (*University of Florida, 2011*). The term Total Ionizing Dose (TID) is also largely used for this parameter. The commonly used unit to express absorbed dose is gray (Gy), while in SI base units this is J/kg, where $1 \text{ Gy} = 1 \text{ J/kg}$. The equivalent dose (H) is the absorbed dose multiplied by radiation weighting factors that take into account the harmful biological effects of all the types of radiation and their energies. Its commonly used unit is sievert (Sv), or in SI base units J/kg, where $1 \text{ Sv} = 100 \text{ J/kg}$. The dose equivalent is calculated by:

$$H = \sum w_R \cdot D \quad (1)$$

Where w_R is the weight factor due to the radiation particle type and D is the absorbed dose. The radiation weighting factors are shown in Figure 3. These weight factors are determined by the International Commission on Radiological Protection (ICRP) and are periodically updated.

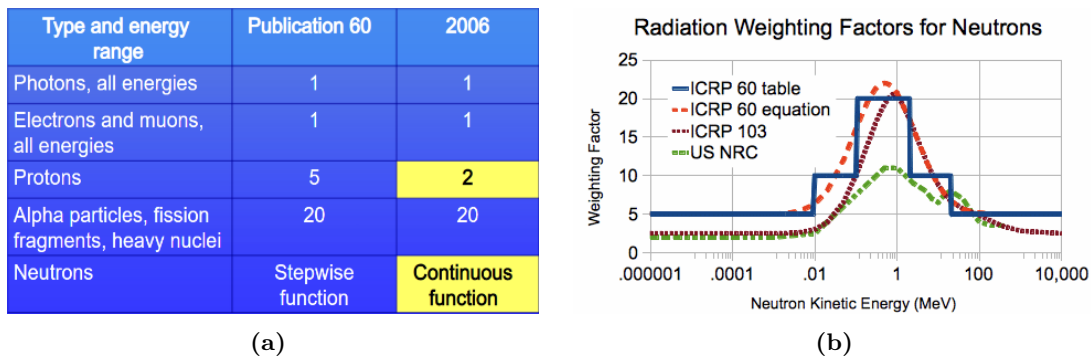


Figure 3: (a) The radiation weighting factors under ICRP publication 60 and the updated version of 2006 (*Burns, 2006*) and (b) various neutron functions according to the ICRP publication (*graph created by Y. Trottier under CC BY-SA 3.0*).

Effective Dose (E) is the equivalent dose multiplied by tissue weighting factors and is also expressed in sievert. These tissue weighting factors represent the individual radiation impact on human organs and tissues because they all react differently with radiation. It is important to note that the effective dose is only used for risk estimation in the context of radiation shielding, and not for calculating the dose of an individual (*University of Florida, 2011*). It is determined using the following equation in conjunction with Equation 1:

$$E = \sum w_T \cdot H = \sum w_T \cdot \left(\sum w_R \cdot D \right) \quad (2)$$

Where w_T is the weight factor for the organs and tissue. The radiation effects on the various human body parts are not yet fully understood and characterized, meaning that these weight factors are also subject to change. The three discussed radiation dose quantities are summarized in Figure 4. It should

be noted that subscripts T and R are sometimes used, such as in this figure, to denote the human body part and the radiation particle, respectively.

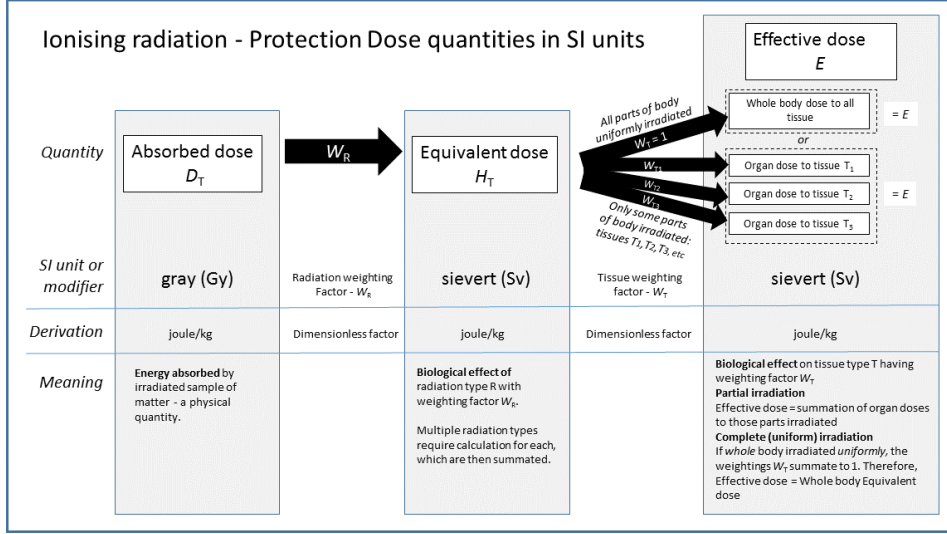


Figure 4: Correlations between absorbed, equivalent and effective dose (overview created by D. Sim under CC BY-SA 3.0).

Dose reduction is, simply put, the measured dose in a situation with and without a shield in front of a specimen. Essentially, it represents how much of the specific radiation is attenuated by the shield. In this paper, the (absorbed) dose is assessed. The reason for this is that this dose is directly measurable, while the equivalent dose and effective dose require the aforementioned weighting factors that are subject to change. Consequently, results that would use these quantities may not be representative anymore in the future, while the absorbed dose would still be.

The dose reductions can be calculated from the FLUKA simulation results. FLUKA (Fluvtuierende Kaskade) is a radiation transport code software that models the interactions between particles and materials. From the five FLUKA cycles per simulation, five values are attained that represent the absorbed dose of the detector behind the shield. The average of these five values is then calculated using:

$$\bar{D}_{runs} = D_1 + D_2 + D_3 + D_4 + D_5 \quad (3)$$

These values are originally expressed in [GeV/g/cm³/primary] by FLUKA and should be converted to [Gy/primary]. This is done by multiplying the values by $1.602176462 \times 10^{-7}$ and consequently dividing by the volume of the detector, as stated by *Ferrari et al., 2021*. The converted average value from Equation 3 becomes:

$$\bar{D}_{runs} = \bar{D}_{runs} \cdot \frac{1.602176462 \times 10^{-7}}{800,000} \quad (4)$$

In this work, the detector has a length and width of 200 cm and a thickness of 20 cm, resulting in a detector volume of 8×10^5 cm³. Once converted, simulations are ran for the case where there is no shield between the radiation beam and detector and for the case with a shield of a certain thickness between the radiation beam and detector, depicted in Figure 5. Finally, the dose reduction is calculated using:

$$\delta D = \frac{\bar{D}_{runs_no_shield} - \bar{D}_{runs_shield}}{\bar{D}_{runs_no_shield}} \quad (5)$$

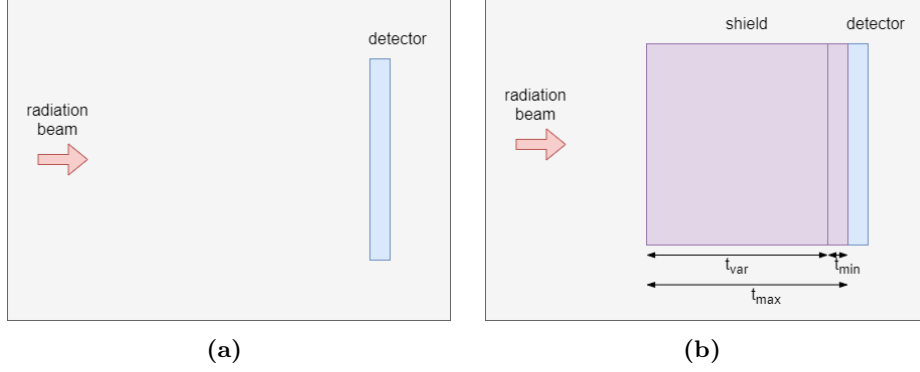


Figure 5: 2D projection of the initial simulation setup for the cases (a) without shield and (b) varying shield thickness.

Each resulting value from the five FLUKA cycles consisting of 10,000 primary particles also has a certain standard error of the mean (SEM) which is calculated by:

$$E_{runs} = \frac{\sigma}{\sqrt{N}} \quad \text{with} \quad \sigma = \sqrt{\frac{\sum_{i=5}^N (D_i - \mu)^2}{N}} \quad (6)$$

Where D_i is the absorbed dose of each cycle, μ the mean of all absorbed dose values from the cycles and N the number of cycles, which is five. The dose reduction from Equation 5 can also be converted to:

$$\delta D = 1 - \frac{\overline{D}_{runs_shield}}{\overline{D}_{runs_no_shield}} \quad (7)$$

Equation 7 now consists of a constant value minus a division. Adding or subtracting a constant value does not change the SEM. Because of this division, the error of the dose reduction can be calculated by:

$$E_{\delta D} = \frac{\overline{D}_{runs_shield}}{\overline{D}_{no_shield}} \cdot \sqrt{\left(\frac{E_{runs_shield}}{\overline{D}_{runs_shield}}\right)^2 + \left(\frac{E_{runs_no_shield}}{\overline{D}_{runs_no_shield}}\right)^2} \quad (8)$$

2.2 GCR and SPE in the Martian radiation environment

Comparing GCR with SPE can be based on four terms: dose rate, duration, dose contribution and energy levels (*Rapp, 2006; Wilkinson et al., 2016; Zeitlin and La Tessa, 2016*). For GCR, the dose rate is lower compared to the very high short-term SPE dose rate, but the GCR dose rate is steady due to the constant bombardment of high-energy particles. This leads to a continuous and steady GCR flux, while for SPE this is only hours to days. The dose contribution of GCR becomes more significant by longer mission durations and becomes an increasing risk of exceeding the career or annual limits. SPE dose contributions are rather low for long mission durations, but its intense radiations bursts can lead to exceeding short-term exposure limits. GCR energies are high and its biological effects are not fully understood until now, while SPE energies are lower than for GCR and thus easier to shield against. On Mars, according to OLTARIS (which is addressed in the next paragraph), the high GCR energies are in the range of tens of GeV, while for SPE the maximum energies are in the range of a few GeV. This is discussed more in detail in Section 2.3.

To ensure that GCR is indeed more significant than SPE for this work, the OLTARIS¹ tool is used to compare them and finally one of these sources is selected to proceed with. OLTARIS, short for On-Line Tool for the Assessment of Radiation In Space, was developed by NASA and is used to acquire radiation data. In particular, the differential flux of radiation during GCR and SPE events on the Martian surface is retrieved. The GCR during solar minima, which is the worst case condition as

¹accessed via <https://oltaris.nasa.gov/>

discussed earlier, is shown in Table 2. With regard to SPE events, OLTARIS offers 11 events which are also presented in Table 2. The subscripts *a-g* indicate the type of fit used to model the event. LaRC stands for NASA’s Langley Research Center, while Webber, King and Tylka refer to the name of the author that developed or documented these fits (*Jiggins et al., 2014*).

Table 2: Dates of GCR during solar minima and historical SPE from OLTARIS.

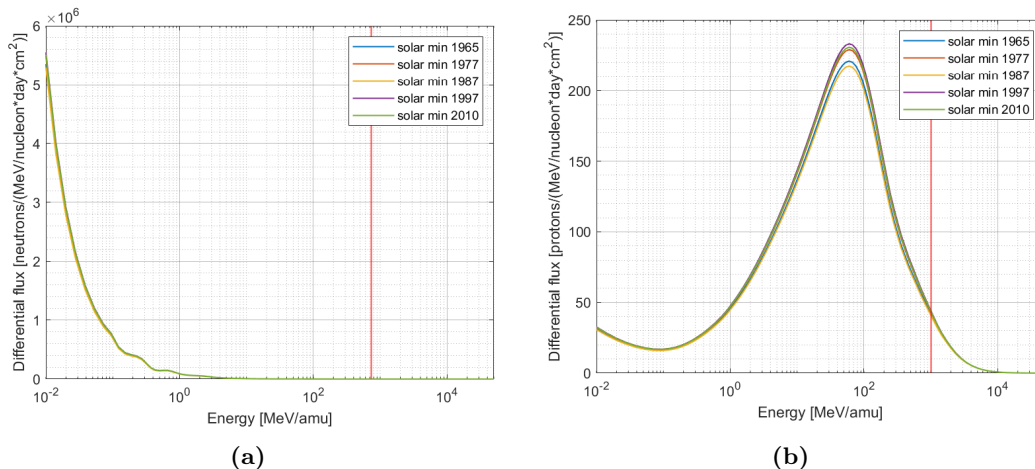
GCR events	SPE events	
1965	Sep 1859 ^{a, b}	Sep 1989
1977	Feb 1956 ^{c, d}	Oct 1989
1987	Nov 1960	Oct 1989 ^g
1997	Aug 1972 ^{e, f}	
2010	Aug 1989	

a: Carrington - Sep 1989 hard fit, **b:** Carrington - Mar 1991 soft fit, **c:** Webber, **d:** LaRC, **e:** LaRC, **f:** King, **g:** sum of October 1989 Tylka Band fits

Various models can be selected for the GCR environment, and the most recent one is chosen, being the Badhwar-O’Neill 2020 mode (*Slaba and Whitman, 2020*). Furthermore, an elevation on the Mars surface between -10 km and 30 km should be defined. In general, the higher the elevation, the more radiation is experienced. An elevation of 0 km is chosen because the output from this work could serve as a reference and basis for further research, possibly taking specific locations and elevations into account. For SPE environments, all historical events are selected with the same chosen elevation of 0 km.

2.3 Selection of particle energy types and energies

Before running the simulations, particles and their respective energies should be selected. Including all particle types with their individual energy spectra would require massive computational power and time that is not available nor feasible. First, the selection of GCR or SPE fluxes is made. From the OLTARIS output for all five available GCR events, the differential fluxes for neutrons, protons, helium and combined HZE ions are plotted in Figure 6.



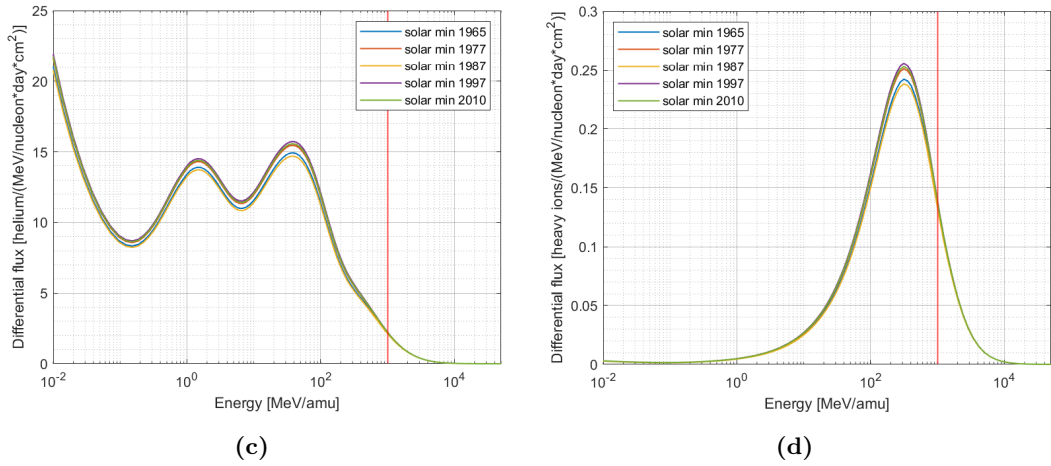


Figure 6: Differential flux versus energy for GCR during five solar minima of (a) neutrons, (b) protons, (c) helium and (d) HZE ions. The unit *amu* is the atomic mass unit, and is a constant value.

Vertical lines drawn in this figure indicate 740 MeV for neutrons and 1 GeV for the other particle types, which is discussed hereafter when the energies are selected. Similarly, the 11 SPEs are plotted in Figure 7.

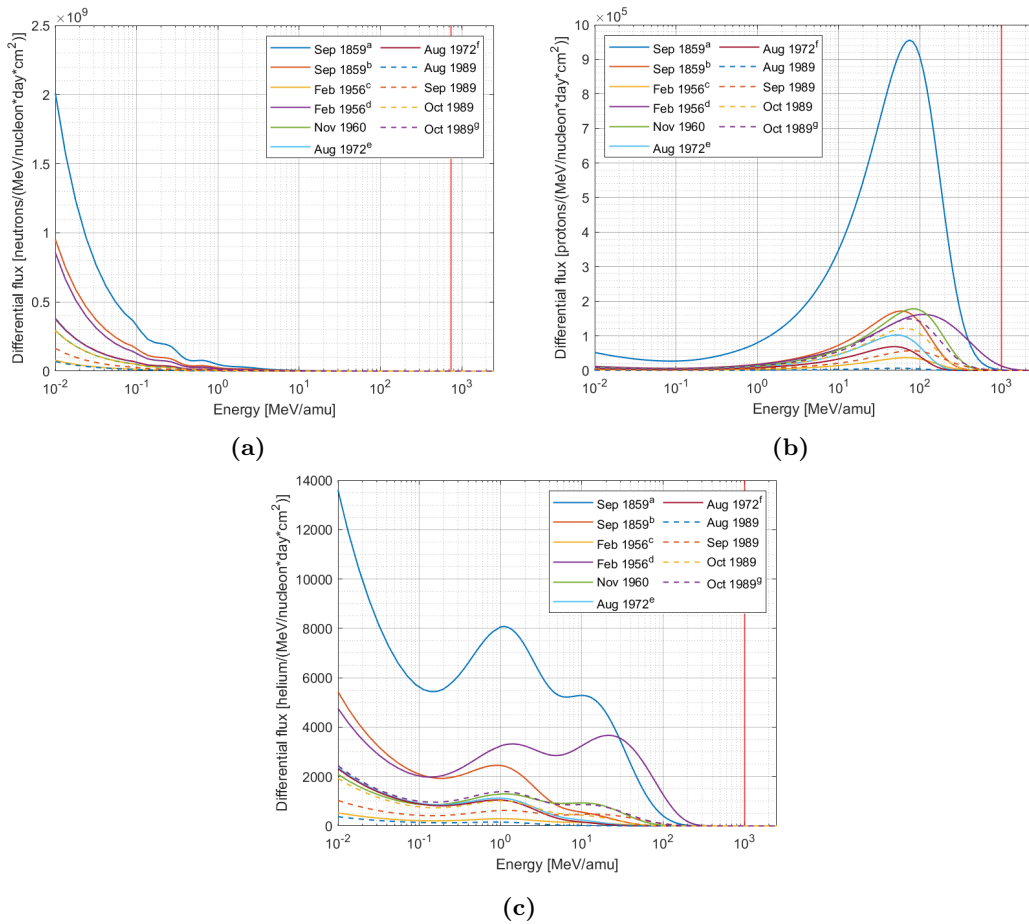


Figure 7: Differential flux versus energy for all 11 historical SPEs of (a) neutrons, (b) protons and (c) helium. The unit *amu* is the atomic mass unit, and is a constant value.

It can be seen from Figures 6 and 7 that the energy spectrum for GCR has an upper limit of 50 GeV, while for SPE it is 2.5 GeV. This is a big difference and for this reason, GCR is chosen as the source to continue with. Furthermore, the particle spectrum of GCR and SPE both include neutrons, protons and helium. Based on this, when optimizing radiation reduction for GCR radiation, SPE radiation is also optimally shielded.

Choosing particles is based on their contribution to the flux of the entire particle spectrum. Figure 8 shows the relative particle contribution in fluence (i.e. flux) of GCR for atomic numbers from Z=1 to 26 during a solar minimum. This figure shows that protons (H) and helium (He) have the largest contributions. Then, from Z=3 to 8, carbon and oxygen are most present, while for Z=9 to 14 these are neon, magnesium and silicon. Iron (Fe) is far more abundant for Z=15 to 28.

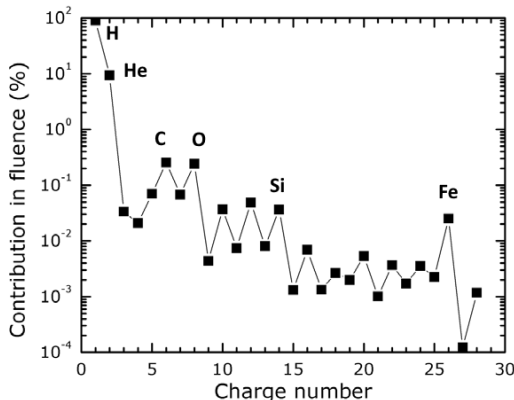


Figure 8: Contribution in GCR fluence by particle types during a solar minimum (adapted from *Geng et al., 2015*).

Since it is known that neutrons are created on the Martian surface through interactions with the surface and atmosphere, its contribution must also be determined, which can be done using the integral flux of the particle spectrum. Neutrons in particular are a major threat to human health and the interactions between neutrons and nuclei of biological tissue occur easily (*Wimmer-Schweingruber et al., 2020*). Usually, neutrons have low energies but possess a high ionization that destroy cells by damaging DNA and by producing free radicals. The integral fluxes can be determined from the OLTARIS differential flux data. The OLTARIS output for the differential flux on the Martian surface includes 100 energy values and 59 particle types, which are neutrons and particles from Z=1 to 28, with some of the particles having several different atomic weights. It is important to mention that secondary neutron radiation must be taken into account as well. The OLTARIS output only gives a differential flux at a specific energy value, while energy bins are needed for calculating the integral flux. These energy bins, or intervals, are determined by two consecutive energy values from the OLTARIS output file. The differential flux in these intervals is calculated by means of interpolation and expressed in [*particles/(MeV/nucleon·day·cm²)*]:

$$DF_i = DF_{lower} + (E_i - E_{lower}) \cdot \frac{DF_{upper} - DF_{lower}}{E_{upper} - E_{lower}} \quad \text{with} \quad E_i = \frac{E_{lower} + E_{upper}}{2} \quad (9)$$

Where DF_i and E_i are the differential flux and energy at each interval respectively. The integral fluxes are then calculated with the differential flux values from Equation 9 and are expressed in [*particles/(day·cm²)*]:

$$IF_1 = \int_{E_{lower}}^{E_{upper}} DF_1 \cdot dx = DF_1 \cdot [x]_{E_{lower}}^{E_{upper}} = DF_a \cdot (E_{upper} - E_{lower}) \quad (10)$$

After the integral flux has been calculated for each interval, all values per particle type are summed. The contribution is then determined by dividing the total integral flux per particle type by the total integral flux of all considered particle types. This was applied to the OLTARIS output file and the

resulting GCR contributions are determined and shown in Table 3, for all five available solar minimum events, as well as visualized in Figure 9 for the 2010 solar minimum as an example.

Table 3: Total integral flux value and particle type contributions for neutrons, protons, helium and HZE ions during five solar minima, as well as the average values from these solar minima.

Solar min	1965	1977	1987	1997	2010	Average
Total IF	9.37E+05	9.63E+05	9.25E+05	9.76+05	9.68E+05	<i>9.54E+05</i>
Contribution						
Neutron	82.1967%	82.0533%	82.2604%	81.9818%	82.0236%	<i>82.10%</i>
Proton	16.8848%	17.0260%	16.8221%	17.0965%	17.0554%	<i>16.98%</i>
Helium	0.8770%	0.8793%	0.8759%	0.8804%	0.8798%	<i>0.88%</i>
HZE*	0.0415%	0.0413%	0.0416%	0.0413%	0.0413%	<i>0.04%</i>
<i>*heavy ions included by OLTARIS are from lithium to nickel</i>						

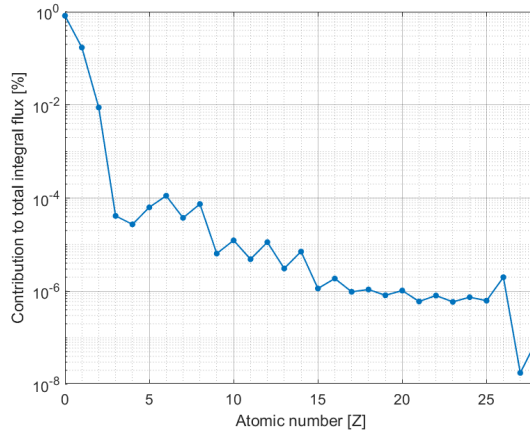


Figure 9: Contributions of neutrons and elements from Z=1 to 28 on the Martian surface from GCR during the 2010 solar minimum.

Table 3 shows that the total integral flux values and the particle contributions for all five solar minima are almost equal. This gives an indication that GCR radiation is indeed constant and steady, as mentioned previously. From this table, it can also be concluded that neutrons are predominant on the Martian surface with a contribution of $\sim 82\%$, followed by protons $\sim 17\%$, helium $\sim 0.88\%$ and only a tiny fraction of $\sim 0.04\%$ by HZE ions. However, HZE ions should not be neglected due to their much higher radiation weighting factors as shown in Figure 3a. This means that in the case of the equivalent dose, their contribution increases considerably. This is also demonstrated in Figure 10, where the equivalent dose largely corresponds to the regions where there is a higher risk of heavy ion bombardments.

Figure 9 shows that on the Martian surface with the inclusion of neutrons, the relative abundances between HZE ions are still very similar to those in free space as seen in Figure 3. When selecting heavy ions, it should be noted that FLUKA simulations for heavy ions require extensive computational power, which increases significantly for higher atomic numbers. For this reason, a compromise had to be made. Based on Table 3, Figure 9 and these considerations, the following particles were chosen: neutrons, protons (H), helium (He), carbon (C), oxygen (O), silicon (Si) and iron (Fe). This selection should provide a reasonable representation of GCR on the Martian surface for this intended work.

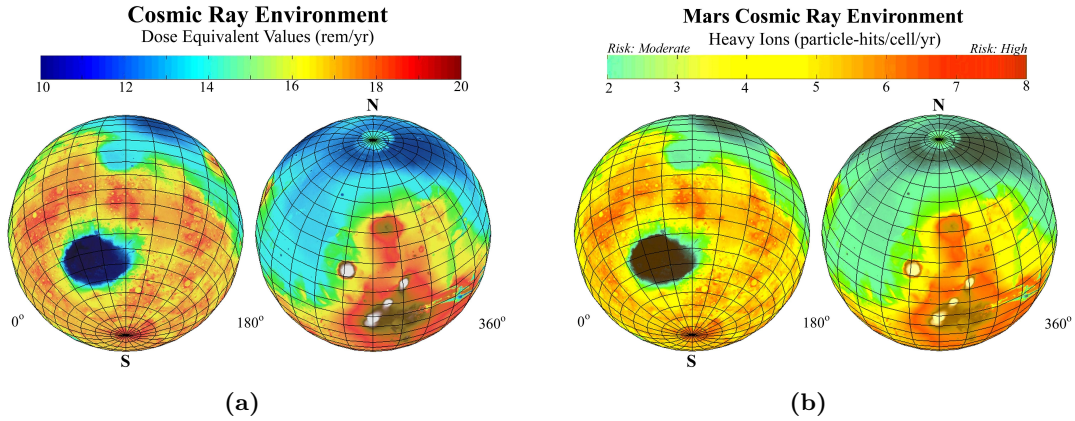


Figure 10: The cosmic ray environment of Mars in terms of (a) dose equivalent values and (b) risks of heavy ion bombardment (*NASA, JPL, and Johnson Space Center, n.d.*).

Although radiation from SPE is no longer considered, the particle contributions to the total integral flux are determined and documented for future work. These are shown in Table 4 and Figure 11.

Table 4: The contribution of neutrons, protons and helium to the total integral flux for all 11 SPEs.

SPE	Total IF	Contribution		
		Neutron	Proton	Helium
Sep 1859 ^a	6.1108E+08	67.26%	32.70%	0.04%
Sep 1859 ^b	2.2188E+08	88.82%	11.17%	0.01%
Feb 1956 ^c	2.2678E+07	72.68%	27.30%	0.02%
Feb 1956 ^d	2.2522E+08	64.95%	34.90%	0.15%
Nov 1960	9.6986E+07	61.98%	37.98%	0.04%
Aug 1972 ^e	9.2400E+07	87.52%	12.47%	0.01%
Aug 1972 ^f	8.8478E+07	91.87%	8.12%	0.01%
Aug 1989	1.4876E+07	94.86%	5.14%	0.01%
Sep 1989	4.6668E+07	67.98%	31.95%	0.07%
Oct 1989	8.1072E+07	76.09%	23.89%	0.02%
Oct 1989 ^g	1.0893E+08	70.71%	29.25%	0.04%

a: Carrington - Sep 1989 hard fit, b: Carrington - Mar 1991 soft fit, c: Webber, d: LaRC, e: LaRC, f: King, g: sum of October 1989 Tylka Band fits

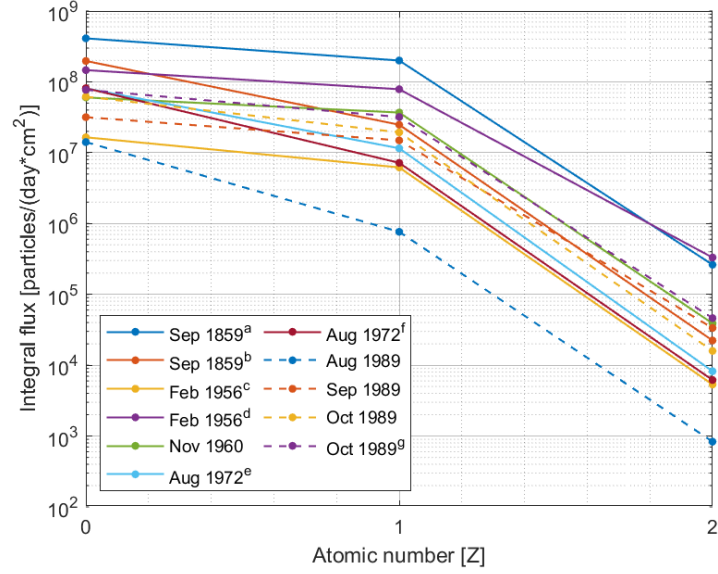


Figure 11: The integral fluxes of neutrons, protons and helium for all 11 SPEs. Historical data and labels are in accordance with Table 4.

Now that the particle types have been chosen, their energies are also determined. In the case of neutrons, the energy is chosen to be 740 MeV. This is because a neutron energy range of 8-740 MeV is measured on the Martian surface by the Radiation Assessment Detector (RAD) of the Mars Science Laboratory (MSL) aboard the Curiosity Mars rover, as reported by *Litvak et al., 2020*. Comparing this to Figures 6a and 7a, where the red vertical line represent 740 MeV, it can be seen that the majority of the neutrons are in the low energy range. Designing for 740 MeV neutrons is therefore intended for the worst case scenario. For the other remaining particles, namely protons, helium, carbon, oxygen, silicon and iron, the chosen energy is 1 GeV, and it can be seen from Figure 6 that the majority of these particles are left of this line. Choosing an energy of 1 GeV is also a compromise between a higher energy limit and the required computation effort, as well as the time to run all simulations. Choosing energies even higher than 1 GeV is not feasible due to time constraints. Furthermore, it can also be seen that the particle flux for higher energies decreases dramatically. Figure 12 shows the combination of the chosen particle types for GCR and SPE, as well as the 740 MeV and 1 GeV energies. This figure confirms again that the most particles have energies below these lines.

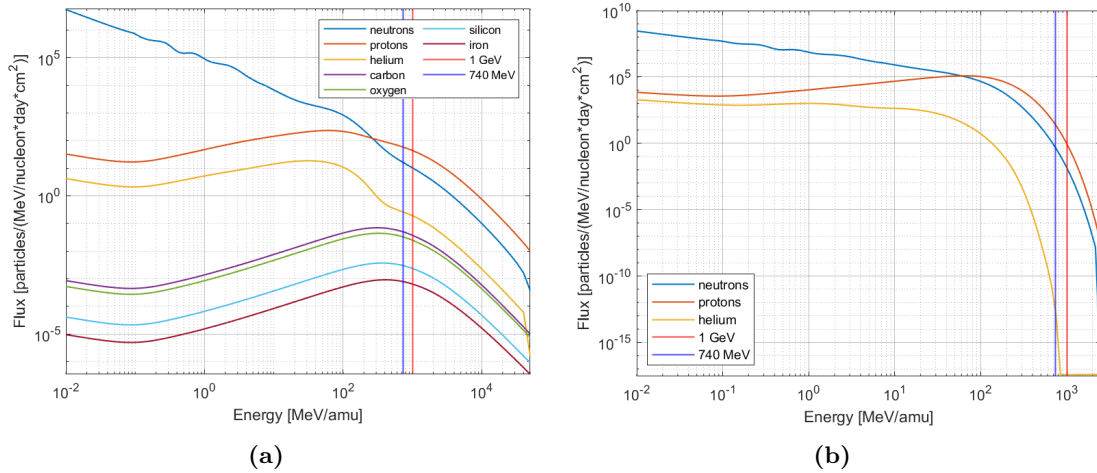


Figure 12: Differential flux versus energy for (a) GCR radiation during the solar minimum of 2010 and (b) SPE radiation during October 1989. The unit *amu* is the atomic mass unit, and is a constant value.

2.4 Martian regolith simulant MGS-1

Considering that the particle types and energies have been selected, the Martian regolith simulant MGS-1 is characterized consequently. This simulant, shown in Figure 13a, is used as the equivalent of Martian regolith. MGS-1 stands for Mars Global Simulant, was developed by the University of Central Florida, and can be purchased from Exolith Lab in the USA. It is a simulant standard for the high-fidelity mineralogical standard for the global basaltic Martian regolith, which is characterized by the Rocknest windblown deposit at Gale crater on Mars, shown in Figure 13b. Rocknest regolith was chosen as the reference because it best characterizes Martian soil at the time of writing of *Cannon et al., 2019*. Its physical properties and bulk chemistry are presented in Tables 5 and 6, respectively. The MGS-1 fact sheet can be retrieved from Appendix A.

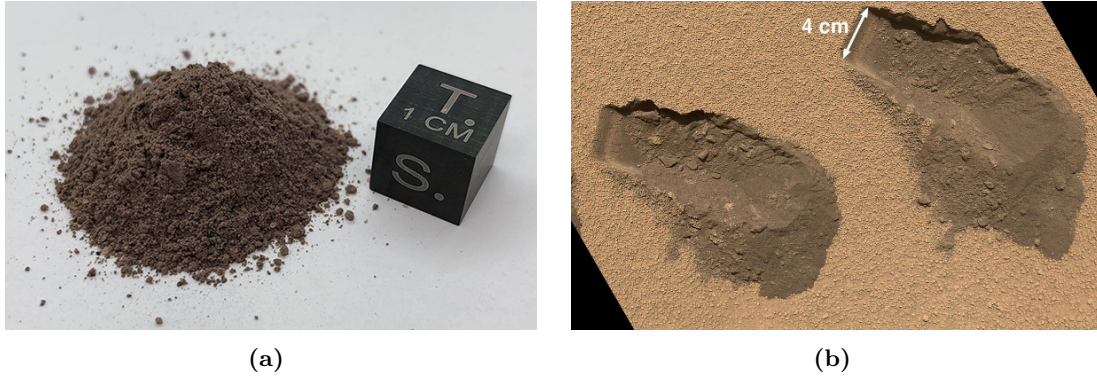


Figure 13: (a) Martian regolith simulant MGS-1 (*Central Florida, n.d.*) and (b) Martian regolith at the Rocknest deposit photographed by the Curiosity rover (*NASA, JPL-Caltech, and MSSS, 2012*).

Table 5: Physical properties of MGS-1 (*Cannon et al., 2019*).

Property	Value
Particle size	0-1 mm
Mean particle size (by volume)	122 μm
Bulk density	1.29 g/cm^3

Table 6: Bulk chemistry of oxides in MGS-1 (*Cannon et al., 2019, Achilles et al., 2017*).

Oxide wt% (total of 99.99%)											
SiO ₂	TiO ₂	Al ₂ O ₃	Cr ₂ O ₃	FeO	MnO	MgO	CaO	Na ₂ O	K ₂ O	P ₂ O ₅	SO ₃
45.57	0.30	9.43	0.12	16.85	0.10	16.50	4.03	3.66	0.43	0.37	2.63

The MGS-1 simulant is a recent standard Martian simulant that better approximates the global basaltic Martian regolith compared to MMS-1, MMS-2 and JSC Mars-1 simulants, as reported by *Cannon et al., 2019*, and shown by the reflectance spectrum in Figure 14. This figure shows that the MGS-1 spectrum resembles the analyzed Rocknest soils much more than the other simulants. For this reason, as well as its availability, MGS-1 is chosen as the shield material for the FLUKA simulations. Other variations of MGS-1 are MGS-1S and MGS-1C, which are modifications enriched with polyhydrated sulfate gypsum and hydrated clay minerals, respectively.

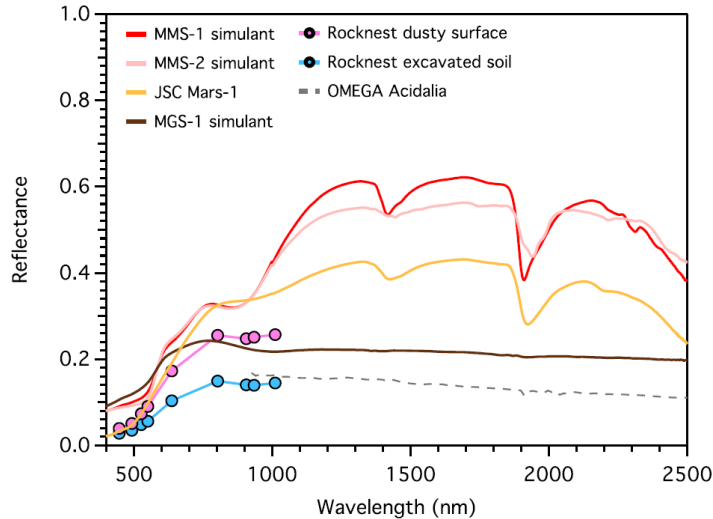


Figure 14: Reflectance spectrum of MGS-1 and other Martian simulants compared to the Rocknest regolith (*Cannon et al., 2019*).

Finally, *Karl et al., 2020* created a slurry composed of MGS-1 and MGS-1C regolith simulants, which are deposited layer by layer, much like 3D printing. Once deposited, it is sintered in a simulated Martian atmosphere. A bulk density of 2.49 g/cm^3 of the material created in this simulated atmosphere was reported. Using it as a reference value, this density will be used hereafter as an upper limit for the MGS-1 density in the simulations, while the MGS-1 bulk density of 1.29 g/cm^3 (shown in Table 5) will be used as the lower density limit.

2.5 Shield thickness

The shield thickness of the MGS-1 shield for the dose reduction assessment is based on several references. *Röstel et al., 2020* describes that shield thicknesses should be between 80 cm and 250 cm, depending on the soil composition, in order to keep the annual equivalent dose below 100 mSv. The more hydrated the soil is, the thinner the shield can be. Furthermore, they mention that a minimum area density value of $\sim 200 \text{ g/cm}^2$ should be chosen when using dry and rocky Martian subsurface materials. Taking into account the previous upper and lower density limits of 2.49 g/cm^3 and 1.29 g/cm^3 , results in a minimum shield thickness of $\sim 80 \text{ cm}$ and $\sim 155 \text{ cm}$, respectively.

Documentation about thicknesses of Martian regolith shields are limited and for this reason, published analyses about lunar regolith are also used to support the Martian regolith thickness selection. *Meurisse et al., 2020* mentions that regolith shielding of more than 200 g/cm^2 is required to absorb more than 50% of GCR radiation, while SPE radiation is already absorbed by more than an order of magnitude at several 10 g/cm^2 . *Ceccanti et al., 2010* reports that a regolith shield thickness of 1 m to 2 m is needed to keep the total dose within a reasonable level for mission times between six months and one year. *Benaroya and Bernold, 2008* notes that a minimum of 250 cm regolith shielding is needed to stay below the annual dose of 0.05 Sv. Finally, *Zhou et al., 2020* states that 200 cm of lunar regolith shielding protects the inner area from the destructive lunar radiation environment.

This leads to a chosen shield thickness of 250 cm, mainly based on *Röstel et al., 2020*. However, for the initial simulations, all dose reductions will mostly be assessed for shield thicknesses up to 400 cm. This is to understand the progression of the dose reductions at different shield thicknesses as well as having reference values for future work.

2.6 Verification of FLUKA software

To ensure that the FLUKA and flair installations were successful, several of the publicly available FLUKA exercises were carried out with equal results. Also recreating plots from the [Brookhaven National Laboratory](#) (BNL) and from *Durante and Cucinotta, 2011*, showed similar results.

3 Sensitivity analysis on dose reduction simulations

3.1 Dose reduction of polymers and reference materials

Prior to running the initial simulations, a selection of thermoplastic polymers is made based on the options given in [GRANTA EduPack 2020](#) and existing 3D printing filaments. This selection, in addition to reference materials, is shown in Table 7 with associated molecular formulae and densities. This list was created to assess their radiation shielding capabilities with respect to each other and some reference materials that are usually mentioned in terms of space radiation shielding.

Table 7: The density and molecular formula of the selected polymers and reference materials.

Material	Molecular formula	Density [g/cm ³]	Material	Molecular formula	Density [g/cm ³]
LH₂	H ₂	0.0708	PEEK	C ₁₉ H ₁₂ O ₃	1.264
H₂O	H ₂ O	1	PEI	C ₃₇ H ₂₄ O ₆ N ₂	1.27
Al	Al	2.699	PEKK	C ₂₀ H ₁₂ O ₃	1.279
Pb	Pb	11.35	PET	C ₁₀ H ₈ O ₄	1.333
MGS-1	/	1.29	PI	C ₂₂ H ₁₀ O ₅ N ₂	1.42
ABS	C ₁₅ H ₁₇ N	1.04	PLA	C ₃ H ₄ O ₂	1.248
ASA	C ₁₈ H ₂₃ O ₂ N	1.07	PMMA	C ₅ H ₈ O ₂	1.159
COC	C ₉ H ₁₄	1.02	POM	CH ₂ O	1.425
LCP	C ₁₈ H ₁₀ O ₄	1.4	PP	C ₃ H ₆	0.9
PC	C ₁₆ H ₁₄ O ₃	1.2	PS	C ₈ H ₈	1.06
PE	C ₂ H ₄	0.94	PVC	C ₂ H ₃ Cl	1.388

One way to assess the radiation shielding effectiveness of materials is by using the Material Index (MI), which represents the ratio of electronic stopping power to the nuclear interaction transmission (*Durante and Cucinotta, 2011; Naito et al., 2020; Vuolo, Baiocco, et al., 2017*). The MI is calculated using:

$$MI = (Z/\rho) \cdot A^{-2/3} \quad (11)$$

Where Z is the atomic number, ρ the density in kg/m³, and A the atomic weight of the material. When dealing with compound materials, the effective atomic number is determined by:

$$Z_{eff} = A_{eff} \cdot \sum \left(\frac{w_i \cdot Z_i}{A_i} \right) \quad \text{with} \quad A_{eff} = \sum (w_i \cdot Z_i) \quad (12)$$

Where w_i is the relative weight factor of each atom expressed in percentage. The relative weight factor w_i is calculated using:

$$w_i = \frac{N_i \cdot A_i}{\sum (N_j \cdot A_j)} \quad (13)$$

Where N_i is the total number of element i in the material, A_i is the atomic weight of element i , and subscript j depicts all elements present in the material. Other ways to assess the effectiveness of radiation shielding are done by comparing the effective atomic mass A_{eff} shown in Equation 12. According to *Durante and Cucinotta, 2011*, materials with the smallest effective atomic mass protect most effectively against GCR and SPE radiation. Calculating the MI of all materials from Table 7 results in the graph shown in Figure 15a. In this figure, the lower and upper ranges of the MI are

shown in dark and light blue, respectively. The orange markers represent the MI with the densities from Table 7. This range of MI is a direct result from the density range of some polymers. Hence, it is important to consider the actual densities when assessing the radiation shielding of polymers. MI values of several materials are reported in *Vuolo, Baiocco, et al., 2017*; 14, ~ 1 , 0.5, 0.2, ~ 1 , ~ 0.82 and ~ 0.66 for LH₂, H₂O, Al, Pb, PE, PMMA and POM, respectively. These are similar values when compared to the displayed values of Figure 15b.

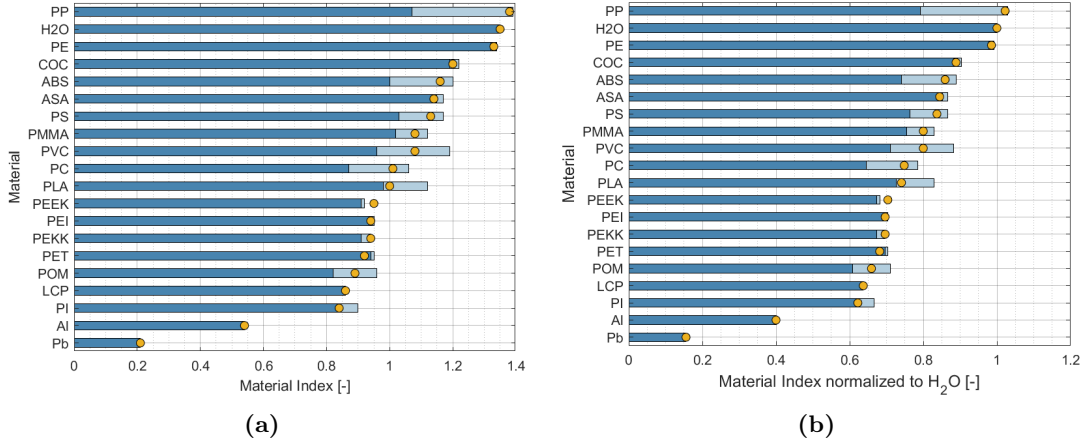
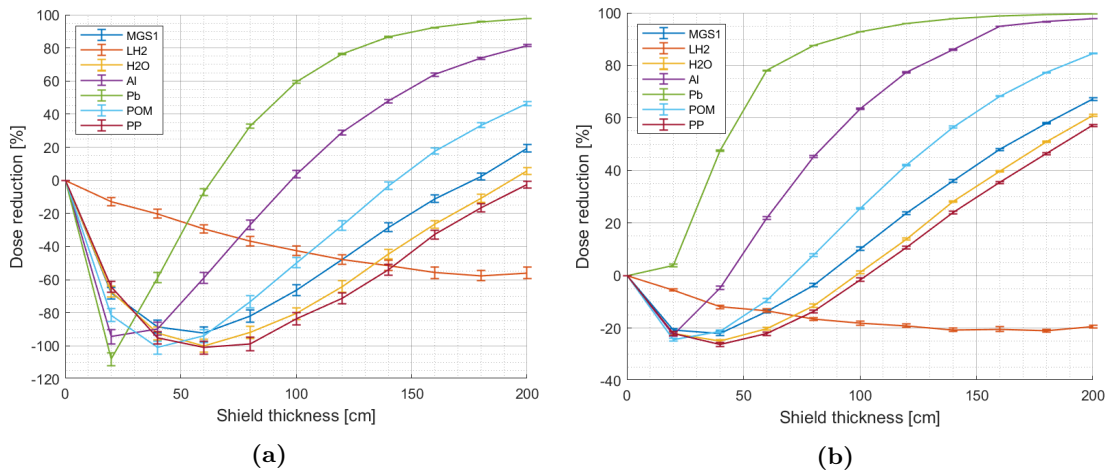
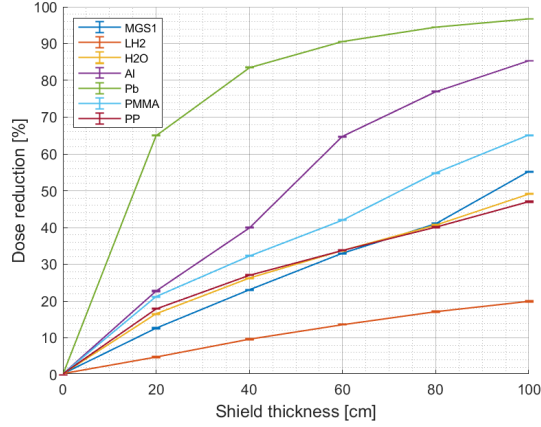


Figure 15: (a) Material Index of assessed materials from Table 7 and (b) normalized to the MI of H₂O. Liquid hydrogen is excluded because of its high MI value of ~ 14 .

The materials from Table 7 have also been simulated in FLUKA for shield thicknesses from 20 cm to 200 cm for neutrons and protons, and up to 100 cm for helium and carbon beams. All the dose reduction values for all considered materials, particle types, and shield thicknesses are shown in Appendix C. As seen in Figure 16, the results show that both MGS-1 and H₂O are within the range of all polymers, while aluminium and lead perform best for all assessed particle types for larger thicknesses. For neutrons and protons, it can be seen that for materials with a better dose reduction for larger thicknesses, the first tens of cm actually lead to a worse dose reduction (i.e. a larger dose increase). This is something to consider when designing the outer layers of a radiation shield or for thin shields in general. For neutrons, protons and helium, liquid hydrogen initially provides better shielding, but is then outperformed by all other materials for larger thicknesses. The dose reductions for neutrons, protons and carbon for the reference materials, MGS-1 as well as the best and worst performing polymer at 200 cm (for neutrons and protons) and 100 cm (for carbon) are shown in Figure 16. All other plots for these materials and assessed particle types can be seen in Appendix D. When using helium beams, all assessed materials reached a dose reduction of $\sim 90\%$ at ~ 40 cm, except for lead, aluminium and liquid hydrogen.

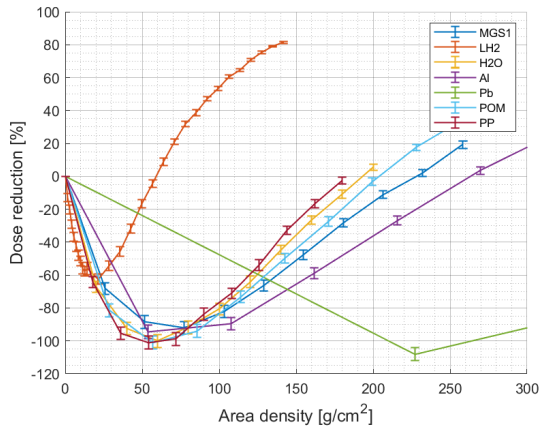




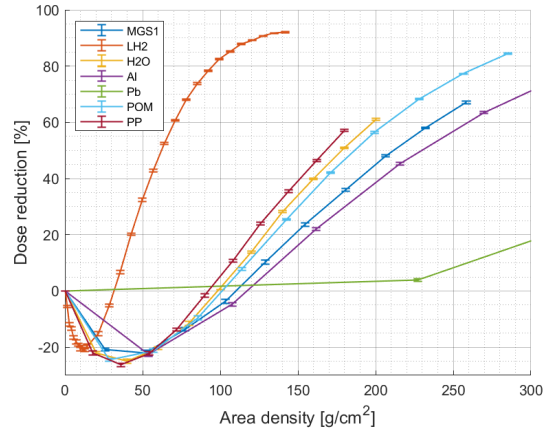
(c)

Figure 16: Dose reduction from 1 GeV monochromatic (a) neutron, (b) proton and (c) carbon beams for selected polymer and reference material shields with a thickness range of 0-200 cm and 0-100 cm.

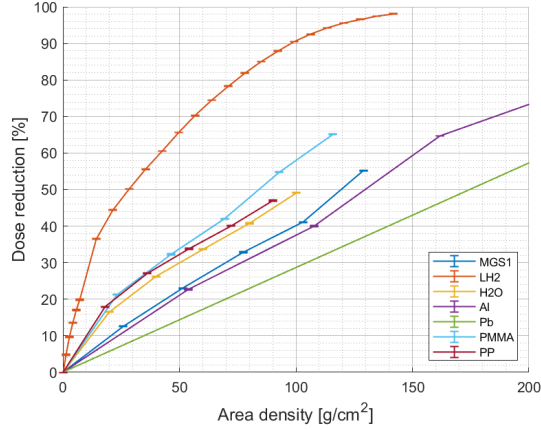
Figure 16 and Appendix D show that materials with a higher MI from Figure 15a are among the worst performing materials. This has to do with the densities and Table 7 indicates that the materials with low densities such as LH₂, PE and PP are performing worse than all other materials. From this can be concluded that the effect of density has a significant impact on dose reduction. Materials that are more dense lead to a higher probability of interactions between radiation particles with the shield material (*Hellström, Diószegi, and Diaconu, 2017*), meaning that more energy is absorbed by the material. A better way and usually the conventional method to compare radiation shielding materials is by assessing the absorbed dose versus the area density. The area density is the shield thickness multiplied by the material density and is expressed in g/cm². Following this method, the density effect of materials is omitted in the comparisons. Comparing the same materials from Figure 16 but in terms of the area density is shown in Figure 17. The complete selection of area density plots is shown in Appendix E.



(a)



(b)



(c)

Figure 17: Dose reduction from a 1 GeV monochromatic (a) neutron, (b) proton and (c) carbon beam for selected polymer and reference material shields in terms of area density.

Figure 17 shows that when comparing the materials by area density, liquid hydrogen performs best, except for the first ten g/cm^2 or so. It can also be seen that MGS-1 also underperforms with respect to the other polymers and H_2O , but not by a great extent. Conversely, MGS-1 outperforms aluminium and lead. Comparing the dose reduction of these materials is now much more in line with the MI ranking from Figure 15a. However, it should be noted that the area density is meant for comparison purposes only and the actual shield thickness is a better representation of a real-life scenario. Therefore, the dose reduction comparisons using the shield thicknesses are leading. In this regard, MGS-1 has shown to be a very promising material for radiation shielding due to its positive performance in terms of dose reduction. Moreover, as a human presence on Mars is eventually envisioned, regolith is a quasi infinite source of materials. When combining MGS-1 and polymers, it is necessary to investigate the impact of adding a polymer that, by itself, already has an improved radiation shielding effectiveness. The reason for this investigation is that the dose reduction becomes less effective deeper in the shield (*Guetersloh et al., 2006*), as discussed previously. However, placing polymers as outermost shield layer in the hazardous Martian environment will also result in much faster degradation of these precious materials, which must be taken from Earth or created on Mars in the long term. Furthermore, the cryogenic temperatures to which the polymer is exposed to, when placed as an outermost layer, could also lead to a vast decrease in its performance, become brittle and less effective in terms of radiation absorption. It is also exposed to micrometeoroids and dust storms. These implications are not addressed in this work as it is not the main focus, but must eventually be taken into account. For these reasons, it seems more reasonable to place the polymer at more inner layers in the shield. Therefore, two scenarios are envisioned to analyse the influence on dose reduction by adding a layer of pure polymer, as well as a composite of MGS-1 and a polymer. The first scenario includes a layer in the middle of the regolith shield, the second scenario includes a layer on the inside of the shield. Both are shown in Figure 18.

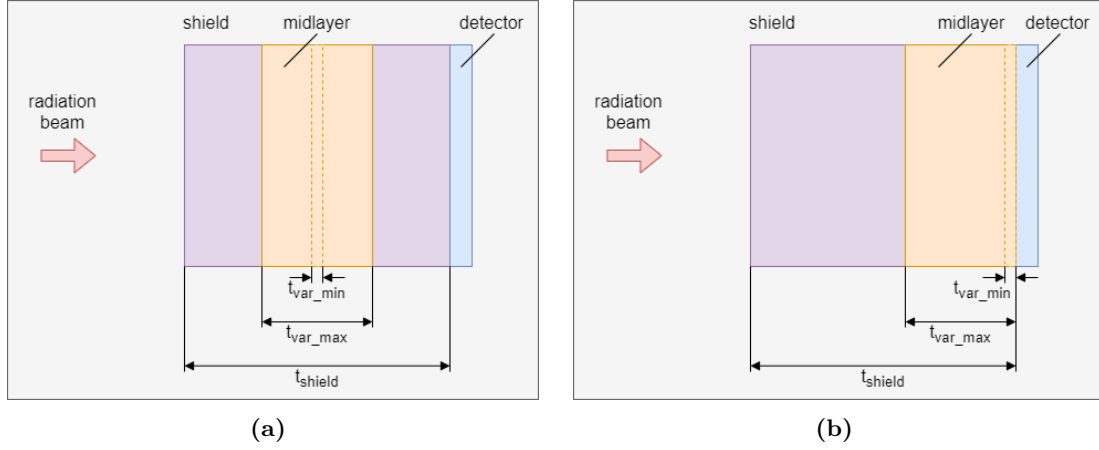


Figure 18: 2D representation of the simulation setup for the (a) middle layer and (b) inner layer case consisting of a pure polymer or MGS-1 and polymer composite with varying concentrations.

These added layers are then run for thicknesses between 10 cm and 100 cm, in 10 cm increments. Furthermore, different concentrations of the MGS-1 and polymer composite are evaluated. LCP (Liquid Crystal Polymer) was chosen as the polymer because of its high radiation shielding performance among the polymers. If there are differences, the influence of a better performing polymer would make these differences more significant. To determine the density of the composite, the following formula for theoretical density is used:

$$\frac{1}{\rho_{composite}} = \frac{\phi_a}{\rho_a} + \frac{\phi_b}{\rho_b} \quad (14)$$

Where ρ is the density and ϕ the weight fraction. Subscripts a and b denote the composite constituent materials. The dose reduction results using different variables are shown in Table 8, 740 MeV neutron and 1 GeV proton beams.

Table 8: Dose reduction of middle and inner layers consisting of LCP polymer or MGS-1 and LCP composite at different concentrations for neutrons and protons.

Particle		Neutrons (740 MeV)				Protons (1 GeV)			
Thickness	LCP/ MGS-1	Middle layer		Inner layer		Middle layer		Inner layer	
		10 cm	100 cm	10 cm	100 cm	10 cm	100 cm	10 cm	100 cm
250 cm	0-100%	51%				82%			
	10-90%	51%	57%	49%	54%	83%	83%	83%	84%
	50-50%	49%	55%	51%	54%	83%	83%	83%	86%
	90-10%	50%	57%	49%	57%	83%	83%	83%	88%
	100-0%	50%	59%	51%	57%	84%	88%	84%	88%
300 cm	0-100%	68%				94%			
	10-90%	68%	69%	68%	69%	94%	95%	94%	95%
	50-50%	71%	72%	68%	71%	95%	97%	95%	97%
	90-10%	69%	75%	69%	73%	95%	97%	95%	97%
	100-0%	70%	75%	69%	74%	95%	97%	95%	97%
400 cm	0-100%	88%				99%			
	10-90%	90%	89%	89%	90%	99%	99%	99%	99%
	50-50%	90%	90%	89%	90%	99%	99%	99%	99%
	90-10%	90%	91%	90%	91%	99%	99%	99%	99%
	100-0%	89%	91%	90%	91%	97%	97%	99%	99%

Table 8 shows that the influence of LCP or the LCP/MGS-1 composite has nearly no effect on the dose reduction for a shield thickness of 400 cm. Also for 250 cm and 300 cm, the effect on the dose reduction is rather small. It is expected that for helium and heavy ions the addition of a polymer or composite layer in a moderately thick regolith shield would not result in significant dose reduction gains. This is an important finding and even more so when the complexity of transporting polymers to Mars is taken into account; it simply is not worth the effort at this moment. It should also be noted that these situations consider an MGS-1 density of 1.29 g/cm^3 , which is the lower density limit. With an increased density, such as the upper limit of 2.49 g/cm^3 , dose reduction gains are even less significant or may even lead to worse results due to the lower density of the composite or polymer relative to the pure regolith parts of the shield. One reason why it is still interesting to use polymers is because of their material properties. The use of polymers could enhance the structural integrity of a Martian habitat and acts as a binder for regolith when additive manufacturing purposes are considered. However, enhanced material properties of polymers for structural integrity is considered out of scope for this work.

3.2 Dose reduction of MGS-1

The previous section showed that different density values between polymers can lead to significant differences in dose reduction. Due to the conclusion that the inclusion of a polymer layer in the shield does not lead to significantly improved dose reductions, only MGS-1 is considered further. With the upper and lower limit of MGS-1 discussed previously, the dose reductions from the selected 1 GeV (740 MeV for neutrons) radiation particle types are simulated and assessed. Furthermore, intermediate density values are also included in order to observe the differences between these various values. The density values considered are: 1.00 g/cm^3 , 1.29 g/cm^3 , 1.50 g/cm^3 , 2.00 g/cm^3 and 2.49 g/cm^3 . All the dose reduction values for all considered MGS-1 densities, particle types, and shield thicknesses are included in Appendix F. Starting with neutron beams, the dose reduction is shown in Figure 19.

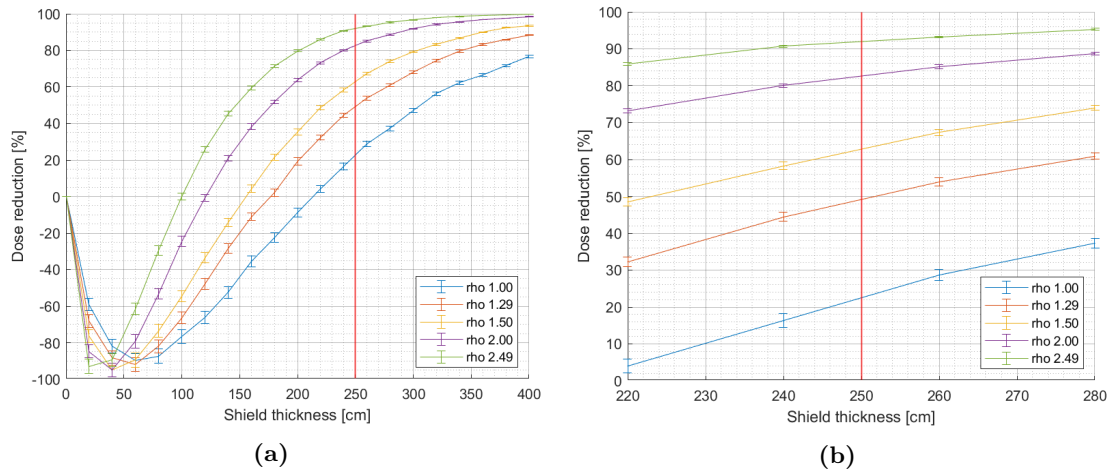


Figure 19: Dose reduction for different MGS-1 densities (in g/cm^3) from a 740 MeV monochromatic neutron beam with a shield thickness range of (a) 0-400 cm and (b) 220-280 cm.

Similar to Figure 16a, lower densities have a smaller dose increase than higher densities for the first few tens of cm, shown more in detail in Figure 20. With increasing thicknesses from about 40 cm and 60 cm, a steep increase in dose reduction is observed, which gradually flattens out. The importance of adequate shielding also becomes clear in Figure 20. For all densities a dose increase up to nearly 100% takes place initially and for the lowest density of 1.00 g/cm^3 . The actual dose reduction starts at a shield thickness of 215 cm, while this is at 100 cm for the highest density of 2.49 g/cm^3 . Even with the chosen shield thickness of 250 cm, the difference between the lowest and highest density is about 70% which is considered excessive. It should also be emphasized that the energy of 740 MeV is the upper limit of the neutron energy spectrum but occurs seldom.

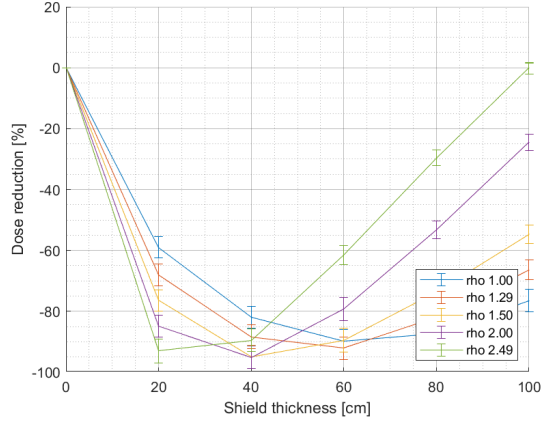


Figure 20: Dose reduction for different MGS-1 densities (in g/cm^3) from a 740 MeV monochromatic neutron beam with a shield thickness range of (a) 0-100 cm.

Also for proton beams, shown in Figure 21, a dose increase up to $\sim 20\%$ takes place first. However, this transforms quickly to a dose increase at about 110 cm for the lowest density and already at 45 cm for the highest density. Except for the lowest density, an almost full dose reduction of the proton beam is achieved before 300 cm. Since protons contribute on average 17% to the absorbed dose (see Table 3), this is quite a positive effect. At 250 cm, the difference in dose reduction between the lowest and highest density is $\sim 33\%$.

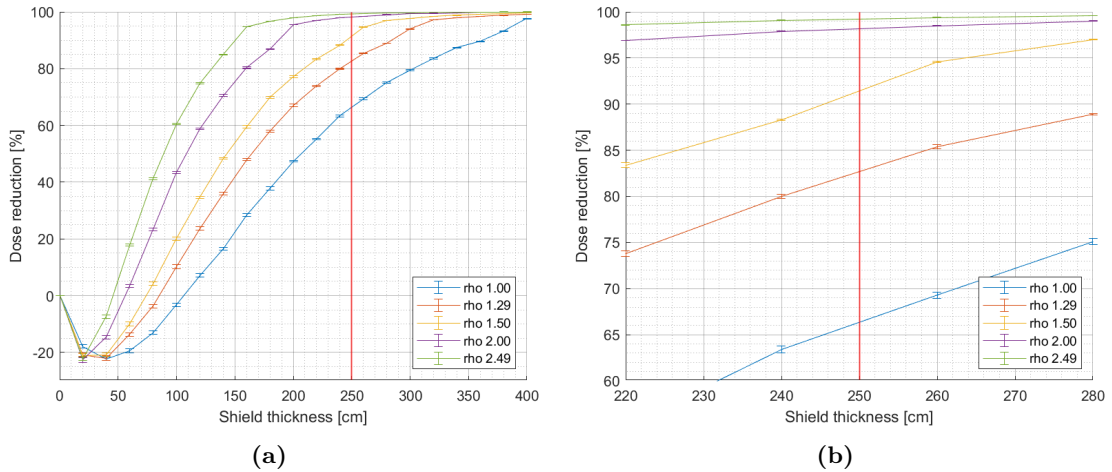


Figure 21: Dose reduction for different MGS-1 densities (in g/cm^3) from a 1 GeV monochromatic proton beam with a shield thickness range of (a) 0-400 cm and (b) 220-280 cm.

For 1 GeV helium beams, all densities have a very steep dose reduction increase before 60 cm of the shield thickness. They all already have a dose reduction above 90% at 60 cm, while at 250 cm this is already above 99%.

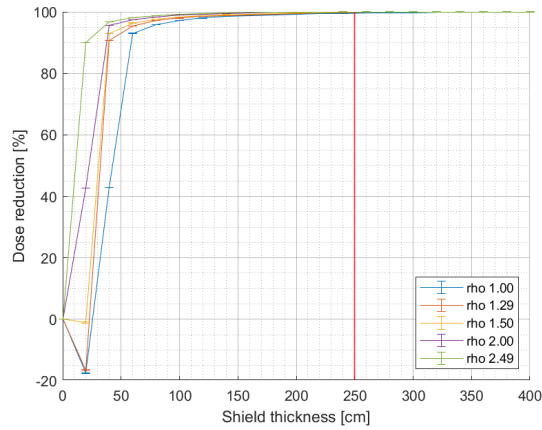
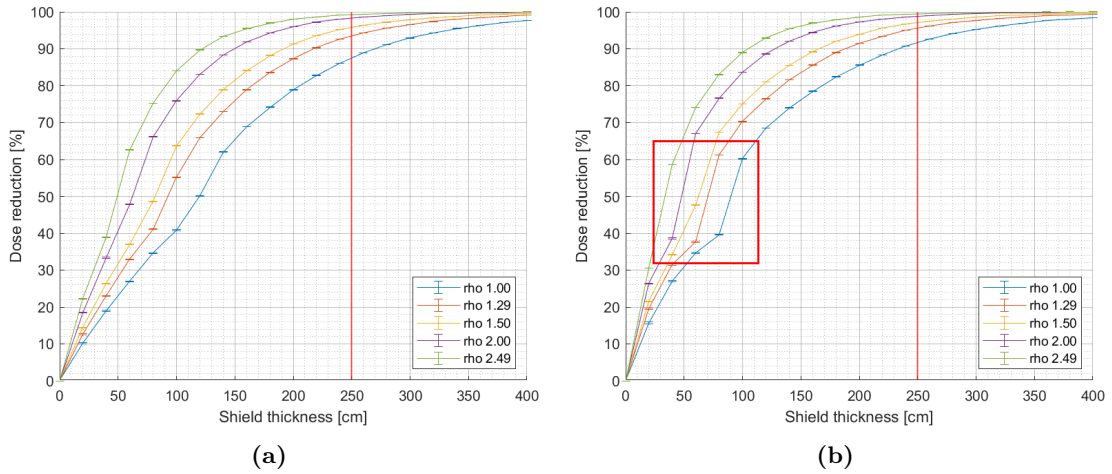


Figure 22: Dose reduction for different MGS-1 densities (in g/cm^3) from a 1 GeV monochromatic helium beam with a shield thickness range of 0-400 cm.

In the case of carbon, oxygen, silicon and iron beams, the dose reduction plots are shown in Figure 23. For all these HZE ions, an immediate dose reduction is observed at 20 cm and beyond. The increase in dose reduction appears to be slowing down and then accelerates again for carbon, oxygen and silicon (to a lesser extent), indicated by the red rectangle in Figure 23b for oxygen. However, the reason for this behaviour is not found. At a shield thickness of 250 cm, the dose reduction of all densities ranges between 87.5-99% for carbon, 91.5-99.5% for oxygen, 96-99.7% for silicon and 99.1-99.9% for iron. From this can be concluded that for HZE ions, high values of dose reduction are obtained for all considered densities. However, it is important to note that the contribution of, for example, iron to the total absorbed dose is much higher than carbon in absolute values. A specific dose reduction of iron may still mean a higher absorbed dose with respect to lower heavy ions.



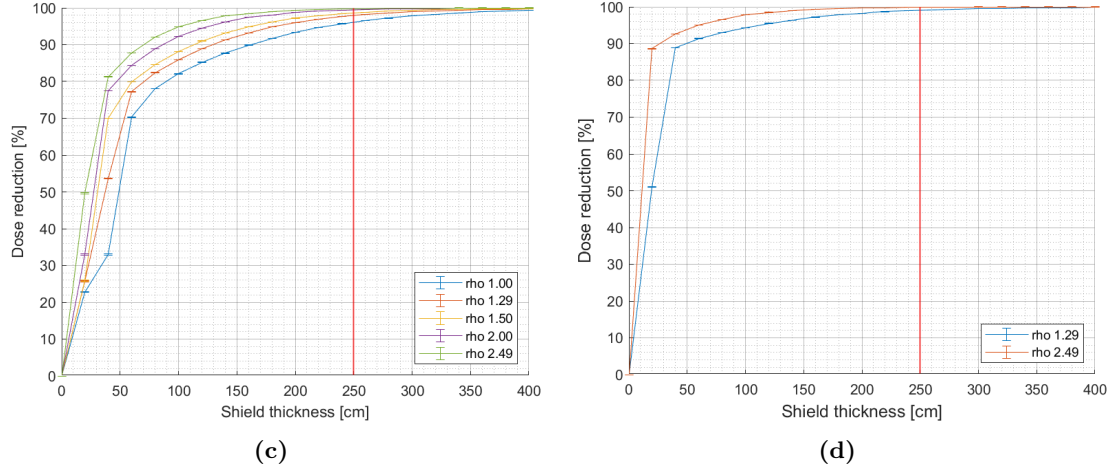


Figure 23: Dose reduction for different MGS-1 densities (in g/cm^3) from a 1 GeV monochromatic (a) carbon, (b) oxygen, (c) silicon and (d) iron beam with a shield thickness range of 0-400 cm.

3.3 Different energies

Different energy levels of neutrons, protons, helium and carbon are also assessed. This is done by looking at the absorbed dose inside the MGS-1 shield with a density of $1.29 \text{ g}/\text{cm}^3$. First, the average differential fluxes of all chosen particle types during the five solar minima from OLTARIS are calculated and plotted in Figure 24. Next, the energy level at which the highest flux occurs is determined and shown in Table 9, together with other assessed energy levels. Simulations for oxygen, silicon and iron are not simulated due to the required computational power, as well as a limited time constraint.

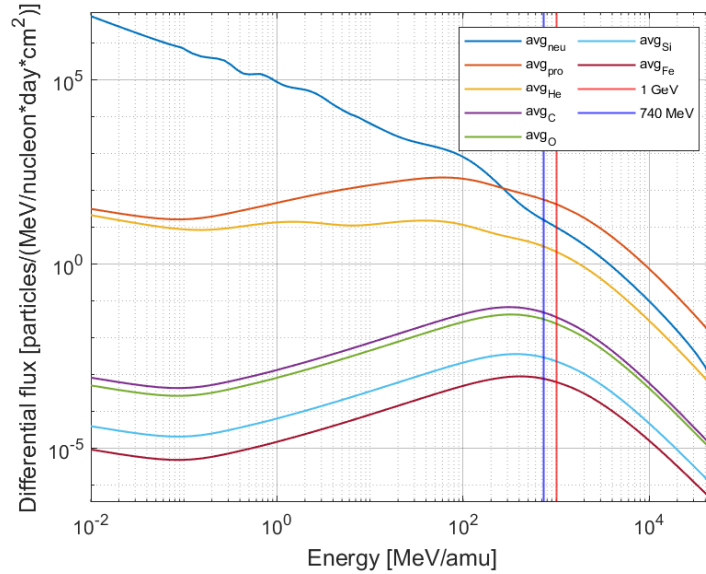


Figure 24: Combined energies for an MGS-1 shield with $1.29 \text{ g}/\text{cm}^3$ density and a thickness range of 0-400 cm.

Table 9: Energies at the highest flux per particle type.

Particle type	Energy at highest flux	Other assessed energies
Neutrons	~1 MeV*	[10, 100, 250, 500, 740] MeV
Protons	~60 MeV	[100, 250, 500, 750] MeV, [1, 5, 10] GeV
Helium	~40 MeV**	[100, 500] MeV, [1, 5, 10] GeV
Carbon	~315 MeV	[100, 500] MeV, [1, 5, 10] GeV
Oxygen	~315 MeV	not applicable
Silicon	~360 MeV	not applicable
Iron	~405 MeV	not applicable

**taken as 'lowest' energy, **this is the second highest flux*

Figure 25 shows the progression of the absorbed dose through the shield, with the vertical line representing the 250 cm shield for neutrons, protons, helium and carbon, respectively. For all these particle beams, most increases occur at the beginning, which confirms that most of the radiation is absorbed at the outer shield layers.

For higher energies such as 5 GeV and 10 GeV, most of the dose absorption takes place deeper in the shield. For neutrons, even at lower energies such as 10 MeV and 100 MeV, the dose absorption is less effective at any shield thickness after the peak. Very steep peaks can be observed at lower energies for protons, helium and carbon. The physics phenomenon which gives rise to these peaks is called a Bragg curve and it is characteristic for radiation in materials and shields. These curves represent how a charged particle moves through matter while leaving a certain dose behind. The deeper and longer it penetrates in a material, the higher the probability of interactions. During these interactions, the particle loses increasingly more energy while slowing down at the same time, where the energy loss is inversely proportional to the velocity squared (*Zeitlin, Guetersloh, Heilbronn, and Miller, 2006*). This means that when the particle slows down because of the interactions, it deposits more dose into the shield up to the Bragg peak where suddenly most or even all radiation is lost by the particle and consequently comes to a rest, which is characterized by the sudden drop of the peak.

In the case of protons, see Figure 25b, all radiation is lost after this Bragg peak. In the case of helium and carbon (Figures 25c and 25d), a drop can be observed but evolves into a tail. For elements with $Z=3$ and higher, the particle fragments into lower Z particles with lower energies. Evidently, for higher Z ions, particles can continually fragment more into lower Z ions. Before the Bragg peak, the carbon dose first decreases and then increases back toward the peak, while for helium it increases immediately (*Zeitlin and La Tessa, 2016*). This is because carbon fragments more easily into lower Z elements that eventually fragment themselves. The sum of these energies is always lower than the energy of the initial particle. The increase in the case of helium indicates that helium has not fragmented before the peak and is able to penetrate deeper into the shield before fragmenting (*Brookhaven National Laboratory, n.d.*).

It is important to mention that the highest peaks, seen in Figure 25, for neutrons, protons, helium and carbon reach values of about 4.25×10^{-21} , 5.0×10^{-20} , 1.0×10^{-19} and 6.5×10^{-19} , respectively. This gives a better understanding of the order of magnitude between them. Concerning Bragg peaks, it is paramount that Bragg peaks occur completely inside the shield for the entire particle type and energy spectrum experienced on the Martian surface. If a shield is too thin, there is a risk that these peaks lie partially or completely behind the shield with devastating consequences. Finally, it occurs that the absorbed dose at a Bragg peak has a comparable or higher value than a higher energy beam of the same particle. For protons, the highest absorbed doses of a 100 MeV and 5 GeV are almost equal as can be observed in Figure 25. For helium, the peak value is higher for a 100 MeV, 500 MeV and 1 GeV beam compared to a 5 GeV and 10 GeV beam. For carbon, 315 MeV and 500 MeV reach a higher absorbed dose value than its 10 GeV counterpart and similarly, a 1 GeV beam has a higher

peak than a 5 GeV beam. However, the radiation beams for lower energies that have higher peak values are attenuated much earlier in the first layers of the shield while for higher energy beams this is much deeper into the shield. This emphasizes the complexity of designing a shield to protect against all radiation present on Mars.

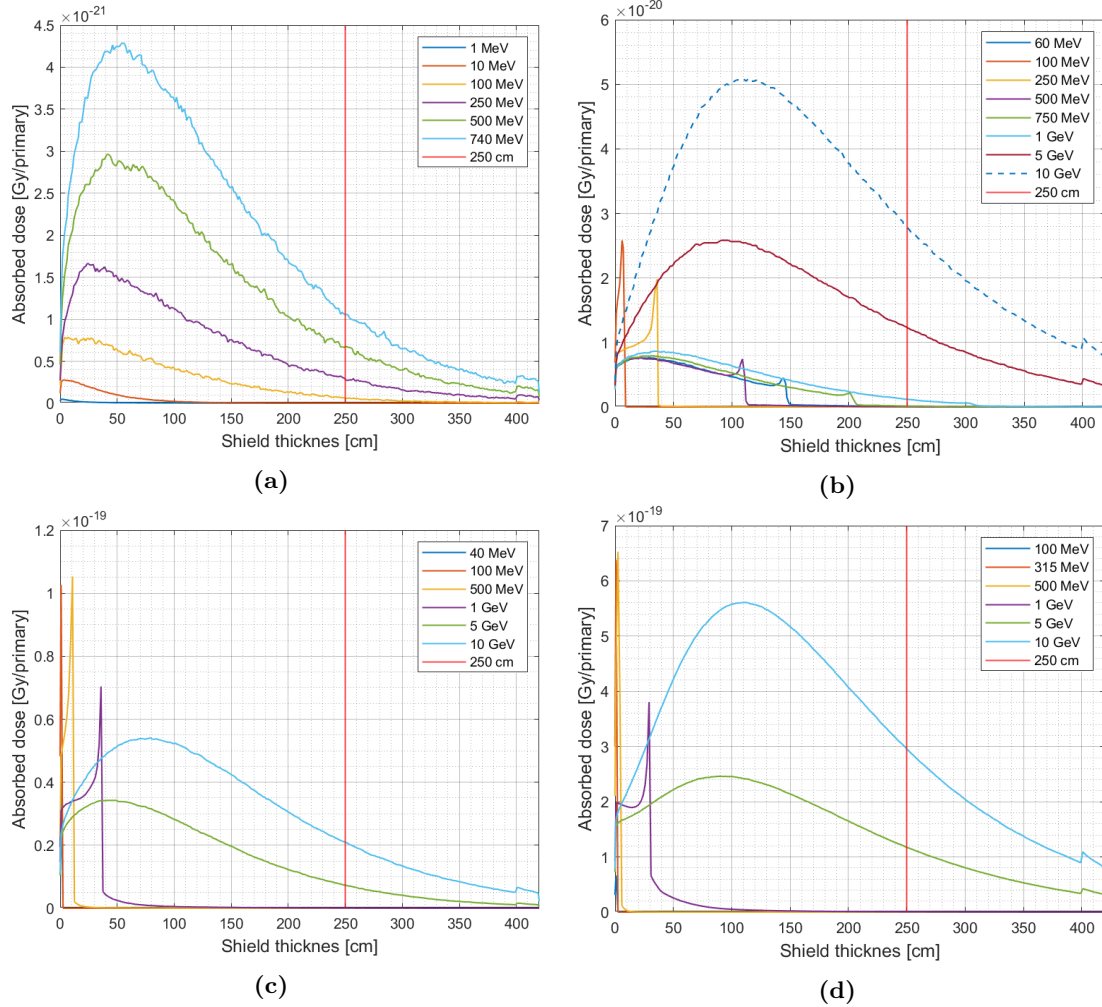


Figure 25: Absorbed dose in an MGS-1 shield with a maximum thickness of 400 cm for (a) neutron, (b) proton, (c) helium and (d) carbon beams at different energies.

3.4 Dose reduction overview for several MGS-1 shield thicknesses

All dose reduction results of the assessed particle types at 1 GeV and 740 MeV for neutrons are combined and shown for the lower and upper MGS-1 densities in Table 10 and Figure 26. For the lower density limit at 250 cm, the dose reduction of neutrons is about 50%, 82% for protons and more than 94% for helium and HZE ions. For the upper density limit at 250 cm, a dose reduction of at least 92% is achieved for all considered particles. This highlights the importance of using high-density materials. At a density of 1.29 g/cm^3 , a shield thickness of 250 cm appears to be insufficient. However, these dose reductions are only for monochromatic beams and not for the energy spectrum of the particle types, as well as their contributions to the total integral flux, as discussed in Section 2.3. Once the energy spectrum and contributions have been applied to the simulations, a more substantiated conclusion can be drawn. The first steps of this approach are carried out in the section hereafter.

Table 10: Dose reduction for all chosen particles for a 200 cm, 250 cm, 300 cm, 400 cm MGS-1 shield with a density of 1.29 g/cm³ and 2.49 g/cm³.

Density [g/cm ³]		1.29				2.49			
Shield thickness [cm]		200	250	300	400	200	250	300	400
Neutron	740 MeV	19%	51%	68%	88%	80%	92%	97%	100%
Proton	1 GeV	67%	82%	94%	99%	98%	99%	100%	100%
Helium		99%	100%	100%	100%	100%	100%	100%	100%
Carbon		87%	94%	97%	99%	98%	100%	100%	100%
Oxygen		91%	96%	98%	99%	99%	100%	100%	100%
Silicon		96%	98%	99%	100%	99%	100%	100%	100%
Iron		98%	99%	100%	100%	100%	100%	100%	100%

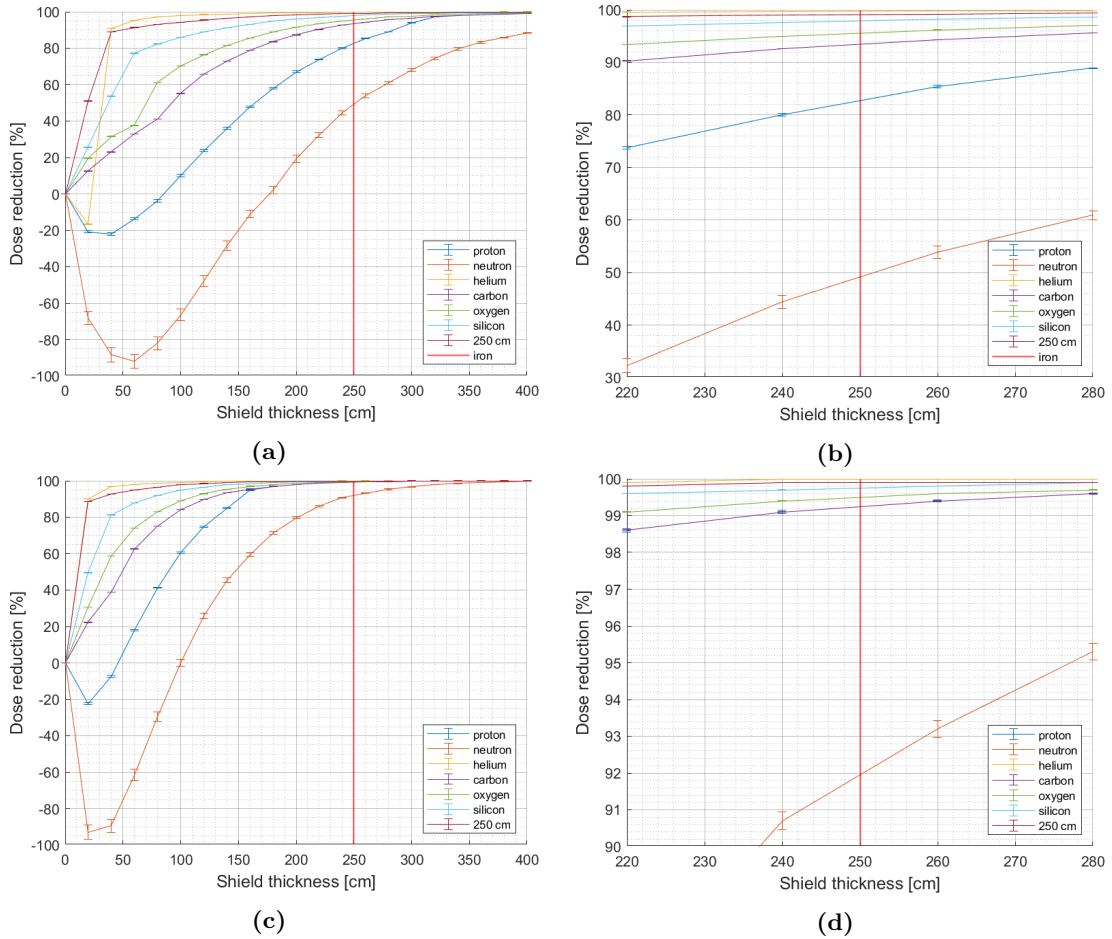


Figure 26: Dose reduction for the monochromatic beams of all considered elements with their respective energies for an MGS-1 shield with (a), (b) 1.29 g/cm³ and (c), (d) 2.49 g/cm³ density with a maximum shield thickness of 400 cm.

4 Radiation shielding of a Mars habitat

4.1 Habitat design

A habitat for humans has been designed to make a more realistic mission scenario on Mars. This design should be simplified as the results will provide for a first assessment of the radiation shielding and can serve as a reference point, after which subsequent work should include further iterations of the design. The shape and dimensions are mainly based on references elaborated below.

The basic design is derived from *Kading and Straub, 2015* where several dome designs are proposed, and the chosen dome geometry is based on a modular work and living unit. This geometry should be sufficient for the astronaut to work and live in. Note that this dome is intended to be 3D printed from basalt, therefore its thickness is not used in this Mars habitat design. The dome is made of aluminium with a thickness of 1.5 cm, which is reported in *Vuolo, Baiocco, et al., 2017* for reproducing a spacecraft wall. This thickness is determined for both the dome wall and floor. The dome is then covered by MGS-1 with a thickness of 250 cm, as mentioned in Section 2.5. Its density is uniform and chosen to be 1.9 g/cm^3 . This value is reached as the average rounded value between the lower and upper density limit described in Section 2.4. Taking the lower density limit would be an underestimation of the MGS-1 shield because this is the bulk density, while the upper density limit could result in a habitat design with an overestimated density value.

Inside the dome, three cylindrical water phantoms, i.e. detectors, are placed at different locations. These water phantoms represent human bodies and serve as detectors of the absorbed dose such that the dose reductions can be calculated consistently. One water phantom is placed in the center of the dome, while the two other phantoms are placed further from the center, one of which is close to the dome wall. The height of the water phantoms is taken to be 190 cm, as this is the maximum height ESA allows for astronauts (*ESA, 2021*), while NASA has an astronaut height limit of 75 inches, i.e. 190.5 cm (*NASA, 2011*). Using the maximum astronaut height also means that the absorbed dose is essentially a worst-case scenario with respect to the height, as shorter people will receive less radiation because of their smaller body volume. The radius of the cylinders is 30 cm, as this is often taken as the radius of the average human body. Air is present inside the dome for the obvious reason that humans need to breathe. Combining all the design considerations and choices results in the habitation structure shown in Figure 27.

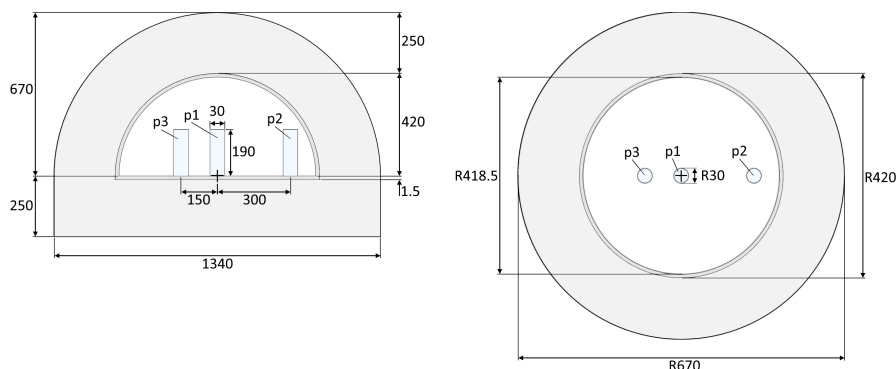


Figure 27: Dimensions (in cm) of the habitat used for the FLUKA simulations. The phantoms are denoted by p . Note that the thickness of the aluminium shell is not to scale.

4.2 Final simulation preparations and simplifications of the GCR event

As already mentioned in Section 2, a GCR event during a solar minimum is chosen instead of a historical SPE. Furthermore, it was also shown by Table 3 that the particle type contributions are almost identical during the past five solar minima. For this reason, an averaged GCR event with its corresponding contributions will be used for the simulation. Instead of using monochromatic beams as

done in Section 3, energy spectra of the chosen particle types are used and implemented in FLUKA. Although FLUKA allows to simulate particle beams according to energy spectra, this can only be done for one particle type at a time. Therefore, the individual particle type contributions for an averaged GCR event, shown in Table 11, are used. The integral flux in this table represents particle types with a single atomic charge and atomic weight. This is another simplification because the OLTARIS output also includes particle types with different atomic weights for a specific atomic charge. For all particle types, there is always clearly a larger contributor in terms of atomic weight. Consequently, all integral fluxes for each specific atomic charge with different atomic weights are added together and run for the atomic weight of the largest contributor.

Table 11: Contribution of the chosen particle types to the total integral flux, expressed in terms of integral flux and contributions (in %).

Particle type	Integral flux [particles/(day·cm ²)]	Contribution [%]	Total integral flux [particles/(day·cm ²)]
Neutrons	7.8315E+05	8.2119E-01	9.5368E+05
Protons	1.6196E+05	1.6983E-01	
Helium	8.3800E+03	8.7870E-03	
Carbon	1.0698E+02	1.1218E-04	
Oxygen	7.1063E+01	7.4514E-05	
Silicon	6.7840E+00	7.1135E-06	
Iron	1.9148E+00	2.0078E-06	

Due to practical complications and time constraints, the GCR event is simplified using different interpretations. First, the particle beams are divided into nine concentrated beams, instead of random sampling around the habitat that better represents a GCR event as shown in Figure 28a. It should be noted that this simplified setup by no means accurately simulates a GCR, but rather serves as a first assessment to gain a better understanding of the dose reduction following a simplified GCR event. These beams are radially divided from 18° to 162° with respect to the horizontal and at equal intervals of 18°. Furthermore, they are directed at the center of the habitat where the middle phantom is located, shown in Figure 28b. There are no beams included between 0°-18° and 162°-180° to take into account that radiation beams will not hit the habitat in this setup if they are directed towards the center.

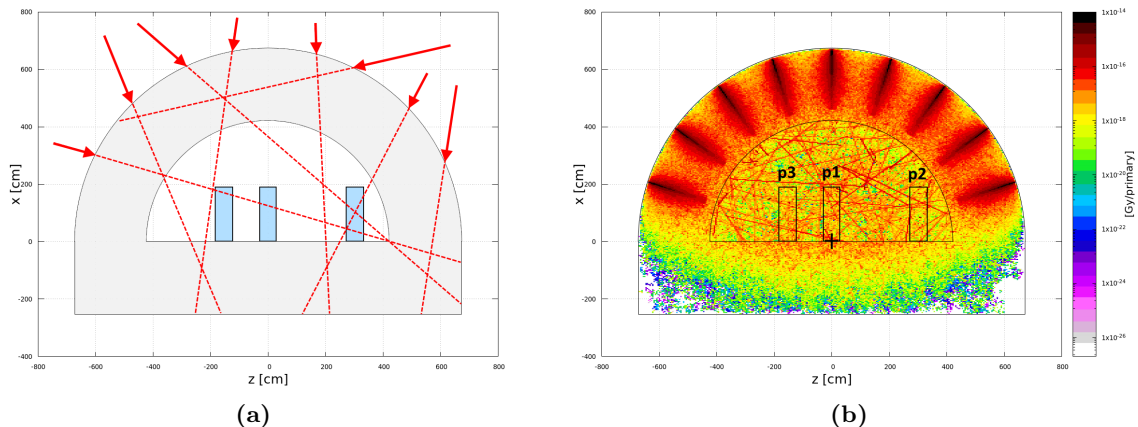
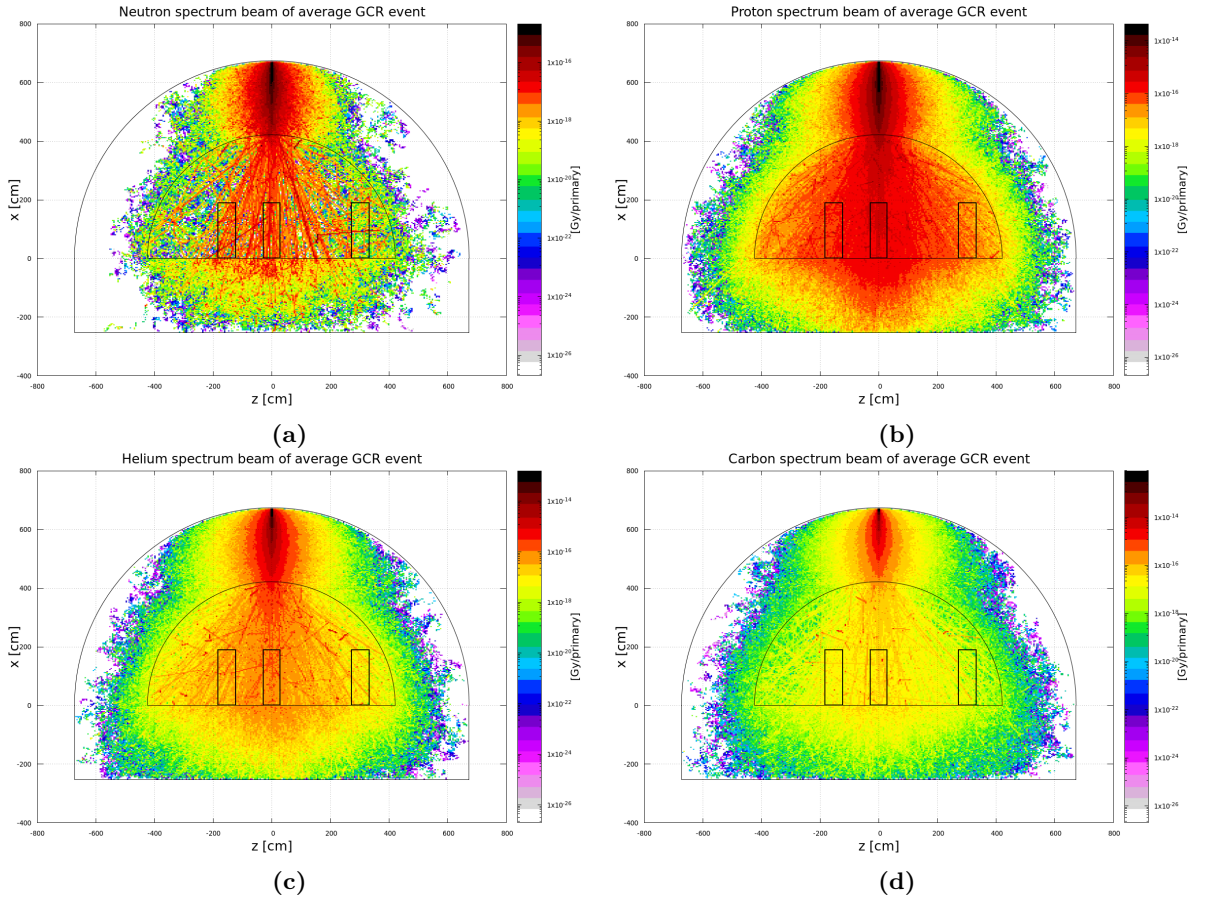


Figure 28: (a) Illustration of in-plane randomly distributed GCR beams impinging on the habitat outer layer with varying directions and (b) division of nine 1 GeV proton beams directed to the center of the habitat. The habitat and phantom contours (denoted by *p*) are displayed as well.

Furthermore, the calculated integral flux using Equation 10 is expressed in $[particles/(day \cdot cm^2)]$. To determine the total number of particles hitting the habitat, it is also necessary to determine the surface area that is exposed to this radiation. It is assumed that equal surface areas are exposed to each of the nine beams. Following this, the first beam at an angle of 18° towards the center will be constrained to the surface area stretching from 9° to 27° . The surface area of the second beam is bounded by 27° and 45° , etc. This results in a total surface area between 9° and 171° . Based on the habitat geometry seen in Figure 27 and the formula for a spherical cap, the exposed surface area is calculated and equals $2.3793 \times 10^6 \text{ cm}^2$.

4.3 Final simulation results and discussion

With the preparations and simplifications discussed in the previous section, the FLUKA simulations are carried out. The dose propagation of each of the selected particle types for a single particle hitting the habitat is shown in Figure 29. The propagation in this figure hits the habitat atop, while simulations are run for each of the nine angled beams. Figure 30 depicts the separate simulations for the nine beams using the neutron GCR spectrum.



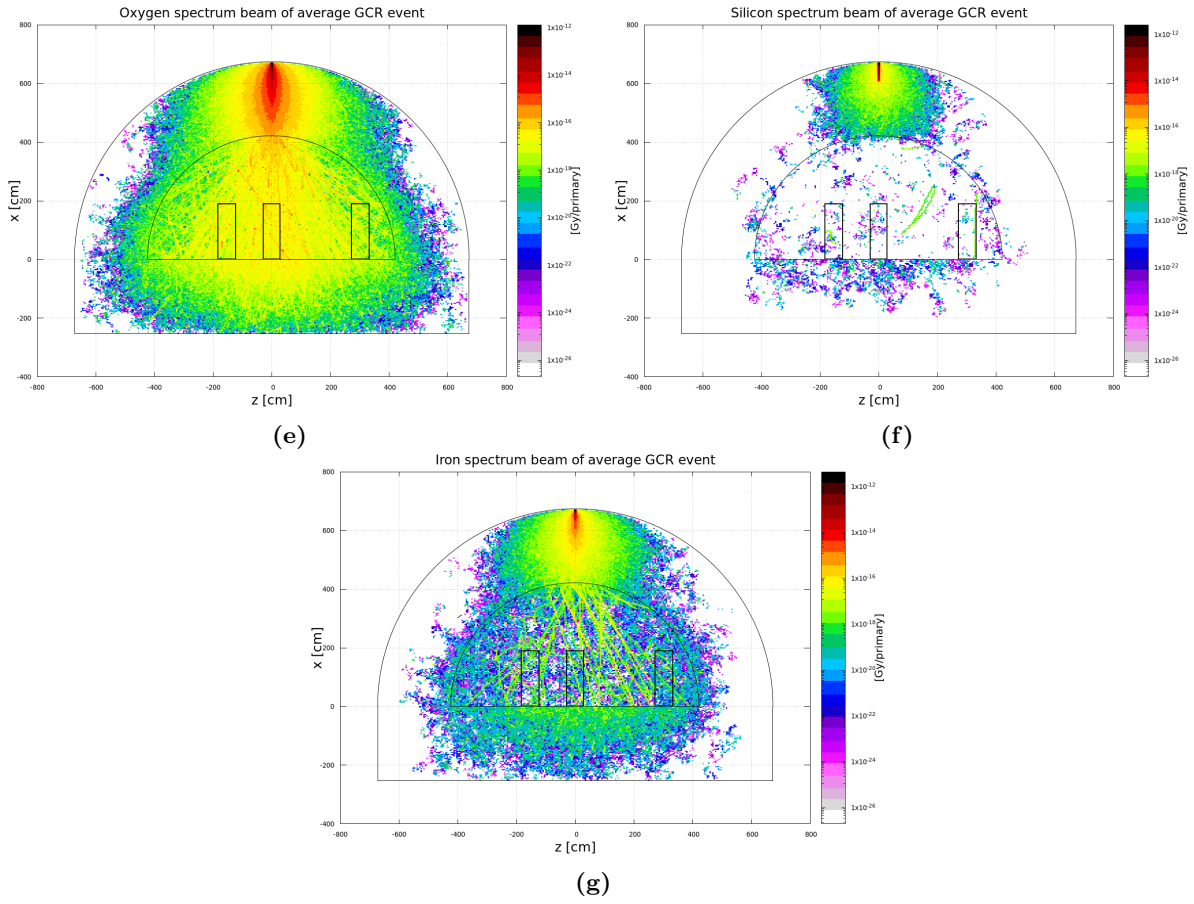
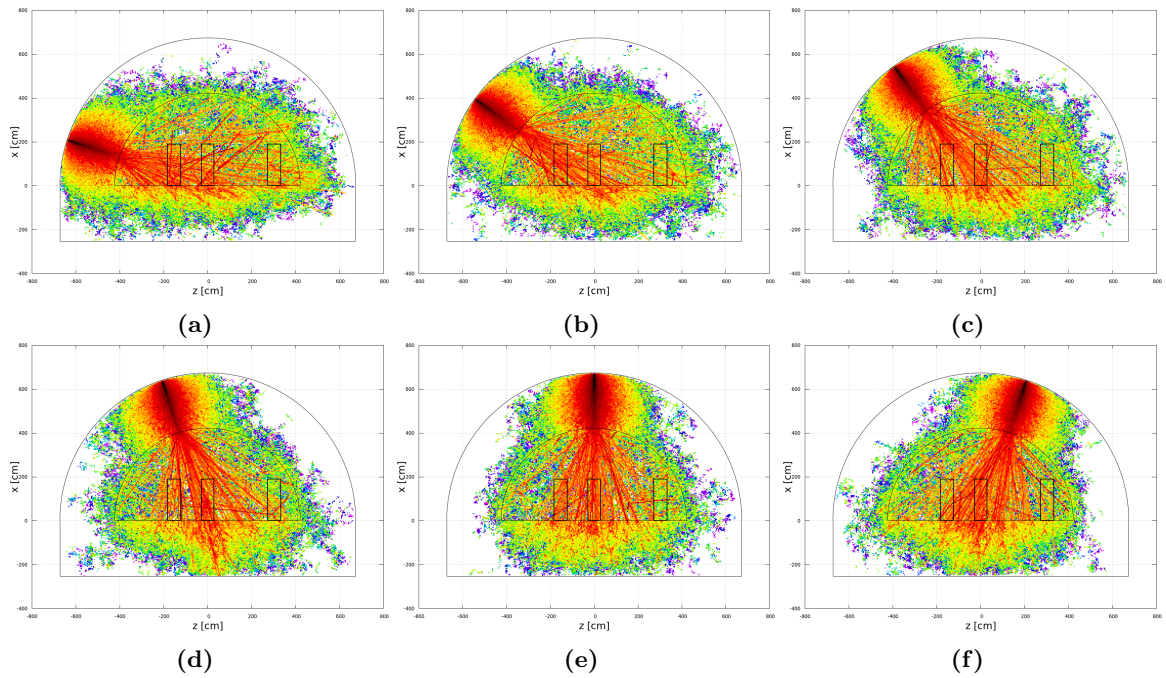


Figure 29: Dose propagation of a single particle hitting the habitat atop for the GCR energy spectra of (a) neutrons, (b) protons, (c) helium, (d) carbon, (e) oxygen, (f) silicon and (g) iron. Note that the color bar values are not equal to each other and differ by some orders of magnitude between neutrons, protons and HZE ions.



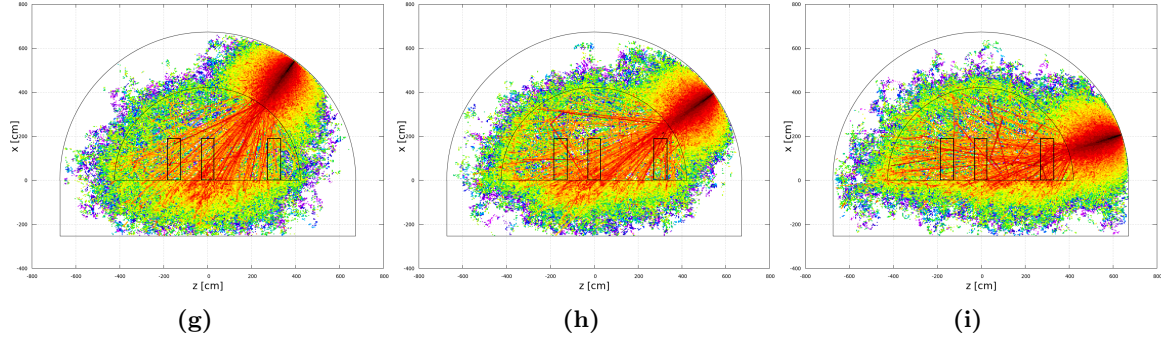


Figure 30: Dose propagation of a single neutron particle for the nine beams at angles from 18° to 162° in steps of 18° with respect to the horizontal, directed to the center with the average GCR energy spectrum during a solar minimum.

Figures 29a and 30 show that the regolith shield absorbs a large portion of the dose for neutrons. Still, a significant amount of relatively high radiation doses still reach the interior of the habitat. This is an important observation because, unlike other radiation particles, neutrons can make objects radioactive through neutron activation (*NRC, 2020*). In addition, neutrons can more easily penetrate through other materials and only interact with atomic nuclei because they are not charged as mentioned previously in Section 1. Moreover, neutrons can easily propagate through the air that is present inside the habitat (*NRC, 2020*) and interact more with the hydrogen nucleus of the water phantom, which adds another level of complexity. Although the doses are about two orders of magnitude lower than protons and four orders of magnitude lower than the heavy ions, they still cause extensive biological damage even in the case of low-energy neutrons. In this context, the use of polymers as an inner shield layer may again become critical, which could further attenuate the lower energy neutrons that have passed through the regolith shield. Another option is to increase the regolith shield thickness. However, this can be investigated more accurately once a realistic GCR event has been reproduced and ran in FLUKA. The straight lines that can be observed are thought to be higher energy particles from the interactions between the particle and material, thus having higher kinetic energies.

For protons and helium shown in Figures 29b and 29c respectively, the regolith shield has reduced the dose by about two orders of magnitude. However, the dose stretches out again inside the shield in both cases albeit smaller dose values for helium. For the HZE ions in Figures 29d, 29e, 29f and 29g dose reductions by many orders of magnitude are observed, more than in the case of neutrons, protons and helium. Table 12 presents the dose reduction of the nine beams combined during one day per particle type. These have been determined from the results of the FLUKA simulations and Table 11. From Table 12, it can be seen that the dose reduction for all chosen particle types is higher than 95%, some even close to 100%. Relating these results to Figure 29, this means that although the radiation has propagated through the shield inside the habitat, it is significantly reduced. This is promising, as such high dose reductions per day imply that astronauts can be present in these habitats for long periods conforming to the ALARA principle. The location of the phantoms with respect to the dose reduction shows that phantom 1 in the center has the largest dose reduction. This is likely due to that all nine beams are directed at the center and phantom 1 will also in the case without the habitat, be exposed to these radiation beams. For phantoms 2 and 3, in the case without the habitat, they will not be exposed to all nine of these beams propagating through the vacuum as a slender beam. It is important to mention that the outside environment in FLUKA is the space vacuum because the OLTARIS output files already take into account the secondary neutrons from the atmosphere and surface. In the case of the habitat, phantoms 2 and 3 will still receive radiation from these beams resulting in radiation propagation in all directions after interactions with the shield. If the realistic GCR event is reproduced, not all beams would hit these phantoms and the resulting dose reduction values of the phantoms will be more accurate relative to each other.

Table 12: Dose and corresponding dose reduction per particle type for all phantoms per day.

Particle	Phantom	Dose [Gy/day]	δD	Particle	Phantom	Dose [Gy/day]	δD
neutron	P1	7.9420E-05	98.77%	O	P1	2.0776E-08	99.96%
	P2	4.6312E-05	95.10%		P2	1.7380E-08	99.83%
	P3	6.6878E-05	97.27%		P3	1.7640E-08	99.94%
proton	P1	5.2969E-04	98.04%	Si	P1	5.5203E-11	99.999%
	P2	2.6727E-04	92.24%		P2	1.6609E-11	99.999%
	P3	3.3481E-04	96.31%		P3	1.3524E-10	99.996%
He	P1	8.0814E-06	99.64%	Fe	P1	3.2536E-11	99.999%
	P2	5.5663E-06	98.45%		P2	3.6560E-11	99.992%
	P3	5.8804E-06	99.41%		P3	3.6853E-11	99.997%
C	P1	4.7489E-08	99.93%				
	P2	3.6187E-08	99.72%				
	P3	3.7600E-08	99.90%				

By combining all the absorbed doses per particle type for each phantom, the total dose reduction is determined. This is shown in Table 13, which also includes the absorbed dose, normalized dose and its relative error. The normalized dose is another way of representing the dose reduction, which is the absorbed dose with shield divided by the absorbed dose without shield:

$$D_{norm} = \frac{D_{shield}}{D_{no_shield}} \quad (15)$$

Values resulting from Equation 15 that are less than 1 indicate a dose reduction and values greater than 1 indicate a dose increase. The error is calculated using Equation 8. The results from Table 12 have been overestimated to some extent due to all of the nine concentrated beams that are aimed at the center. When the distribution is truly random and a bombardment during a GCR event is more accurately represented, not every beam will be directed to the center, as discussed earlier.

Table 13: Combined dose reduction per phantom per day.

Phantom	Dose [Gy/day]	D_{norm}	δD
1	6.1726E-04	0.0172 \pm 1.81%	98.28%
2	3.1920E-04	0.0669 \pm 2.29%	93.31%
3	4.0762E-04	0.0324 \pm 2.14%	96.79%

Table 13 shows that the dose reductions for each phantom are very high. The highest dose reduction is attained at the center where phantom 1 is located, followed by phantom 3 and phantom 2 respectively.

5 Conclusions

This work investigated the radiation shielding capabilities of Martian regolith simulant MGS-1 as well as several other polymers and reference materials by determining the dose reduction. First, the Martian

radiation environment is analyzed using the online OLTARIS tool. From the differential fluxes output for historical SPE and GCR during solar minima, the contributions of neutrons, protons, helium and heavy ions from lithium to nickel are determined. For GCR, these contributions from the past five solar minima are almost equal to one another and thus the averaged values of these five are taken. Neutrons are by far the largest contributor on Mars, accounting for $\sim 81.10\%$ of the total integral flux, followed by protons, helium and heavy ions at $\sim 16.98\%$, $\sim 0.88\%$ and $\sim 0.04\%$ respectively. For SPE, the contributions may differ largely due to the varying intensity of such events. When comparing the particle and energy spectra between GCR and SPE fluxes, GCR also contains heavy ions while SPE does not. Moreover, the energy range of GCR goes much higher than for SPE, namely 50 GeV versus 2.5 GeV. Therefore, the shielding habitat design is based on GCR, as this would also provide adequate protection against SPE radiation. The dominant contribution of secondary radiation neutrons also emphasizes the importance of taking them into consideration when designing for radiation shielding, as both low and high-energy neutrons have detrimental biological effects on the human body and can easily penetrate shields.

A sensitivity analysis was performed on MGS-1 shields, polymers and other reference materials. Dose reductions were calculated for monochromatic 740 MeV neutron beams and 1 GeV proton, helium and carbon beams. When comparing MGS-1 to polymers, the performance lies within the range of the best and worst performing polymer for thicknesses up to 200 cm in the case of neutrons and protons, and up to 100 cm for helium and carbon. This is an important finding because although MGS-1 does not outperform certain polymers, it still is an effective material to shield radiation. Regolith will ultimately be used on Mars and is available as a quasi infinite material source, making it attractive to use as a radiation shield. Furthermore, the density effect of MGS-1 was assessed for monochromatic 740 MeV neutron and 1 GeV proton, helium, carbon, oxygen, silicon and iron beams for shield thicknesses up to 400 cm. It was found that higher densities significantly result in higher dose reductions for thicker shields, except for helium where almost 100% dose reductions are attained for shields thicker than 100 cm. The dose reductions at the chosen shield thickness of 250 cm for the lower density limit of 1.29 g/cm^3 are 51.15% for neutrons, 82.38% for protons, 99.75% for helium, 93.53% for carbon, 95.59% for oxygen, 97.92% for silicon and 99.09% for iron. Using the upper density limit of 2.49 g/cm^3 , the dose reductions are 91.80%, 99.22%, 99.97%, 99.28%, 99.50%, 99.76% and 99.89% respectively. Between these two density values, a significant increase for neutrons is observed. Referring back to the ALARA principle, anything that effectively results in higher dose reductions should be taken into account and density can play a major role in this. A 250 cm shield already leads to a significant dose reduction, but the feasibility and practicality of constructing thicker shields on Mars also needs further investigation.

Furthermore, the impact of adding a polymer as a middle or inner layer in the MGS-1 shield was assessed because polymers are effective in absorbing radiation due to their high hydrogen content. It was found that the effect of polymers for thick habitat shields, such as 250 cm, 300 cm and 400 cm did not result in significant dose reduction gains. Since a thick regolith shield on the Martian surface is essentially required, a middle or inner layer of a polymer is no longer necessary in this regard. This also omits the additional efforts required to get polymers on the Martian surface. However, the use of polymers can still be of interest in the context of creating bricks in combination with regolith through additive manufacturing for structural integrity reasons. Furthermore, as discussed previously, an inner polymer layer may be able to further absorb lower energy neutrons that have penetrated the regolith shield.

Finally, a simplified habitat is designed with an MGS-1 shield thickness of 250 cm, and energy spectra of the chosen particle types for an averaged GCR event during a solar minimum are used in the FLUKA simulations. This GCR event is a simplified case, where the radiation particles hitting the regolith shield are concentrated into nine beams that are aimed towards the center of the habitat instead of randomly sampled with different directions, i.e. an isotropic distribution. The dose reductions per particle type per phantom are all larger than 95%. For helium, carbon, oxygen, silicon and iron this even is close to 100%. Combining the dose reduction per phantom per day results in a dose reduction of 98.28% for phantom 1 in the center of the habitat, 93.31% for phantom 2, which is located at 300 cm from the center and closest to the habitat wall, and 96.79% for phantom 3, which is located at 150 cm from the center. In terms of normalized doses, these are $0.0172 \pm 1.81\%$, $0.0669 \pm 2.29\%$

and $0.0324 \pm 2.14\%$, respectively. The dose reduction is highest for phantom 1, followed by phantom 3 and worst for phantom 2. However, it cannot be inferred with certainty that phantom 2 has the worst dose reduction because it is closest to the wall and thus, closer to the outside environment due to the concentrated beam that are not randomly distributed. It is also important to note that this simplified GCR event is to some extent an overestimation of the absorbed doses of the phantoms and thus, an underestimation of the corresponding dose reductions. This again relates to all particles being concentrated in nine beams that are directed towards the center. In reality, it may occur that the path of such a particle does not cross the interior habitat.

6 Recommendation

The main recommendation for the next step is to develop the code that takes into account the entire particle type and energy spectra as well as the random sampling of these particles with varying directions around the Mars habitat, while being compatible with FLUKA, .

References

- [1] NASA. *OLTARIS: On-Line Tool for the Assessment of Radiation in Space*. Tech. rep. July 2010. URL: <https://oltaris.nasa.gov/links>.
- [2] M. Durante and F.A. Cucinotta. “Physical basis of radiation protection in space travel”. In: *Reviews of Modern Physics* 83.4 (2011), pp. 1245–1281. DOI: [10.1103/revmodphys.83.1245](https://doi.org/10.1103/revmodphys.83.1245).
- [3] N. Abuali Galehdari and A.D. Kelkar. “Characterization of Nanoparticle Enhanced Multifunctional Sandwich Composites Subjected to Space Radiation”. In: *Volume 1: Advances in Aerospace Technology* (2016). DOI: [10.1115/imece2016-66774](https://doi.org/10.1115/imece2016-66774).
- [4] NASA. *Why Space Radiation Matters*. 2019. URL: <https://www.nasa.gov/analogs/nsrl/why-space-radiation-matters/>.
- [5] G. Genta. *Next Stop Mars: The Why, How, and When of Human Missions*. 1st ed. Springer, 2017. DOI: [10.1007/978-3-319-44311-9](https://doi.org/10.1007/978-3-319-44311-9).
- [6] B. Kading and J. Straub. “Utilizing in-situ resources and 3D printing structures for a manned Mars mission”. In: *Acta Astronautica* 107 (2015), pp. 317–326. DOI: [10.1016/j.actaastro.2014.11.036](https://doi.org/10.1016/j.actaastro.2014.11.036).
- [7] G. De Angelis et al. “A new Mars radiation environment model with visualization”. In: *Advances in Space Research* 34.6 (2004), pp. 1328–1332. DOI: [10.1016/j.asr.2003.09.059](https://doi.org/10.1016/j.asr.2003.09.059).
- [8] M. Rais-Rohani. *On Structural Design of a Mobile Lunar Habitat with Multi-Layered Environmental Shielding (NASA/CR-2005-213845)*. Tech. rep. Apr. 2005. DOI: [10.13140/RG.2.1.3120.4962](https://doi.org/10.13140/RG.2.1.3120.4962). URL: https://www.researchgate.net/publication/280092103_On_Structural_Design_of_a_Mobile_Lunar_Habitat_with_Multi-Layered_Environmental_Shielding_NASACR-2005-213845.
- [9] S. Nambiar and J.T.W. Yeow. “Polymer-Composite Materials for Radiation Protection”. In: *ACS Applied Materials & Interfaces* 4.11 (2012), pp. 5717–5726. DOI: [10.1021/am300783d](https://doi.org/10.1021/am300783d).
- [10] O. C. Allkofer. *Introduction to cosmic radiation*. Tech. rep. 1975.
- [11] NCRP. *Guidance on Radiation Received in Space Activities*. Tech. rep. 098. 1989.
- [12] J.A. Simpson. “Elemental and Isotopic Composition of the Galactic Cosmic Rays”. In: *Annual Review of Nuclear and Particle Science* 33.1 (1983), pp. 323–382. DOI: [10.1146/annurev.ns.33.120183.001543](https://doi.org/10.1146/annurev.ns.33.120183.001543).
- [13] J.W. Wilson et al. “Transport Methods and Interactions for Space Radiations”. In: *Biological Effects and Physics of Solar and Galactic Cosmic Radiation Part B* (1993), pp. 187–786. DOI: [10.1007/978-1-4615-2916-3_12](https://doi.org/10.1007/978-1-4615-2916-3_12).
- [14] D. Rapp. “Radiation effects and shielding requirements in human missions to the moon and Mars”. In: *The Mars Journal* (2006), pp. 46–71. DOI: [10.1555/mars.2006.0004](https://doi.org/10.1555/mars.2006.0004).
- [15] J. Rask et al. *Space Faring: The Radiation Challenge Introduction and Module 1: Radiation Educator Guide*. Tech. rep. 2008. URL: <https://www.nasa.gov/stem-ed-resources/sf-radiation-challenge-hs-mod1.html>.
- [16] J.W. Norbury et al. “Advances in space radiation physics and transport at NASA”. In: *Life Sciences in Space Research* 22 (2019), pp. 98–124. DOI: [10.1016/j.lssr.2019.07.003](https://doi.org/10.1016/j.lssr.2019.07.003).

- [17] T. Berger et al. “Long term variations of galactic cosmic radiation on board the International Space Station, on the Moon and on the surface of Mars”. In: *Journal of Space Weather and Space Climate* (2020). DOI: [10.1051/swsc/2020028](https://doi.org/10.1051/swsc/2020028).
- [18] J. Guo et al. “Ready functions for calculating the Martian radiation environment”. In: *Journal of Space Weather and Space Climate* 9 (2019), A7. DOI: [10.1051/swsc/2019004](https://doi.org/10.1051/swsc/2019004).
- [19] C. Zeitlin and C. La Tessa. “The Role of Nuclear Fragmentation in Particle Therapy and Space Radiation Protection”. In: *Frontiers in Oncology* 6 (2016). DOI: [10.3389/fonc.2016.00065](https://doi.org/10.3389/fonc.2016.00065).
- [20] S. Gabriel. “Cosmic rays and solar protons in the near-earth environment and their entry into the magnetosphere”. In: 2000.
- [21] A. Meurisse et al. “Neutron radiation shielding with sintered lunar regolith”. In: *Radiation Measurements* 132 (2020), p. 106247. DOI: [10.1016/j.radmeas.2020.106247](https://doi.org/10.1016/j.radmeas.2020.106247).
- [22] J. Rask et al. *Space Faring: The Radiation Challenge - Introduction and Module 3: Radiation Countermeasures*. Tech. rep. 2008. URL: <https://www.nasa.gov/stem-ed-resources/sf-radiation-challenge-hs-mod3.html>.
- [23] F.A. Cucinotta. “Space Radiation Risks for Astronauts on Multiple International Space Station Missions”. In: *PLoS ONE* 9.4 (2014), e96099. DOI: [10.1371/journal.pone.0096099](https://doi.org/10.1371/journal.pone.0096099).
- [24] Lennart Röstel et al. “Subsurface Radiation Environment of Mars and Its Implication for Shielding Protection of Future Habitats”. In: *Journal of Geophysical Research: Planets* 125.3 (2020). DOI: [10.1029/2019je006246](https://doi.org/10.1029/2019je006246).
- [25] J.C. Chancellor et al. “Limitations in predicting the space radiation health risk for exploration astronauts”. In: *npj Microgravity* 4.1 (2018). DOI: [10.1038/s41526-018-0043-2](https://doi.org/10.1038/s41526-018-0043-2).
- [26] F.A. Cucinotta, M.Y. Kim, L.J. Chappell, et al. “How Safe Is Safe Enough? Radiation Risk for a Human Mission to Mars”. In: *PLoS ONE* 8.10 (2013), e74988. DOI: [10.1371/journal.pone.0074988](https://doi.org/10.1371/journal.pone.0074988).
- [27] F.A. Cucinotta, M.Y. Kim, and L. Ren. “Evaluating shielding effectiveness for reducing space radiation cancer risks”. In: *Radiation Measurements* 41.9-10 (2006), pp. 1173–1185. DOI: [10.1016/j.radmeas.2006.03.011](https://doi.org/10.1016/j.radmeas.2006.03.011).
- [28] B. Mukherjee et al. “Feasibility of a novel TLD based personal microdosimeter for dosimetry and risk assessment of astronauts enduring long-term habitat in space stations”. In: International Astronautical Federation. Sept. 2017, pp. 1–4.
- [29] E. Niiler. *NASA Wants to Set a New Radiation Limit for Astronauts*. Feb. 2021. URL: <https://www.wired.com/story/nasa-wants-to-set-a-new-radiation-limit-for-astronauts/>.
- [30] Ramin Skibba. *New Space Radiation Limits Needed for NASA Astronauts, Report Says*. July 2021. URL: <https://www.scientificamerican.com/article/new-space-radiation-limits-needed-for-nasa-astronauts-report-says/>.
- [31] L. Walsh et al. “Research plans in Europe for radiation health hazard assessment in exploratory space missions”. In: *Life Sciences in Space Research* 21 (2019), pp. 73–82. DOI: [10.1016/j.lssr.2019.04.002](https://doi.org/10.1016/j.lssr.2019.04.002).
- [32] S. McKenna-Lawlor et al. “Recommendations to mitigate against human health risks incurred due to energetic particle irradiation beyond low earth orbit/BLEO”. In: *Acta Astronautica* 109 (2015), pp. 182–193. DOI: [10.1016/j.actaastro.2014.11.009](https://doi.org/10.1016/j.actaastro.2014.11.009).
- [33] K. Mars. *Space Radiation Risks*. June 2018. URL: <https://www.nasa.gov/hrp/elements/radiation/risks/>.
- [34] C.V. More et al. “Polymeric composite materials for radiation shielding: a review”. In: *Environmental Chemistry Letters* (2021). DOI: [10.1007/s10311-021-01189-9](https://doi.org/10.1007/s10311-021-01189-9).
- [35] J.H. Adams et al. *Revolutionary Concepts of Radiation Shielding for Human Exploration of Space*. Tech. rep. 2005. URL: https://www.lpi.usra.edu/lunar/strategies/AdamsEtAl_NASA%20TM-2005-213688.pdf.
- [36] P. Spillantini et al. “Shielding from cosmic radiation for interplanetary missions: Active and passive methods”. In: *Radiation Measurements* 42.1 (2007), pp. 14–23. DOI: [10.1016/j.radmeas.2006.04.028](https://doi.org/10.1016/j.radmeas.2006.04.028).
- [37] Lawrence Townsend. “Overview of active methods for shielding spacecraft from energetic space radiation”. In: *Physica Medica* 17 (Feb. 2001), pp. 84–85.
- [38] S. Guetersloh et al. “Polyethylene as a radiation shielding standard in simulated cosmic-ray environments”. In: *Nuclear Instruments and Methods in Physics Research Section B: Beam Interactions with Materials and Atoms* 252.2 (2006), pp. 319–332. DOI: [10.1016/j.nimb.2006.08.019](https://doi.org/10.1016/j.nimb.2006.08.019).

- [39] L.C. Simonsen and J.E. Nealy. “Radiation protection for human missions to the Moon and Mars”. In: (Feb. 1991). URL: <https://www.osti.gov/biblio/5759477>.
- [40] A.I. Wozniak et al. “Modern Approaches to Polymer Materials Protecting from Ionizing Radiation”. In: *Oriental Journal of Chemistry* 33.5 (2017), pp. 2148–2163. DOI: [10.13005/ojc/330502](https://doi.org/10.13005/ojc/330502).
- [41] L. Heilbronn, J. Miller, and C. Zeitlin. “5.2.1 Fragmentation Physics and Spacecraft Shielding Studies”. In: *RADIOISOTOPES* 68.6 (2019), pp. 407–409. DOI: [10.3769/radioisotopes.68.407](https://doi.org/10.3769/radioisotopes.68.407).
- [42] R. Battiston et al. “Active Radiation Shield for Space Exploration Missions”. In: (Sept. 2012). DOI: [10.15161/oar.it/1449018317.78](https://doi.org/10.15161/oar.it/1449018317.78).
- [43] C. Zeitlin, S. Guetersloh, L. Heilbronn, J. Miller, et al. “Shielding experiments with high-energy heavy ions for spaceflight applications”. In: *New Journal of Physics* 10.7 (2008), p. 075007. DOI: [10.1088/1367-2630/10/7/075007](https://doi.org/10.1088/1367-2630/10/7/075007).
- [44] Haym Benaroya and Leonhard Bernold. “Engineering of lunar bases”. In: *Acta Astronautica* 62.4-5 (2008), pp. 277–299. DOI: [10.1016/j.actaastro.2007.05.001](https://doi.org/10.1016/j.actaastro.2007.05.001).
- [45] M. Vuolo, M. Giraudo, et al. “Monte Carlo simulations for the space radiation superconducting shield project (SR2S)”. In: *Life Sciences in Space Research* 8 (2016), pp. 22–29. DOI: [10.1016/j.lssr.2015.12.003](https://doi.org/10.1016/j.lssr.2015.12.003).
- [46] Ministry of the Environment. *BOOKLET to Provide Basic Information Regarding Health Effects of Radiation*. Tech. rep. Mar. 2013. URL: <https://www.env.go.jp/en/chemi/rhm/basic-info/>.
- [47] University of Florida. *Radiation Safety Short Course Study Guide*. Tech. rep. July 2011. URL: <https://www.ehs.ufl.edu/programs/rad/rssc/>.
- [48] P. Burns. *Draft ICRP Recommendations*. Oct. 2006. URL: <https://slideplayer.com/slide/7695777/>.
- [49] A. Ferrari et al. *Fluka: a multi-particle transport code*. Tech. rep. May 2021. URL: <http://www.fluka.org/content/manuals/FM.pdf>.
- [50] S. Wilkinson et al. “Preliminary findings from a multi-robot system for large-scale extra-planetary additive construction”. In: Sept. 2016.
- [51] P. Jiggins et al. “The magnitude and effects of extreme solar particle events”. In: *Journal of Space Weather and Space Climate* 4 (2014), A20. DOI: [10.1051/swsc/2014017](https://doi.org/10.1051/swsc/2014017).
- [52] T. C. Slaba and K. Whitman. “The Badwar-O’Neill 2020 GCR Model”. In: *Space Weather* 18.6 (2020). DOI: [10.1029/2020sw002456](https://doi.org/10.1029/2020sw002456).
- [53] Changran Geng et al. “A Monte Carlo-based radiation safety assessment for astronauts in an environment with confined magnetic field shielding”. In: *Journal of Radiological Protection* 35.4 (2015), pp. 777–788. DOI: [10.1088/0952-4746/35/4/777](https://doi.org/10.1088/0952-4746/35/4/777).
- [54] R.F. Wimmer-Schweingruber et al. “The Lunar Lander Neutron and Dosimetry (LND) Experiment on Chang’E 4”. In: *Space Science Reviews* 216.6 (2020). DOI: [10.1007/s11214-020-00725-3](https://doi.org/10.1007/s11214-020-00725-3).
- [55] NASA, JPL, and Johnson Space Center. *Cosmic Ray Environment*. URL: <https://phys.org/news/2016-11-bad-mars.html>.
- [56] M.L. Litvak et al. “Mars neutron radiation environment from HEND/Odyssey and DAN/MSL observations”. In: *Planetary and Space Science* 184 (2020). DOI: [10.1016/j.pss.2020.104866](https://doi.org/10.1016/j.pss.2020.104866).
- [57] K.M. Cannon et al. “Mars global simulant MGS-1: A Rocknest-based open standard for basaltic martian regolith simulants”. In: *Icarus* 317 (2019), pp. 470–478. DOI: [10.1016/j.icarus.2018.08.019](https://doi.org/10.1016/j.icarus.2018.08.019).
- [58] University of Central Florida. *MGS-1 prototype*. URL: https://sciences.ucf.edu/class/simulant_marsglobal/.
- [59] NASA, JPL-Caltech, and MSSS. *Scoop Marks in the Sand at ‘Rocknest’*. 2012. URL: <https://mars.nasa.gov/resources/4907/scoop-marks-in-the-sand-at-rocknest/>.
- [60] C.N. Achilles et al. “Mineralogy of an active eolian sediment from the Namib dune, Gale crater, Mars”. In: *Journal of Geophysical Research: Planets* 122.11 (2017), pp. 2344–2361. DOI: [10.1002/2017je005262](https://doi.org/10.1002/2017je005262).
- [61] David Karl et al. “Sintering of ceramics for clay in situ resource utilization on Mars”. In: *Open Ceramics* 3 (2020), p. 100008. DOI: [10.1016/j.oceram.2020.100008](https://doi.org/10.1016/j.oceram.2020.100008).
- [62] F. Ceccanti et al. “3D printing technology for a moon outpost exploiting lunar soil”. In: International Astronautical Federation. 2010, pp. 8812–8820.
- [63] Cheng Zhou et al. “Design and automated assembly of Planetary LEGO Brick for lunar in-situ construction”. In: *Automation in Construction* 118 (2020), p. 103282. DOI: [10.1016/j.autcon.2020.103282](https://doi.org/10.1016/j.autcon.2020.103282).

- [64] GRANTA EduPack. 2020. URL: <https://www.ansys.com/products/materials/granta-edupack>.
- [65] M. Naito et al. “Investigation of shielding material properties for effective space radiation protection”. In: *Life Sciences in Space Research* 26 (2020), pp. 69–76. DOI: [10.1016/j.lssr.2020.05.001](https://doi.org/10.1016/j.lssr.2020.05.001).
- [66] M. Vuolo, G. Baiocco, et al. “Exploring innovative radiation shielding approaches in space: A material and design study for a wearable radiation protection spacesuit”. In: *Life Sciences in Space Research* 15 (2017), pp. 69–78. DOI: [10.1016/j.lssr.2017.08.003](https://doi.org/10.1016/j.lssr.2017.08.003).
- [67] K. Hellström, A. Diószegi, and L. Diaconu. “A Broad Literature Review of Density Measurements of Liquid Cast Iron”. In: *Metals* 7.5 (2017), p. 165. DOI: [10.3390/met7050165](https://doi.org/10.3390/met7050165).
- [68] C. Zeitlin, S. Guetersloh, L. Heilbronn, and J. Miller. “Measurements of materials shielding properties with 1GeV/nuc ^{56}Fe ”. In: *Nuclear Instruments and Methods in Physics Research Section B: Beam Interactions with Materials and Atoms* 252.2 (2006), pp. 308–318. DOI: [10.1016/j.nimb.2006.08.011](https://doi.org/10.1016/j.nimb.2006.08.011).
- [69] Brookhaven National Laboratory. *NSRL User Guide*. URL: <https://www.bnl.gov/nsrl/userguide/bragg-curves-and-peaks.php>.
- [70] ESA. *ASTRONAUT APPLICANT HANDBOOK*. Tech. rep. 2021. URL: https://esamultimedia.esa.int/docs/careers/ESA_Astrosel_Handbook.pdf.
- [71] NASA. *Astronaut Selection and Training*. Tech. rep. 2011. URL: https://www.nasa.gov/centers/johnson/pdf/606877main_FS-2011-11-057-JSC-astro_trng.pdf.
- [72] NRC. *Radiation Basics*. Mar. 2020. URL: <https://www.nrc.gov/about-nrc/radiation/health-effects/radiation-basics.html>.

4

Additive Manufacturing of an MGS-1/Polymer Composite

4.1. Rationale for Additive Manufacturing of the Composite

Additive manufacturing, often called 3D printing, is a developing prototyping, manufacturing and construction technology and an attractive option for space applications, such as space exploration and potential extraterrestrial habitation. It opens up a wide range of interesting and novel approaches to construct habitats on Mars because it can create complex structures (*Isachenkov et al., 2021*) in relatively short times. The process requires minimal preprocessing and makes efficient use of local materials such as Martian regolith, which reduces the transport of construction materials from Earth and thus drastically reducing the launch costs and reliance on Earth supplies (*Naser, 2019*). Additive manufacturing for space applications is already heavily researched, e.g. presented in *Cesaretti et al., 2014*, *Kalapodis, Kampas, and Ktenidou, 2020*, *Leach, 2014*, and Figure 4.1 shows illustrations of 3D printing a Martian habitat and collecting Martian regolith.



Figure 4.1: (a) 3D printing of a Martian habitat (*AI SpaceFactory, 2019*) and (b) collecting Martian regolith (*NASA, 2020*).

The rationale of 3D printing an MGS-1/polymer composite is based on the finding from Chapter 3, that a polymer may still be useful as a binder to produce regolith blocks, and to enhance the structural integrity of the habitat shield. Therefore, the feasibility of creating a composite filament consisting of MGS-1 and a polymer is explored. A study that investigates the structural integrity of the composite is considered out of scope and only the density will be assessed due to its significant and positive effect on the dose reduction, as concluded in Chapter 3.

4.2. Preparation

The concept of making filament and 3D printing is briefly elaborated here. First, the *NEXT 1.0 - advanced* filament maker from *3devo*, shown in Figure 4.2a, is used to make filament. Filament is the

wounded material, usually a thermoplastic polymer, that is fed to the 3D printer. Materials are added into the hopper, labelled in Figure 4.2a, and should be in the form of pellets or granulates. Then, the extruder screw in the machine moves the material to the nozzle while it melts. At the nozzle, the premature filament is extruded and passes through the filament sensor and puller wheel. This sensor measures the filament diameter and the user must ensure that the correct filament diameter required to 3D print is achieved. The puller wheel makes sure that filament leaves the nozzle evenly. The filament spool automatically winds the filament once the correct diameter is reached, resulting in a suitable filament for 3D printing. Figure 4.2b shows an example of an FDM (Fused Deposition Modelling) printer. This type of printer works by inserting a filament in the extruder head, in which the material melts and is extruded through the nozzle. The nozzle moves in such a way that the intended object is printed layer by layer until finished.

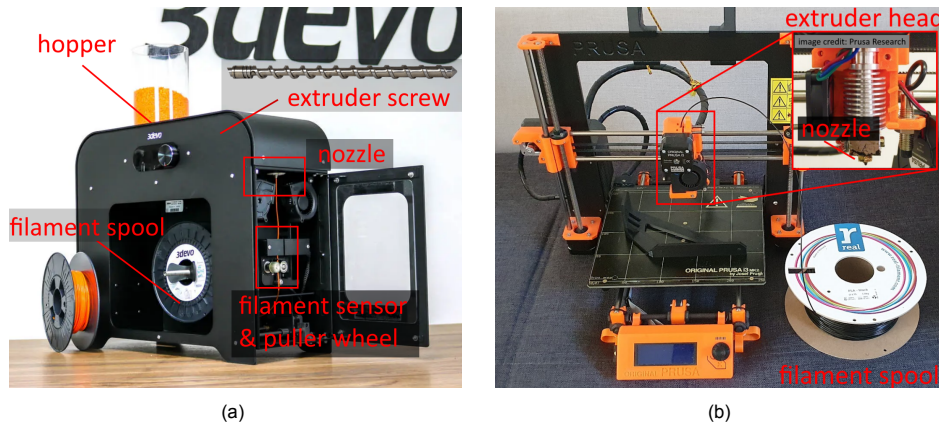


Figure 4.2: (a) The *NEXT 1.0 - advanced* filament maker (3devo, 2021) and (b) a Prusa MK2 FDM printer.

To make filament from MGS-1 and a polymer, the MGS-1 simulant must be sieved first. This is to prevent potential accumulation of particles that clog the nozzle when particles have large diameters with respect to the nozzle diameter. The used 3D printer has a nozzle diameter of 0.4 mm, while the MGS-1 particle size range is 0.04 μm - 600 μm , as retrieved from the fact sheet in Appendix A. This justifies the sieving as the large MGS-1 particles can damage the extrusion nozzle of the FDM printer. The nozzle diameter of the filament maker is 4 mm, and is sufficiently large for any MGS-1 particle. Two sieves with a mesh size of 0.150 mm and 0.056 mm are used, resulting in three batches; one with particle diameters smaller than 0.056 mm, one between 0.056 and 0.150 mm, and one larger than 0.150 mm. The sieving machine and three MGS-1 batches are shown Figure 4.3.

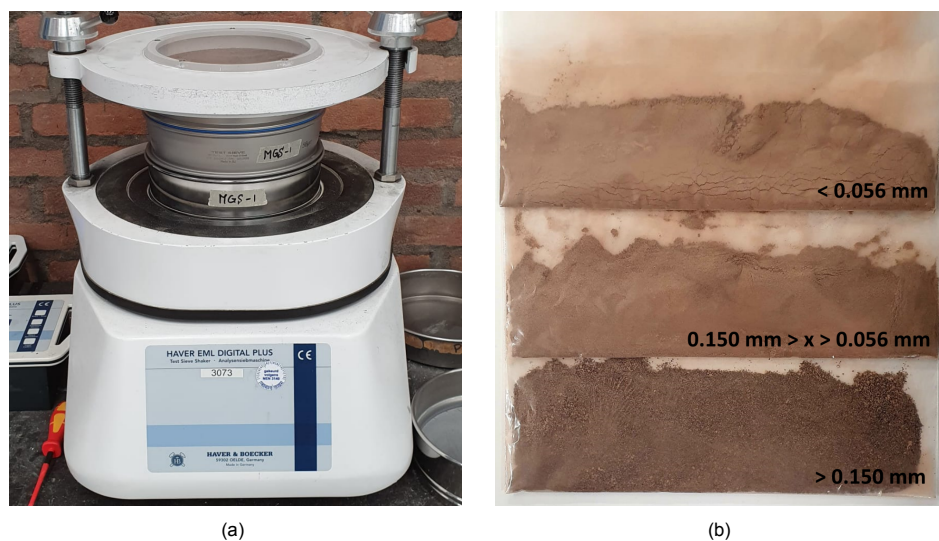


Figure 4.3: (a) The *Haver EML Digital Plus* sieve shaker and (b) the three MGS-1 batches after sieving.

4.3. Filament Making and 3D Printing

Once sieved, the filament is made using the filament maker from *3devo*. This machine allows the production of a combination of multiple materials into a single filament. In this case, the used materials are PLA pellets and weight fractions of 5wt%, 10wt% and 20wt% of MGS-1 particles, both shown in Figure 4.4. The batch of particles with a diameter between 0.056 mm and 0.150 mm was used because very fine particles may also lead to brittle filament as reported in *Spaceship EAC: 3D printing with lunar dust 2021*. PLA (Polylactic Acid) was selected as polymer because it is the most commonly and conventionally used 3D printing filament. Small weight fractions of MGS-1 were added with the intent of reducing the chance of producing a brittle filament that consequently cannot be used. Larger weight fractions may result in a more brittle filament as well, because MGS-1 particles cannot bind together when 3D printed. Therefore, a polymer is required that binds the MGS-1 particles when melted at a certain temperature. First, a weight fraction of PLA and MGS-1 of 95wt% and 5wt%, respectively, was used as a first attempt to make filament. However, the MGS-1 particles sank to the extrusion screw much faster than the PLA pellets, leading to higher concentrations of MGS-1. For this reason, all original PLA and MGS-1 batches were combined and added in small amounts to the hopper of the filament maker such that the materials would mix to a certain extent. Despite this effect, the composite filament was successfully produced. However, an homogeneous concentration of the materials throughout the filament could not be achieved and this resulted in local concentration variations. Because all PLA and MGS-1 were combined, the average weight fraction concentration of the filament was $\sim 88.3\text{wt}\%$ and $\sim 11.7\text{wt}\%$ for PLA and MGS-1, respectively.



Figure 4.4: (a) Sieved MGS-1 particles and PLA pellets, and (b) the produced MGS-1/PLA composite filament.

The difference in local concentration of the filament could also be observed by the color. Filament parts with darker colors corresponded to higher MGS-1 concentrations due to the transparent PLA pellets, as can be seen in Figure 4.5a. Some filament parts had such high MGS-1 concentrations that they broke immediately when handled and as a result could no longer be used for 3D printing. Different strands of the same filament with locally different concentrations, shown in Figure 4.5b, were used to measure the density, which is done according to Archimedes' principle. The measured densities are given in Table 4.1.



Figure 4.5: (a) Different concentrations of MGS-1 and PLA as derived by the color, and (b) filament strands with differing concentrations to measure the density, ranging from low (S1) to high (S4) MGS-1 weight fractions.

Table 4.1: Measured densities, based on Archimedes' principle, of the MGS-1/PLA filament strands.

Strand	Density	Concentration
S1	1.242 g/cm ³	100% PLA
S2	1.363 g/cm ³	lowest MGS-1 concentration
S3	1.392 g/cm ³	MGS-1 concentration between S2 and S4
S4	1.523 g/cm ³	highest MGS-1 concentration

Table 4.1 shows that with increasing weight fractions of MGS-1, the density also increases. The lowest density is observed for strand S1, which corresponds to pure PLA, and while the density of strand S4 is considerably larger, it is very fragile and breaks easily. This is a trade-off between parameters, where on the one hand increased weight fractions of MGS-1 lead to higher densities which relate to a increased dose reduction. On the other hand, increased MGS-1 weight fractions also decrease the structural integrity of the composite. Further research is required to study and develop methods where the composite density can be increased, while maintaining its structural integrity. Still, printing with the MGS-1/PLA filament at certain concentrations was successful. This demonstrates that producing the composite filament and printing with it is feasible. Some examples of 3D printed samples from the filament is shown in Figure 4.6.



Figure 4.6: Successfully 3D printed samples using the MGS-1/PLA filament.

4.4. Effect on Filament Density of Different Print Settings for Polymers

Additionally, the density effect due to different print settings was analyzed. Existing polymer filaments that were used for this were PLA, PETG (Polyethylene Terephthalate, Glycol modified) and LCP (Liquid Crystal Polymer). PLA and PETG were chosen because these are the most common and conventional 3D printing filaments, while LCP is a high-performance polymer provided by the Shaping Matter Lab research group of the aerospace faculty.

From these filaments, cubes of 2 x 2 x 2 cm were printed, as shown in Figure 4.7a, where two print settings were varied. These assessed print settings were *layer height* and *material flow*. The *layer height* defines the height of each layer that is printed and *material flow* specifies the amount of material that leaves the nozzle, usually expressed in mm and as a percentage of mm³/s, respectively. One of these settings was varied, while the other was kept constant, to inspect the effect on the sample density. The density of a small strand of the filament was also measured, such that it could be compared to the densities of the 3D printed samples. Furthermore, different filament brands were used for the investigation of each of the two print settings to compare the variations in densities between different brands of PETG and PLA. The setup used for measuring the density is shown in Figure 4.7b, while Table 4.2 shows the measured densities of the PETG and PLA samples based on the varying print settings.

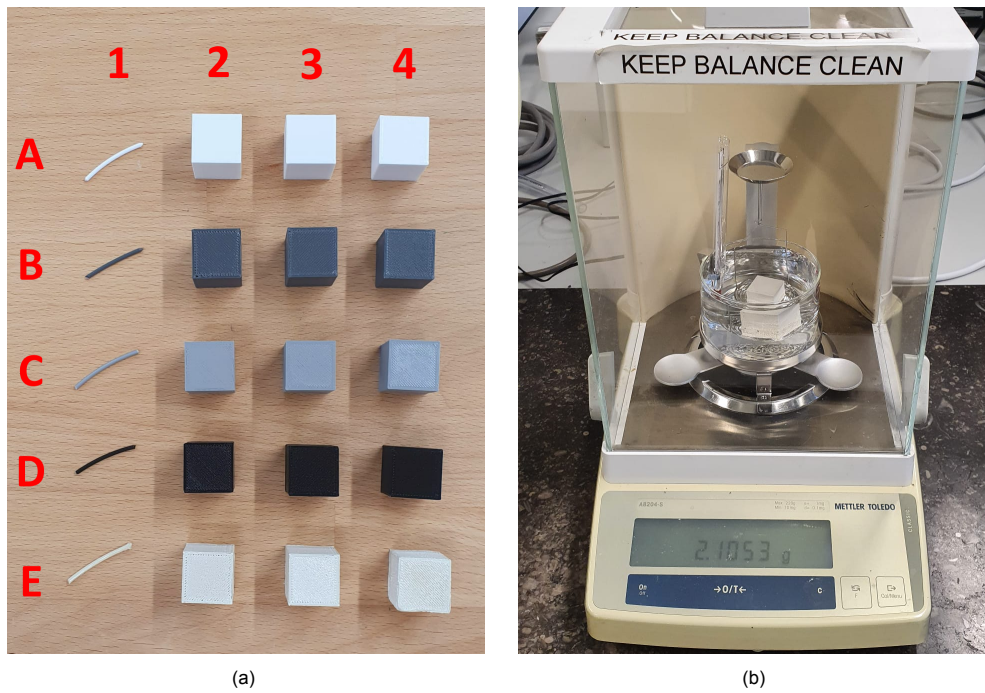


Figure 4.7: (a) All 3D printed sample cubes and filament strands with labels in accordance with Tables 4.2 and 4.3. Samples A1-4 and B1-4 are PETG, samples C1-4 and D1-4 are PLA, and sample E1-4 is LCP. (b) The Mettler Toledo AB204-S density meter using Archimedes' principle for measuring the cube samples.

Table 4.2: Measured density values of the PETG and PLA 3D printed samples. The density is expressed in g/cm³.

PETG							
Sample	Density	Layer height	Material flow	Sample	Density	Layer height	Material flow
1A	1.304	<i>filament strand</i>		1B	1.284	<i>filament strand</i>	
2A	1.122	0.1 mm	100%	2B	1.097	0.2 mm	100%
3A	1.104	0.2 mm	100%	3B	0.986	0.2 mm	90%
4A	1.098	0.3 mm	100%	4B	0.778	0.2 mm	80%
Brand: Extrudr PETG - white				Brand: 3DJAKE PETG - dark grey			
PLA							
Sample	Density	Layer height	Material flow	Sample	Density	Layer height	Material flow
1C	1.263	<i>filament strand</i>		1D	1.264	<i>filament strand</i>	
2C	1.141	0.1 mm	100%	2D	1.095	0.2 mm	100%
3C	1.140	0.2 mm	100%	3D	0.894	0.2 mm	90%
4C	1.148	0.3 mm	100%	4D	0.811	0.2 mm	80%
Brand: Innofil3D PLA - grey				Brand: real PLA - black			

Table 4.2 shows that all densities of the printed samples are reasonably lower than the filament strands. This is because 3D printing the samples creates small cavities of air. These cavities usually appear near the inner edges and corners, as shown in Figure 4.8a. The measurements indicate that the layer height has a minimal effect on the density, while the density is more affected by the material flow. When only printing at 80% or 90% of the material flow, less material per second is extruded and created larger cavities in the corner and sides, as well as between the layers of the infill pattern as shown in the close-up of Figure 4.8a. Furthermore, since the sample were submerged in distilled water for the density

measurements, tiny air pockets may have attached to the sample. This was countered by shaking the submerged sample in the distilled water. Although tiny air pockets could still have been present, it should not have had a significant impact on the final density of the sample. Because the layer height did not affect the resulting density as much as changing the flow, only the flow was varied for two different layer heights in the case of LCP, also because it is an expensive filament.

The measured densities of the LCP samples are shown in Table 4.3. It can be seen that the density of the LCP filament strand is close to the reported density of 1.4 g/cm^3 by *Celanese, 2014*. At the default material flow speed of 100%, the density value of sample 2E was closer to the measured density of the LCP filament strand compared to PETG and PLA. However, sample 2E had over-extruded as can be seen in Figure 4.8b. This is also observed to a lesser extent for samples 3E and 2E, but both samples also had lower densities. In the context of achieving the highest possible density, over-extrusion could be considered because the radiation shield surrounding the habitat can be created with a rather rough structure such as shown with sample 2E. When comparing the densities of the polymers with the bulk density of MGS-1, i.e. 1.29 g/cm^3 , they do not differ significantly. The earlier mentioned upper limit density of 2.49 g/cm^3 as reported by Karl et al., 2020, is attained by means of sintering the 3D printed regolith simulant. High density values that are attained by sintering, cannot be achieved when only 3D printing is considered. It may be that 3D printing a thicker shield with a lower density is a less demanding process than sintering a thinner shield with a higher density. However, more research is required to evaluate this trade-off between design parameters.

Relating the aforementioned findings to the MGS-1/PLA composite filament also means that the 3D printed samples will have lower densities than the filament strand. Over-extruding this composite filament should also lead to a higher density but should be examined more in future work.

Table 4.3: Measured density values of the LCP 3D printed samples. The density is expressed in g/cm^3 .

LCP			
Sample	Density	Layer height	Material flow
1E	1.408	<i>filament strand</i>	
2E	1.349	0.2 mm	100%
3E	1.279	0.2 mm	90%
4E	1.153	0.2 mm	80%
Brand: Vectra A950			

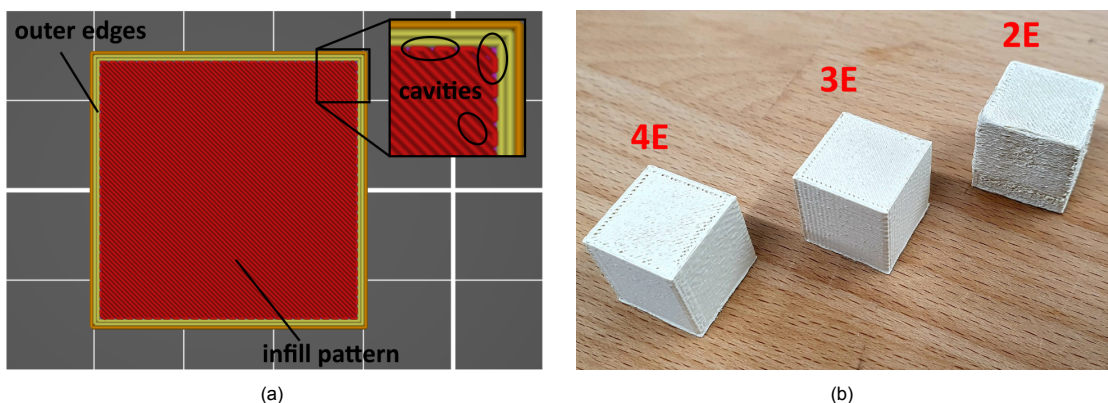


Figure 4.8: (a) Top view of the cubic samples with indicated print features and (b) 3D printed LCP samples with labels in accordance with Table 4.3.

5

Conclusions and Recommendations

5.1. Conclusions

In addition to the conclusions at the end of Chapter 3, this chapter also draws conclusions by answering the research questions listed in Chapter 1. First, the sub-questions are answered and based on these, the main research question is answered subsequently. Note that some of the conclusions from Chapter 3 could be repeated to some extent based on how the research questions are answered.

Q1. How should the radiation shielding capability be assessed and verified?

The radiation shielding capability is assessed by means of dose reduction. This is done by measuring the absorbed dose in the situation where a shield is present and where such a shield is absent. The absorbed dose is used instead of the equivalent dose or effective dose because it is a directly measurable physical quantity, while the two others are not. The equivalent dose and effective dose include radiation and tissue weighting factors that are published by the International Commission on Radiological Protection (ICRP). These values are periodically updated in accordance with advances in understanding the effects of space radiation on the human body. Evidently, the most recent ICRP weight factors should be considered. The measured absorbed dose is as it stands and, hence, is not subject to change. However, it should be noted that when these results are compared with the biological effects, the conversion to equivalent dose or effective dose has to be carried out. Verification of the FLUKA particle transport code is done in Chapter 2.2 by reproducing documented plots of radiation through a shield with given thickness and material density, and then consequently comparing them to these documented plots. Furthermore, the executed sensitivity analysis by varying density values and different shield materials also showed a logical progression of the dose reduction with increasing shield thickness. Finally, a full verification of the results could not be performed due to the lack of reference material for this particular topic, i.e. dose reduction of MGS-1 shields and an MGS-1 habitat structure.

Q2. How is space radiation characterized and how should it be applied to the use case?

Space radiation originates from two sources, GCR and SPE. The averaged GCR during a solar minimum is chosen with respect to historical SPE because its energies are most often much higher. This is also inferred from the OLTARIS output files, where the GCR upper limit is 50 GeV as opposed to 2.5 GeV for SPE. Furthermore, the particle type spectrum of GCR also includes the critical heavy ions. Because the habitat is located on the Martian surface, secondary radiation neutrons arising from primary radiation interactions with the Martian atmosphere and surface should be included as well. The particle type and energy spectra are retrieved from the online OLTARIS tool from which the neutron contribution to the total flux is calculated as the largest at ~81.10%. For the simulations consisting of a simple shield, the averaged GCR is applied by means of monochromatic beams for selected particle types with one fixed energy. These are neutrons, protons, helium, carbon, oxygen, silicon and iron. The fixed energy for neutrons is 740 MeV and 1 GeV for the other particles. These high energy limits are chosen as a trade-off

between the representation of the majority of all particles as well as the required computational power and time needed for the large number of simulations. In the context of a non-complex Martian habitat for a simplified GCR case, the entire energy spectrum of the selected particle types is applied. The GCR case is simplified in such a way that the normally isotropic distribution is concentrated into nine beams that are directed towards the center of the habitat, where the first phantom is located. This simplification was necessary because a FLUKA compatible script needs to be written that takes into account the energy spectrum of all particles combined and randomly distributes them around the habitat with different beam directions. This is a major task and could not be carried out due to time constraints. This simplification gives a good initial understanding but becomes a limitation in continued work.

Q3. How should the polymer selection process be carried out in terms of radiation shielding capabilities?

First, the material index from *Vuolo et al., 2017* is determined for the chosen polymers, MGS-1 and reference materials. Good agreement was found between all materials according to the material index when the dose reductions from FLUKA were plotted with respect to area density (g/cm^2). With respect to shield thickness (cm), the materials with highest density had the best dose reductions, meaning that density plays a significant role in achieving higher dose reductions. The bulk density of $1.29 \text{ g}/\text{cm}^3$ of MGS-1 is well within the density range of all polymers. For thick shields such as 250 cm, 300 cm and 400 cm, it was found that the influence of adding a polymer as middle or inner layer did not result in beneficial dose reduction gains. In this regard, a higher density MGS-1 shield is more favourable than the inclusion of polymers. As a result, the polymer selection process did not have to be carried out, and a homogeneous MGS-1 shield was used hereafter for the subsequent simulations.

Having answered the supporting sub-questions, the main research question can be addressed. This is related to the research objective defined in Chapter 1:

« to assess the radiation shielding properties of Martian regolith simulant MGS-1 and polymers by analyzing the dose reduction in terms of absorbed dose of the particle spectrum on the Martian surface during a galactic cosmic ray or solar particle event »

The main research question is:

What is the most feasible regolith simulant and polymer composite that results in maximal dose reduction of space radiation?

Initially, the purpose was to use a composite consisting of MGS-1 and a polymer as a radiation shield. However, the influence of a polymer for radiation shielding did not have a significant gain on the dose reduction with respect to a thick shield consisting of only MGS-1. The radiation shielding performance by MGS-1 was found to be consistent with the selected polymers and is primarily determined by its density. For the Martian habitat, a shield thickness of 250 cm is chosen based on references and the limitations posed by the required computational power. Consequently, in terms of radiation shielding, it is not necessary to transport the polymer to Mars or to produce it on site, while Martian regolith is readily available in vast amounts. Assessing the maximal dose reduction of space radiation proved to be a complex topic and an intrinsic task due to many variables that influence each other in different ways. Hence, the ALARA principle should be considered. A dose reduction *As Low As Reasonably Achievable* in this context means that the preparations and a first assessment of the dose reduction provide a fundamental insight and serves as a point of reference for further iterations and improvements in the radiation shield and habitat design. However, the work performed under this thesis cannot be fully related to the ALARA principle. This is because the absorbed dose is the directly measured type of radiation, while the equivalent dose and effective dose with their associated weighting factors are used to relate it to the biological effects on the human body. Only then can the dose reduction be fully compared and related to the ALARA principle, as well as the dose limits set by national space agencies. This work carried out the first strategy and steps that are essential for the continuation of this topic.

The two additional research questions concerning 3D printing of the polymer and MGS-1 composite are answered:

Q4. How is the polymer chosen to be used as the filament for 3D printing?

The production of the MGS-1 and polymer composite filament and consequently 3D printing, was successful and proven to be feasible. The polymer PLA was chosen for this composite as it is the most conventional and referenced 3D printing filament, as well as for its ease of printing. Furthermore, LCP, PETG and PLA samples were 3D printed from which the densities were determined. Similar to PLA, PETG is convenient to use. LCP was chosen because it is a high-performance polymer, and was made available by the Shaping Matter Lab research group of the aerospace faculty of the Delft University of Technology. The use of other polymers and the assessment of other material properties, based on their performance in the Martian environment, are proposed in the recommendations hereafter.

Q5. Which material properties of the 3D print are relevant and how are these evaluated?

For this work, the most important material property is the density because of its effect on the dose reduction. It was previously concluded that a higher density relates to a significant improvement of the dose reduction. The densities of all the samples were measured using a density meter that applies Archimedes' principle. The density of filament strands with various concentrations was determined using this setup. It was found that higher concentrations of MGS-1 resulted in higher densities but also increased the brittleness and fragility of the filament. However, a homogeneous concentration could not be attained throughout the entire filament due to the inconsistent mixing of PLA pellets and MGS-1 particles in the filament maker. The MGS-1 particles sank faster to the extrusion screw of the filament maker than the PLA pellets. Moreover, sample cubes were printed using three polymers with varied *layer height* and *material flow*. Generally, all 3D printed samples had lower densities than the density of the filament itself. Changing the *layer height* did not result in a significant density difference but changing the *material flow* did cause considerable changes. Furthermore, it is recommended to over-extrude while printing such that possible air cavities are avoided in order to increase the density. Lastly, higher densities could also be obtained with other (additive) manufacturing techniques, such as sintering, and could be even more convenient to use than extrusion printing. However, this conclusion is based on small-scale 3D printing and scaling up the extrusion printing process could result in a more advantageous process again. Therefore, additional research is required.

5.2. Recommendations

For the continuation of this work, the following recommendations are made and elaborated per topic. These recommendations may lead to the merging of topics between the space engineering and aerospace materials master tracks, enabling further cooperation between aerospace departments of TU Delft. Also important to mention is that each of these topics will greatly benefit from new and existing data of radiation measurements performed on Mars. The recommendations are:

Reproducing a representative GCR event

- A representative and accurate GCR event was not simulated due to practical complications and time constraints. To truly reproduce an GCR event, the incoming particle beams should be distributed randomly around the habitat geometry in three dimensions as well as their directions. In other words, an isotropic distribution around the habitat should be reproduced. In practical terms using the FLUKA software, this means that a dedicated script (called a source routine in FLUKA) should be written which also includes the use of multiple particle types as well as their energy spectra sampling from the OLTARIS output. It is not known whether the implementation of the [energy spectra routine](#), that is available to use, can be combined with such a user-defined script. If not, the energy spectra routine has to be adapted and included in this user-defined script.
- If more computational power is available, for example by means of servers, the initial simulations can be run again, but with significantly more primaries and thus reduced errors. Now, each simulation was run on the author's laptop which involves certain limitation in computational power.

Moreover, the inclusion of the energy spectra instead of monochromatic beams is a recommendation as this possibility was only discovered at a later stage.

- An interesting finding by *Heilbronn et al., 2015* can also be further explored. It has been reported that a full GCR particle type spectrum was replaced by a simplified case with similar results. Two cases have been assessed: the first case included protons, helium and oxygen with a scaling factor, whereas for the second case only protons and helium with a scaling factor were used. Using a simplified case could also save computation power and time. For the Martian environment, neutrons will have to be included as well.

Mars habitat design, the location on Mars and the Martian environment

- With a representative GCR event in FLUKA, the Martian habitat design can be further iterated by means of shield thicknesses, different densities and other materials.
- Instead of a general Mars location, several suitable Mars locations based on references at their corresponding altitudes can be examined. For example, the OLTARIS tool allows the user to input a specific location based on coordinates as well as the altitude. This way, further improvements can be made in the context of the intended human presence on Mars ultimately.
- Another option is to investigate the feasibility of a (partially) underground habitat, or at geological features such as next to a cliff or in a valley. These geological features should also influence the radiation environment, but comprehensive research is currently lacking.
- Finally, the influence of the Martian environment can be studied, such as the surface temperatures that can reach cryogenic values. The Martian seasonal changes and dust storms also have a critical influence on the radiation environment (both for primary and secondary radiation) that should be considered eventually.

Conversion from absorbed dose to equivalent dose and effective dose

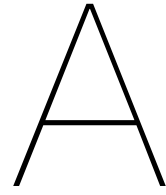
- Once an accurate GCR event has been reproduced and implemented in FLUKA, the results can be linked to the biological effects for humans by taking into account the most recent ICRP radiation and tissue weighting factors. This can either be done after the FLUKA simulations for absorbed dose or using the built-in equivalent and effective scoring options.
- Once the equivalent dose or effective dose is assessed, its results could be used to relate them with the daily dose limits, career dose limits, etc., set by national space agencies. This way, it can be reviewed how realisable and achievable these limits are with respect to habitation on Mars, and how viable the idea of human colonization is at this moment because the radiation dose limits are currently based on low-Earth orbits .
- The OLTARIS tool also has several options for the equivalent and effective doses. This can also be used to compare it with the FLUKA results.

Benchmarking different particle transport codes and space environment models

- Considering that all simulations in this work are done in FLUKA and have used the OLTARIS environment model, it could be interesting to benchmark them with other alternatives. For particle transport codes, the same simulations can be performed in GEANT4, for example. Similarly, SPENVIS is another space environment model that is available for use. Because the dose reductions are determined for GCR during solar minima, other GCR models can also be assessed. The Badhwar-O'Neill 2020 GCR model (BON2020) is used for this work, while other models are for example BON2014, Matthia 2013, SINP 2016 in OLTARIS and ISO 15390, Nymmik and CREME96 in SPENVIS.

Additive manufacturing

- Extensive research can be conducted in the field of additive manufacturing. First, the weight fraction of MGS-1 with respect to the polymer can be optimized, i.e. increasing the MGS-1 weight fractions as much as possible while still acquiring a 3D printable filament. Usually, high weight fractions of regolith (simulant) lead to brittle filament that cannot be used. Similar research using lunar regolith simulant is done by the Spaceship EAC (European Astronaut Center) team of ESA, see [Spaceship EAC: 3D printing with lunar dust 2021](#). Moreover, instead of using polymer pellets and MGS-1 granulates, both components can be implemented in granulate form. This could ensure a better and even mix between the components. Concerning filament making, at some point industrial filament makers could be used to create high-end, qualitative filaments instead of utilizing the 3devo filament maker.
- Other methods could also be explored to achieve high(er) density values of MGS-1 by means of a trade-off. This may involve investigating and experimenting with different (additive) manufacturing methods such as 3D printing and sintering, e.g. done by *Karl et al., 2020*. Furthermore, any manufacturing process considered for Martian habitats need to be scaled up which has implications on this trade-off.
- Possibilities to perform physical radiation tests can be examined as well. Potential locations could be the GSI Helmholtz Centre for Heavy Ion Research in Germany or at CHARM, which is the CERN radiation test facility in Switzerland. It is important to mention that this needs to be considered well in advance in order to carry out the necessary preparations.
- Also the influence of Martian cryogenic temperatures on polymers and MGS-1 can be investigated. Regarding Martian habitats, polymers with good performance at low temperatures in terms of radiation shielding and structural strength could make them an interesting option to consider again. In particular, the high-performance LCP polymer is an interesting option because of its promising properties that seem to make them suitable in the Martian environment. The *Shaping Matter Lab* interdisciplinary research group of the aerospace faculty is working with this polymer.



MGS-1 Fact Sheet

The version of the fact sheet used in this work is from January 2021. However, it has been updated in November 2021 with a slightly different bulk chemistry. These updated bulk chemistry values are not used because they were not accessible at the time of running the simulations.



Simulant Name: MGS-1 Mars Global Simulant

Simulant Type: General purpose

Reference Material: Rocknest soil

Uncompressed Bulk Density: 1.29 g/cm³

Mean Particle Size: 90 μm

Median Particle Size: 60 μm

Particle Size Range: >0.04 μm – 600 μm

Publication: Cannon et al. 2019, Icarus 317, 470-478



Mineralogy

As mixed.

Component	Wt.%
Anorthosite	27.1
Glass-rich basalt	22.9
Pyroxene	20.3
Olivine	13.7
Mg- sulfate	4.0
Ferrihydrite	3.5
Hydrated silica	3.0
Magnetite	1.9
Anhydrite	1.7
Fe-carbonate	1.4
Hematite	0.5

Safety

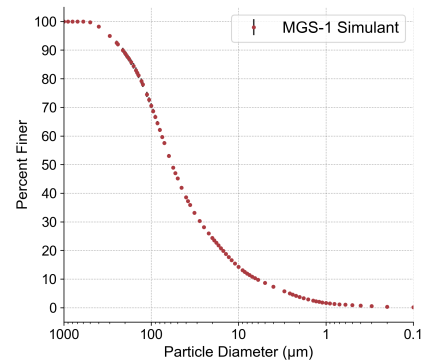
See SDS for details. Primary hazard is dust inhalation; wear a respirator in dusty conditions.

Bulk Chemistry

Measured by XRF.

Oxide	Wt.%
SiO ₂	45.2
TiO ₂	0.4
Al ₂ O ₃	14.9
Cr ₂ O ₃	0.2
Fe ₂ O ₃	18.7
NiO	0.2
MnO	0.1
MgO	7.6
CaO	10
K ₂ O	0.6
P ₂ O ₅	0.9
SO ₃	0.9
Cl	0.4
SrO	0.1
Total	100.0

Particle Size Distribution



FTIR Spectrum

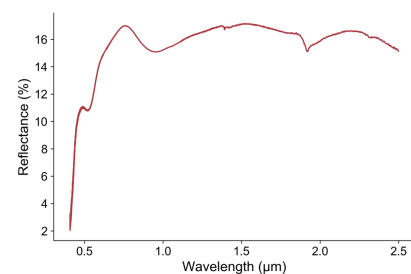


Photo credit Matthew Villegas. FTIR spectrum courtesy of Katerina Slavicinska, Bennett Lab, UCF.

Figure A.1: Fact sheet (January 2021) of Martian regolith simulant MGS-1 (ExolithLab, 2020).

B

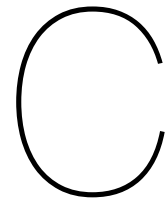
Dose Reduction Tables for Varying Number of Primaries and Seeds

Table B.1: Effect of the number of primaries and different seeds for 500 MeV neutron beams on the dose reduction of an MGS-1 shield with 1.29 g/cm³ density and a thickness range of 20-200 cm. 5k, 10k and 50k represents 5000, 10000 and 50000 primaries, respectively, while s1-5 denotes different randomized seeds. D_{norm} is the normalized dose, $E_{D_{norm}}$ is the error of the normalized dose and δD is the dose reduction.

		Shield thickness														
Particle	Primary & seeds	20 cm			40 cm			60 cm			80 cm			100 cm		
		D_{norm}	$E_{D_{norm}}$	δD	D_{norm}	$E_{D_{norm}}$	δD	D_{norm}	$E_{D_{norm}}$	δD	D_{norm}	$E_{D_{norm}}$	δD	D_{norm}	$E_{D_{norm}}$	δD
neutron	5k s1	1.5388	1.27%	-53.88%	1.7312	0.79%	-73.12%	1.7183	0.79%	-71.83%	1.5839	1.06%	-58.39%	1.4124	0.96%	-41.24%
	5k s2	1.5849	2.79%	-58.49%	1.7038	2.79%	-70.38%	1.7264	2.94%	-72.64%	1.6059	2.82%	-60.59%	1.4285	2.83%	-42.85%
	5k s3	1.5183	1.75%	-51.83%	1.6876	1.69%	-68.76%	1.6887	1.88%	-68.87%	1.5329	1.72%	-53.29%	1.3922	1.65%	-39.22%
	5k s4	1.5612	1.89%	-56.12%	1.7007	1.70%	-70.07%	1.6550	1.80%	-65.50%	1.5663	1.56%	-56.63%	1.4125	1.77%	-41.25%
	5k s5	1.6335	1.41%	-63.35%	1.7666	1.59%	-76.66%	1.7821	1.53%	-78.21%	1.6278	1.37%	-62.78%	1.4602	1.48%	-46.02%
	10k s1	1.5854	1.15%	-58.54%	1.7659	0.95%	-76.59%	1.7346	0.79%	-73.46%	1.6059	0.97%	-60.59%	1.4502	1.20%	-45.02%
	10k s2	1.6201	1.71%	-62.01%	1.7870	1.72%	-78.70%	1.7607	1.60%	-76.07%	1.6450	1.78%	-64.50%	1.4803	1.59%	-48.03%
	10k s3	1.5851	1.88%	-58.51%	1.7516	1.57%	-75.16%	1.7294	1.81%	-72.94%	1.6029	1.70%	-60.29%	1.4567	1.60%	-45.67%
	10k s4	1.6203	1.00%	-62.03%	1.7982	0.96%	-79.82%	1.7784	0.86%	-77.84%	1.6623	0.82%	-66.23%	1.4721	0.92%	-47.21%
	10k s5	1.5968	1.54%	-59.68%	1.7651	1.37%	-76.51%	1.7641	1.25%	-76.41%	1.6412	1.25%	-64.12%	1.4578	1.29%	-45.78%
	50k s1	1.5969	0.37%	-59.69%	1.7636	0.37%	-76.36%	1.7462	0.33%	-74.62%	1.6094	0.43%	-60.94%	1.4497	0.50%	-44.97%
	50k s2	1.6113	0.64%	-61.13%	1.7744	0.60%	-77.44%	1.7541	0.62%	-75.41%	1.6478	0.63%	-64.78%	1.4605	0.65%	-46.05%
	50k s3	1.6177	0.74%	-61.77%	1.7811	0.80%	-78.11%	1.7610	0.73%	-76.10%	1.6600	0.85%	-66.00%	1.4773	0.71%	-47.73%
	50k s4	1.6109	0.51%	-61.09%	1.7768	0.40%	-77.68%	1.7572	0.49%	-75.72%	1.6425	0.33%	-64.25%	1.4613	0.40%	-46.13%
	50k s5	1.5922	0.34%	-59.22%	1.7592	0.54%	-75.92%	1.7474	0.51%	-74.74%	1.6049	0.60%	-60.49%	1.4560	0.40%	-45.60%
Particle	Primary & seeds	120 cm			140 cm			160 cm			180 cm			200 cm		
		D_{norm}	$E_{D_{norm}}$	δD	D_{norm}	$E_{D_{norm}}$	δD	D_{norm}	$E_{D_{norm}}$	δD	D_{norm}	$E_{D_{norm}}$	δD	D_{norm}	$E_{D_{norm}}$	δD
neutron	5k s1	1.2588	1.08%	-25.88%	1.0661	1.82%	-6.61%	0.9317	2.06%	6.83%	0.7609	1.10%	23.91%	0.6419	1.40%	35.81%
	5k s2	1.2573	2.87%	-25.73%	1.0806	2.95%	-8.06%	0.9161	3.17%	8.39%	0.7960	2.77%	20.40%	0.6347	3.57%	36.53%
	5k s3	1.2264	2.09%	-22.64%	1.0293	2.12%	-2.93%	0.9116	1.86%	8.84%	0.7504	2.31%	24.96%	0.6403	2.64%	35.97%
	5k s4	1.2497	1.52%	-24.97%	1.0592	1.45%	-5.92%	0.9237	2.13%	7.63%	0.7794	2.21%	22.06%	0.6056	1.82%	39.44%
	5k s5	1.2623	1.60%	-26.23%	1.0792	1.48%	-7.92%	0.9301	1.14%	6.99%	0.7738	1.27%	22.62%	0.6664	1.59%	33.36%
	10k s1	1.2762	0.86%	-27.62%	1.0837	1.35%	-8.37%	0.9342	1.71%	6.58%	0.7752	1.89%	22.48%	0.6516	1.11%	34.84%
	10k s2	1.2874	1.55%	-28.74%	1.1102	1.66%	-11.02%	0.9291	1.55%	7.09%	0.8013	1.73%	19.87%	0.6519	2.17%	34.81%
	10k s3	1.2510	1.65%	-25.10%	1.0851	1.82%	-8.51%	0.9322	2.23%	6.78%	0.7806	1.83%	21.94%	0.6491	1.65%	35.09%
	10k s4	1.3150	1.27%	-31.50%	1.1146	1.02%	-11.46%	0.9342	1.29%	6.58%	0.7953	0.87%	20.47%	0.6662	1.48%	33.38%
	10k s5	1.2797	1.24%	-27.97%	1.1114	1.28%	-11.14%	0.9313	1.11%	6.87%	0.7794	1.12%	22.06%	0.6564	1.52%	34.36%
	50k s1	1.2669	0.47%	-26.69%	1.1000	0.48%	-10.00%	0.9355	0.60%	6.45%	0.7833	0.69%	21.67%	0.6538	0.41%	34.62%
	50k s2	1.2792	0.64%	-27.92%	1.1040	0.81%	-10.40%	0.9453	0.73%	5.47%	0.7903	0.67%	20.97%	0.6658	0.58%	33.42%
	50k s3	1.2883	0.80%	-28.83%	1.1125	0.77%	-11.25%	0.9564	1.00%	4.36%	0.8026	0.70%	19.74%	0.6710	0.80%	32.90%
	50k s4	1.2843	0.47%	-28.43%	1.1124	0.61%	-11.24%	0.9473	0.65%	5.27%	0.7959	0.51%	20.41%	0.6635	0.62%	33.65%
	50k s5	1.2719	0.35%	-27.19%	1.0959	0.30%	-9.59%	0.9313	0.42%	6.87%	0.7783	0.42%	22.17%	0.6499	0.45%	35.01%

Table B.2: Effect of the number of primaries and different seeds for 500 MeV neutron beams on the dose reduction of an MGS-1 shield with 1.29 g/cm³ density and a thickness range of 220-400 cm. 5k, 10k and 50k represents 5000, 10000 and 50000 primaries, respectively, while s1-5 denotes different randomized seeds. D_{norm} is the normalized dose, E_{Dnorm} is the error of the normalized dose and δD is the dose reduction.

		Shield thickness														
Particle	Primary & Seeds	220 cm			240 cm			260 cm			280 cm			300 cm		
		D _{norm}	E _{Dnorm}	δD												
neutron	5k s1	0.5268	2.13%	47.32%	0.4359	1.62%	56.41%	0.3598	2.19%	64.02%	0.2896	1.43%	71.04%	0.2392	2.58%	76.08%
	5k s2	0.5453	3.72%	45.47%	0.4688	3.70%	53.12%	0.3699	2.92%	63.01%	0.2965	3.66%	70.35%	0.2380	4.34%	76.20%
	5k s3	0.5310	2.69%	46.90%	0.4345	2.23%	56.55%	0.3621	2.66%	63.79%	0.2917	2.02%	70.83%	0.2388	3.82%	76.12%
	5k s4	0.5231	1.76%	47.69%	0.4248	2.73%	57.52%	0.3460	2.54%	65.40%	0.2927	1.90%	70.73%	0.2324	2.22%	76.76%
	5k s5	0.5559	2.57%	44.41%	0.4522	1.47%	54.78%	0.3637	2.07%	63.63%	0.3068	2.02%	69.32%	0.2584	3.38%	74.16%
	10k s1	0.5446	1.32%	45.54%	0.4455	1.29%	55.45%	0.3688	1.96%	63.12%	0.2941	1.24%	70.59%	0.2459	1.54%	75.41%
	10k s2	0.5353	1.65%	46.47%	0.4530	1.65%	54.70%	0.3826	2.47%	61.74%	0.3012	1.95%	69.88%	0.2580	2.03%	74.20%
	10k s3	0.5542	2.04%	44.58%	0.4512	2.25%	54.88%	0.3634	1.83%	63.66%	0.2995	1.84%	70.05%	0.2514	2.13%	74.86%
	10k s4	0.5544	1.40%	44.56%	0.4735	1.00%	52.65%	0.3854	1.43%	61.46%	0.3269	1.59%	67.31%	0.2475	1.31%	75.25%
	10k s5	0.5546	1.87%	44.54%	0.4598	1.91%	54.02%	0.3757	2.77%	62.43%	0.3010	1.66%	69.90%	0.2439	1.57%	75.61%
	50k s1	0.5510	0.86%	44.90%	0.4540	0.75%	54.60%	0.3692	0.46%	63.08%	0.3056	0.89%	69.44%	0.2446	0.42%	75.54%
	50k s2	0.5488	0.57%	45.12%	0.4569	0.63%	54.31%	0.3778	0.67%	62.22%	0.3068	0.59%	69.32%	0.2493	1.08%	75.07%
	50k s3	0.5597	1.07%	44.03%	0.4620	1.05%	53.80%	0.3764	1.11%	62.36%	0.3059	1.04%	69.41%	0.2541	1.09%	74.59%
	50k s4	0.5569	0.63%	44.31%	0.4596	0.98%	54.04%	0.3729	0.92%	62.71%	0.3111	1.00%	68.89%	0.2523	0.97%	74.77%
	50k s5	0.5515	0.65%	44.85%	0.4544	0.37%	54.56%	0.3688	0.79%	63.12%	0.3052	0.86%	69.48%	0.2445	0.69%	75.55%
Particle	Primary & Seeds	320 cm			340 cm			360 cm			380 cm			400 cm		
		D _{norm}	E _{Dnorm}	δD												
neutron	5k s1	0.1881	3.04%	81.19%	0.1599	3.12%	84.01%	0.1232	5.35%	87.68%	0.0991	2.31%	90.09%	0.0871	2.60%	91.29%
	5k s2	0.1947	5.36%	80.53%	0.1542	3.69%	84.58%	0.1309	3.56%	86.91%	0.0976	5.30%	90.24%	0.0822	3.19%	91.78%
	5k s3	0.1902	3.26%	80.98%	0.1548	4.37%	84.52%	0.1316	2.14%	86.84%	0.1011	2.99%	89.89%	0.0740	1.61%	92.60%
	5k s4	0.1784	2.76%	82.16%	0.1579	3.57%	84.21%	0.1206	4.17%	87.94%	0.1079	2.86%	89.21%	0.0828	4.66%	91.72%
	5k s5	0.2065	2.92%	79.35%	0.1636	2.92%	83.64%	0.1247	2.79%	87.53%	0.1071	7.01%	89.29%	0.0877	2.71%	91.23%
	10k s1	0.1967	1.87%	80.33%	0.1639	2.77%	83.61%	0.1254	1.82%	87.46%	0.0997	2.72%	90.03%	0.0882	2.65%	91.18%
	10k s2	0.1963	1.94%	80.37%	0.1713	2.65%	82.87%	0.1318	3.44%	86.82%	0.1133	4.16%	88.67%	0.0855	3.53%	91.45%
	10k s3	0.1981	3.04%	80.19%	0.1656	2.38%	83.44%	0.1310	4.10%	86.90%	0.1049	3.26%	89.51%	0.0849	2.07%	91.51%
	10k s4	0.1961	1.59%	80.39%	0.1647	2.05%	83.53%	0.1305	1.50%	86.95%	0.1063	2.91%	89.37%	0.0848	3.26%	91.52%
	10k s5	0.2082	2.91%	79.18%	0.1645	2.61%	83.55%	0.1294	1.65%	87.06%	0.1071	2.29%	89.29%	0.0812	5.11%	91.88%
	50k s1	0.2027	0.87%	79.73%	0.1612	0.72%	83.88%	0.1323	1.61%	86.77%	0.1012	0.84%	89.88%	0.0853	1.46%	91.47%
	50k s2	0.2054	1.22%	79.46%	0.1669	1.19%	83.31%	0.1315	1.47%	86.85%	0.1059	1.46%	89.41%	0.0855	1.84%	91.45%
	50k s3	0.2037	0.94%	79.63%	0.1667	0.75%	83.33%	0.1332	0.88%	86.68%	0.1067	1.03%	89.33%	0.0859	1.69%	91.41%
	50k s4	0.2019	1.27%	79.81%	0.1659	0.90%	83.41%	0.1325	1.43%	86.75%	0.1091	1.67%	89.09%	0.0842	1.56%	91.58%
	50k s5	0.2020	1.08%	79.80%	0.1618	0.90%	83.82%	0.1292	0.80%	87.08%	0.1046	0.97%	89.54%	0.0857	0.82%	91.43%



Dose Reduction Tables for All Assessed Materials

Table C.1: Dose reduction from 740 MeV neutron beams of all assessed materials with a shield thickness range of 20-100 cm. D_{norm} is the normalized dose, $E_{D_{norm}}$ is the error of the normalized dose and δD is the dose reduction.

Material	Particle	Shield thickness														
		20 cm			40 cm			60 cm			80 cm			100 cm		
		D_{norm}	$E_{D_{norm}}$	δD	D_{norm}	$E_{D_{norm}}$	δD	D_{norm}	$E_{D_{norm}}$	δD	D_{norm}	$E_{D_{norm}}$	δD	D_{norm}	$E_{D_{norm}}$	δD
LH2	neutron	1.1295	2.14%	-12.95%	1.2007	2.12%	-20.07%	1.2922	1.91%	-29.22%	1.3670	2.08%	-36.70%	1.4260	2.04%	-42.60%
H2O		1.6705	1.98%	-67.05%	1.9245	1.97%	-92.45%	1.9999	1.97%	-99.99%	1.9176	2.00%	-91.76%	1.8048	1.98%	-80.48%
Al		1.9453	2.16%	-94.53%	1.8962	2.02%	-89.62%	1.5905	2.06%	-59.05%	1.2692	2.16%	-26.92%	0.9640	2.35%	3.60%
Pb		2.0841	1.94%	-108.41%	1.5883	1.94%	-58.83%	1.0708	1.97%	-7.08%	0.6721	1.94%	32.79%	0.4045	1.90%	59.55%
ABS		1.7004	2.11%	-70.04%	1.9510	1.94%	-95.10%	1.9935	2.11%	-99.35%	1.9355	2.13%	-93.55%	1.7637	1.97%	-76.37%
ASA		1.7329	2.08%	-73.29%	1.9684	1.97%	-96.84%	1.9892	2.33%	-98.92%	1.8681	2.20%	-86.81%	1.7455	1.99%	-74.55%
COC		1.7111	2.04%	-71.11%	1.9628	1.99%	-96.28%	2.0308	2.01%	-103.08%	1.9308	2.09%	-93.08%	1.7609	1.94%	-76.09%
LCP		1.8155	1.95%	-81.55%	2.0472	1.95%	-104.72%	1.9560	2.22%	-95.60%	1.7447	1.92%	-74.47%	1.5100	2.06%	-51.00%
PC		1.7229	1.93%	-72.29%	1.9877	2.04%	-98.77%	1.9961	1.91%	-99.61%	1.8241	1.96%	-82.41%	1.6525	2.01%	-65.25%
PE		1.6670	2.13%	-66.70%	1.9533	2.02%	-95.33%	2.0188	1.90%	-101.88%	1.9614	1.98%	-96.14%	1.8155	1.91%	-81.55%
PEEK		1.7908	2.06%	-79.08%	2.0308	2.09%	-103.08%	1.9739	2.06%	-97.39%	1.8136	1.98%	-81.36%	1.6324	1.99%	-63.24%
PEI		1.7816	1.98%	-78.16%	2.0056	2.04%	-100.56%	1.9676	1.95%	-96.76%	1.8255	1.98%	-82.55%	1.6115	2.03%	-61.15%
PEKK		1.7802	2.08%	-78.02%	2.0058	2.09%	-100.58%	1.9578	2.00%	-95.78%	1.8091	1.92%	-80.91%	1.6058	1.98%	-60.58%
PET		1.7805	2.05%	-78.05%	2.0181	2.01%	-101.81%	1.9622	1.95%	-96.22%	1.7857	1.97%	-78.57%	1.5928	2.24%	-59.28%
PI		1.8053	2.04%	-80.53%	2.0061	1.97%	-100.61%	1.9426	1.94%	-94.26%	1.7582	2.16%	-75.82%	1.5345	2.00%	-53.45%
PLA		1.7612	1.95%	-76.12%	1.9886	1.90%	-98.86%	1.9372	1.93%	-93.72%	1.8366	2.09%	-83.66%	1.6234	2.12%	-62.34%
PMMA		1.7504	1.93%	-75.04%	1.9789	1.96%	-97.89%	1.9907	1.96%	-99.07%	1.8984	1.98%	-89.84%	1.6958	2.05%	-69.58%
POM		1.8139	2.13%	-81.39%	2.0051	1.99%	-100.51%	1.9395	2.03%	-93.95%	1.7326	2.06%	-73.26%	1.4984	2.06%	-49.84%
PP		1.6441	2.04%	-64.41%	1.9525	1.90%	-95.25%	2.0070	1.92%	-100.70%	1.9875	1.98%	-98.75%	1.8370	2.04%	-83.70%
PS		1.7071	2.09%	-70.71%	1.9518	1.95%	-95.18%	1.9801	2.07%	-98.01%	1.9158	1.96%	-91.58%	1.7477	1.97%	-74.77%
PVC	1.7538	2.09%	-75.38%	1.9265	1.97%	-92.65%	1.9226	2.10%	-92.26%	1.7688	2.07%	-76.88%	1.5587	2.03%	-55.87%	
MGS1	1.6814	2.12%	-68.14%	1.8840	2.09%	-88.40%	1.9209	1.93%	-92.09%	1.8203	1.99%	-82.03%	1.6637	1.97%	-66.37%	

Table C.2: Dose reduction from 740 MeV neutron beams of all assessed materials with a shield thickness range of 120-200 cm. D_{norm} is the normalized dose, $E_{D_{norm}}$ is the error of the normalized dose and δD is the dose reduction.

Material	Particle	Shield thickness														
		120 cm			140 cm			160 cm			180 cm			200 cm		
		D_{norm}	$E_{D_{norm}}$	δD	D_{norm}	$E_{D_{norm}}$	δD	D_{norm}	$E_{D_{norm}}$	δD	D_{norm}	$E_{D_{norm}}$	δD	D_{norm}	$E_{D_{norm}}$	δD
LH2	neutron	1.4788	2.01%	-47.88%	1.5139	1.97%	-51.39%	1.5585	2.29%	-55.85%	1.5757	1.92%	-57.57%	1.5589	2.33%	-55.89%
H2O		1.6419	2.17%	-64.19%	1.4462	1.97%	-44.62%	1.2658	1.90%	-26.58%	1.1102	2.24%	-11.02%	0.9442	2.02%	5.58%
Al		0.7106	2.16%	28.94%	0.5224	1.98%	47.76%	0.3615	2.57%	63.85%	0.2629	2.84%	73.71%	0.1856	3.29%	81.44%
Pb		0.2372	2.11%	76.28%	0.1343	2.12%	86.57%	0.0772	2.18%	92.28%	0.0418	2.26%	95.82%	0.0232	1.94%	97.68%
ABS		1.6069	1.91%	-60.69%	1.3762	1.96%	-37.62%	1.1921	1.96%	-19.21%	1.0104	2.00%	-1.04%	0.8432	2.01%	15.68%
ASA		1.5546	1.97%	-55.46%	1.3575	1.90%	-35.75%	1.1784	2.03%	-17.84%	0.9836	2.15%	1.64%	0.8286	2.00%	17.14%
COC		1.5942	2.17%	-59.42%	1.3944	2.15%	-39.44%	1.2058	2.33%	-20.58%	1.0394	2.26%	-3.94%	0.8670	2.09%	13.30%
LCP		1.2875	1.91%	-28.75%	1.0666	1.91%	-6.66%	0.8596	2.14%	14.04%	0.6798	1.97%	32.02%	0.5460	2.30%	45.40%
PC		1.4440	2.07%	-44.40%	1.2506	2.13%	-25.06%	1.0373	2.37%	-3.73%	0.8678	2.36%	13.22%	0.7031	2.16%	29.69%
PE		1.6748	2.01%	-67.48%	1.4894	1.98%	-48.94%	1.2965	2.38%	-29.65%	1.1220	1.97%	-12.20%	0.9577	1.93%	4.23%
PEEK		1.3834	2.05%	-38.34%	1.1739	1.94%	-17.39%	0.9872	2.46%	1.28%	0.8195	1.97%	18.05%	0.6616	2.01%	33.84%
PEI		1.3826	1.91%	-38.26%	1.2006	2.01%	-20.06%	0.9846	1.95%	1.54%	0.8129	1.97%	18.71%	0.6621	2.52%	33.79%
PEKK		1.3974	2.09%	-39.74%	1.1881	1.95%	-18.81%	0.9745	2.36%	2.55%	0.7955	1.98%	20.45%	0.6525	1.97%	34.75%
PET		1.3287	2.09%	-32.87%	1.1301	2.10%	-13.01%	0.9177	2.13%	8.23%	0.7513	2.28%	24.87%	0.6160	2.46%	38.40%
PI		1.2766	2.05%	-27.66%	1.0621	2.19%	-6.21%	0.8672	2.26%	13.28%	0.6827	2.13%	31.73%	0.5391	2.64%	46.09%
PLA		1.4297	1.98%	-42.97%	1.2079	2.17%	-20.79%	1.0126	2.00%	-1.26%	0.8419	2.21%	15.81%	0.6780	2.17%	32.20%
PMMA		1.4855	1.97%	-48.55%	1.3023	2.08%	-30.23%	1.0870	2.00%	-8.70%	0.9046	2.06%	9.54%	0.7407	1.93%	25.93%
POM		1.2742	2.28%	-27.42%	1.0327	2.14%	-3.27%	0.8236	2.19%	17.64%	0.6670	2.15%	33.30%	0.5348	2.29%	46.52%
PP		1.7110	1.92%	-71.10%	1.5393	2.13%	-53.93%	1.3285	2.02%	-32.85%	1.1671	2.05%	-16.71%	1.0250	2.03%	-2.50%
PS		1.5609	2.10%	-56.09%	1.3804	1.97%	-38.04%	1.1647	1.93%	-16.47%	1.0114	2.13%	-1.14%	0.8288	2.21%	17.12%
PVC	1.3589	2.29%	-35.89%	1.1453	2.01%	-14.53%	0.9565	2.01%	4.35%	0.8012	2.13%	19.88%	0.6538	2.15%	34.62%	
MGS1	1.4783	2.01%	-47.83%	1.2833	2.03%	-28.33%	1.1105	1.96%	-11.05%	0.9783	2.12%	2.17%	0.8072	2.72%	19.28%	

Table C.3: Dose reduction from 1 GeV proton beams of all assessed materials with a shield thickness range of 20-100 cm. D_{norm} is the normalized dose, $E_{D_{norm}}$ is the error of the normalized dose and δD is the dose reduction.

Material	Particle	Shield thickness														
		20 cm			40 cm			60 cm			80 cm			100 cm		
		D_{norm}	$E_{D_{norm}}$	δD	D_{norm}	$E_{D_{norm}}$	δD	D_{norm}	$E_{D_{norm}}$	δD	D_{norm}	$E_{D_{norm}}$	δD	D_{norm}	$E_{D_{norm}}$	δD
LH2	proton	1.0554	0.41%	-5.54%	1.1186	0.59%	-11.86%	1.1342	0.56%	-13.42%	1.1652	0.45%	-16.52%	1.1808	0.65%	-18.08%
H2O		1.2205	0.47%	-22.05%	1.2499	0.53%	-24.99%	1.2030	0.47%	-20.30%	1.1151	0.59%	-11.51%	0.9881	0.60%	1.19%
Al		1.2265	0.49%	-22.65%	1.0477	0.64%	-4.77%	0.7803	0.65%	21.97%	0.5467	0.85%	45.33%	0.3655	0.75%	63.45%
Pb		0.9615	0.49%	3.85%	0.5235	0.49%	47.65%	0.2190	0.64%	78.10%	0.1242	0.59%	87.58%	0.0722	0.72%	92.78%
ABS		1.2106	0.44%	-21.06%	1.2458	0.59%	-24.58%	1.1919	0.46%	-19.19%	1.0862	0.47%	-8.62%	0.9562	0.47%	4.38%
ASA		1.2254	0.54%	-22.54%	1.2462	0.43%	-24.62%	1.1908	0.57%	-19.08%	1.0748	0.42%	-7.48%	0.9427	0.95%	5.73%
COC		1.2322	0.48%	-23.22%	1.2531	0.58%	-25.31%	1.1932	0.56%	-19.32%	1.0830	0.50%	-8.30%	0.9500	0.50%	5.00%
LCP		1.2406	0.46%	-24.06%	1.2265	0.47%	-22.65%	1.0986	0.62%	-9.86%	0.9408	0.48%	5.92%	0.7677	0.68%	23.23%
PC		1.2266	0.67%	-22.66%	1.2398	0.45%	-23.98%	1.1623	0.53%	-16.23%	1.0231	0.67%	-2.31%	0.8708	0.66%	12.92%
PE		1.2159	0.44%	-21.59%	1.2618	0.58%	-26.18%	1.2087	0.60%	-20.87%	1.1178	0.69%	-11.78%	0.9954	0.45%	0.46%
PEEK		1.2375	0.64%	-23.75%	1.2385	0.59%	-23.85%	1.1476	0.41%	-14.76%	0.9986	0.49%	0.14%	0.8443	0.66%	15.57%
PEI		1.2320	0.68%	-23.20%	1.2291	0.58%	-22.91%	1.1371	0.54%	-13.71%	1.0023	0.44%	-0.23%	0.8433	0.74%	15.67%
PEKK		1.2262	0.53%	-22.62%	1.2314	0.51%	-23.14%	1.1455	0.60%	-14.55%	0.9938	0.63%	0.62%	0.8382	0.69%	16.18%
PET		1.2325	0.51%	-23.25%	1.2276	0.58%	-22.76%	1.1297	0.66%	-12.97%	0.9803	0.55%	1.97%	0.8098	0.49%	19.02%
PI		1.2272	0.50%	-22.72%	1.2164	0.63%	-21.64%	1.0968	0.48%	-9.68%	0.9378	0.53%	6.22%	0.7666	0.53%	23.34%
PLA		1.2322	0.67%	-23.22%	1.2384	0.43%	-23.84%	1.1470	0.49%	-14.70%	1.0096	0.62%	-0.96%	0.8548	0.52%	14.52%
PMMA		1.2295	0.51%	-22.95%	1.2543	0.47%	-25.43%	1.1609	0.42%	-16.09%	1.0431	0.43%	-4.31%	0.8910	0.66%	10.90%
POM		1.2450	0.46%	-24.50%	1.2118	0.42%	-21.18%	1.0954	0.70%	-9.54%	0.9218	0.62%	7.82%	0.7451	0.43%	25.49%
PP		1.2202	0.65%	-22.02%	1.2629	0.56%	-26.29%	1.2216	0.52%	-22.16%	1.1368	0.51%	-13.68%	1.0155	0.61%	-1.55%
PS		1.2197	0.61%	-21.97%	1.2477	0.61%	-24.77%	1.1891	0.54%	-18.91%	1.0838	0.57%	-8.38%	0.9435	0.43%	5.65%
PVC	1.2344	0.75%	-23.44%	1.2218	0.42%	-22.18%	1.1094	0.48%	-10.94%	0.9755	0.46%	2.45%	0.8202	0.66%	17.98%	
MGS1	1.2078	0.44%	-20.78%	1.2204	0.68%	-22.04%	1.1368	0.53%	-13.68%	1.0371	0.64%	-3.71%	0.8980	0.77%	10.20%	

Table C.4: Dose reduction from 1 GeV proton beams of all assessed materials with a shield thickness range of 120-200 cm. D_{norm} is the normalized dose, $E_{D_{norm}}$ is the error of the normalized dose and δD is the dose reduction.

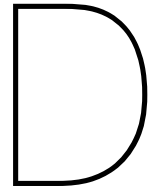
Material	Particle	Shield thickness														
		120 cm			140 cm			160 cm			180 cm			200 cm		
		D_{norm}	$E_{D_{norm}}$	δD	D_{norm}	$E_{D_{norm}}$	δD	D_{norm}	$E_{D_{norm}}$	δD	D_{norm}	$E_{D_{norm}}$	δD	D_{norm}	$E_{D_{norm}}$	δD
LH2	proton	1.1905	0.49%	-19.05%	1.2073	0.54%	-20.73%	1.2042	0.80%	-20.42%	1.2101	0.42%	-21.01%	1.1952	0.49%	-19.52%
H2O		0.8607	0.41%	13.93%	0.7178	0.50%	28.22%	0.6017	0.44%	39.83%	0.4900	0.45%	51.00%	0.3896	0.96%	61.04%
Al		0.2269	1.28%	77.31%	0.1403	1.37%	85.97%	0.0514	1.41%	94.86%	0.0341	2.50%	96.59%	0.0222	2.31%	97.78%
Pb		0.0405	0.45%	95.95%	0.0228	0.63%	97.72%	0.0129	0.64%	98.71%	0.0069	0.67%	99.31%	0.0038	1.58%	99.62%
ABS		0.8158	0.73%	18.42%	0.6747	0.44%	32.53%	0.5589	0.53%	44.11%	0.4475	0.72%	55.25%	0.3476	0.63%	65.24%
ASA		0.8079	0.69%	19.21%	0.6622	0.95%	33.78%	0.5386	0.51%	46.14%	0.4267	0.87%	57.33%	0.3345	1.07%	66.55%
COC		0.8152	0.87%	18.48%	0.6769	0.54%	32.31%	0.5489	0.69%	45.11%	0.4375	0.44%	56.25%	0.3441	0.70%	65.59%
LCP		0.5954	0.83%	40.46%	0.4593	0.65%	54.07%	0.3364	0.72%	66.36%	0.2453	0.51%	75.47%	0.1690	0.67%	83.10%
PC		0.7207	0.63%	27.93%	0.5862	0.67%	41.38%	0.4530	0.83%	54.70%	0.3508	1.15%	64.92%	0.2693	1.58%	73.07%
PE		0.8632	0.62%	13.68%	0.7303	0.64%	26.97%	0.6093	0.70%	39.07%	0.4921	0.78%	50.79%	0.3959	0.82%	60.41%
PEEK		0.6889	0.68%	31.11%	0.5438	0.65%	45.62%	0.4165	0.80%	58.35%	0.3219	0.66%	67.81%	0.2381	1.26%	76.19%
PEI		0.6799	0.61%	32.01%	0.5424	0.51%	45.76%	0.4113	0.69%	58.87%	0.3149	0.68%	68.51%	0.2331	0.64%	76.69%
PEKK		0.6787	0.78%	32.13%	0.5313	0.68%	46.87%	0.4083	0.88%	59.17%	0.3106	1.02%	68.94%	0.2293	1.47%	77.07%
PET		0.6476	0.85%	35.24%	0.5056	0.62%	49.44%	0.3877	0.67%	61.23%	0.2842	0.86%	71.58%	0.2081	0.82%	79.19%
PI		0.6058	0.55%	39.42%	0.4541	0.86%	54.59%	0.3441	0.84%	65.59%	0.2465	0.58%	75.35%	0.1750	0.86%	82.50%
PLA		0.6946	0.57%	30.54%	0.5539	0.74%	44.61%	0.4284	0.81%	57.16%	0.3233	1.09%	67.67%	0.2443	0.89%	75.57%
PMMA		0.7408	0.60%	25.92%	0.5993	0.64%	40.07%	0.4735	0.68%	52.65%	0.3636	0.73%	63.64%	0.2819	0.54%	71.81%
POM		0.5791	0.50%	42.09%	0.4352	0.87%	56.48%	0.3170	0.68%	68.30%	0.2271	0.55%	77.29%	0.1547	1.20%	84.53%
PP		0.8927	0.53%	10.73%	0.7595	0.72%	24.05%	0.6457	0.71%	35.43%	0.5363	0.86%	46.37%	0.4287	0.99%	57.13%
PS		0.8042	0.60%	19.58%	0.6740	0.54%	32.60%	0.5454	0.65%	45.46%	0.4311	0.64%	56.89%	0.3411	1.24%	65.89%
PVC	0.6567	0.58%	34.33%	0.5205	0.80%	47.95%	0.4016	0.57%	59.84%	0.3074	0.67%	69.26%	0.2286	0.81%	77.14%	
MGS1	0.7630	0.78%	23.70%	0.6404	0.77%	35.96%	0.5200	0.71%	48.00%	0.4200	0.80%	58.00%	0.3286	1.46%	67.14%	

Table C.5: Dose reduction from 1 GeV helium beams of all assessed materials with a shield thickness range of 20-100 cm. D_{norm} is the normalized dose, $E_{D_{norm}}$ is the error of the normalized dose and δD is the dose reduction.

Material	Particle	Shield thickness														
		20 cm			40 cm			60 cm			80 cm			100 cm		
		D_{norm}	$E_{D_{norm}}$	δD	D_{norm}	$E_{D_{norm}}$	δD	D_{norm}	$E_{D_{norm}}$	δD	D_{norm}	$E_{D_{norm}}$	δD	D_{norm}	$E_{D_{norm}}$	δD
LH2	helium	1.0390	0.04%	-3.90%	1.0798	0.07%	-7.98%	1.1211	0.10%	-12.11%	1.1633	0.05%	-16.33%	1.2185	0.10%	-21.85%
H2O		1.2100	0.24%	-21.00%	0.1145	0.55%	88.55%	0.0495	0.43%	95.05%	0.0271	1.84%	97.29%	0.0176	1.25%	98.24%
Al		0.0886	0.60%	91.14%	0.0299	0.52%	97.01%	0.0177	1.31%	98.23%	0.0115	1.40%	98.85%	0.0075	1.94%	99.25%
Pb		0.0300	0.82%	97.00%	0.0157	0.48%	98.43%	0.0090	0.97%	99.10%	0.0052	1.29%	99.48%	0.0029	0.71%	99.71%
ABS		1.1694	0.11%	-16.94%	0.1082	0.29%	89.18%	0.0471	1.55%	95.29%	0.0255	0.74%	97.45%	0.0170	0.64%	98.30%
ASA		1.1407	0.14%	-14.07%	0.1041	0.46%	89.59%	0.0450	0.84%	95.50%	0.0244	1.08%	97.56%	0.0160	2.55%	98.40%
COC		1.1991	0.12%	-19.91%	0.1177	0.56%	88.23%	0.0529	1.08%	94.71%	0.0291	1.22%	97.09%	0.0195	1.01%	98.05%
LCP		0.8862	0.15%	11.38%	0.0674	0.55%	93.26%	0.0304	0.74%	96.96%	0.0193	1.03%	98.07%	0.0130	1.09%	98.70%
PC		1.0513	0.26%	-5.13%	0.0871	0.63%	91.29%	0.0390	0.50%	96.10%	0.0228	0.24%	97.72%	0.0154	1.36%	98.46%
PE		1.2071	0.05%	-20.71%	0.1161	0.53%	88.39%	0.0510	0.94%	94.90%	0.0273	1.23%	97.27%	0.0170	0.16%	98.30%
PEEK		1.0071	0.21%	-0.71%	0.0814	0.84%	91.86%	0.0366	0.69%	96.34%	0.0212	1.39%	97.88%	0.0148	1.28%	98.52%
PEI		1.0114	0.24%	-1.14%	0.0812	0.78%	91.88%	0.0357	0.52%	96.43%	0.0212	0.79%	97.88%	0.0147	2.83%	98.53%
PEKK		0.9984	0.20%	0.16%	0.0809	0.59%	91.91%	0.0367	0.94%	96.33%	0.0208	0.70%	97.92%	0.0147	0.95%	98.53%
PET		0.9567	0.39%	4.33%	0.0744	0.91%	92.56%	0.0332	0.88%	96.68%	0.0197	1.84%	98.03%	0.0138	1.33%	98.62%
PI		0.8985	0.16%	10.15%	0.0679	0.85%	93.21%	0.0308	0.93%	96.92%	0.0190	1.83%	98.10%	0.0134	1.38%	98.66%
PLA		1.0223	0.23%	-2.23%	0.0821	0.55%	91.79%	0.0364	1.13%	96.36%	0.0213	2.19%	97.87%	0.0149	2.24%	98.51%
PMMA		1.0736	0.19%	-7.36%	0.0904	0.81%	90.96%	0.0398	0.86%	96.02%	0.0216	1.26%	97.84%	0.0147	1.32%	98.53%
POM		0.8409	0.38%	15.91%	0.0615	0.83%	93.85%	0.0274	1.45%	97.26%	0.0166	1.51%	98.34%	0.0121	2.60%	98.79%
PP		1.2419	0.27%	-24.19%	0.1285	0.30%	87.15%	0.0546	0.86%	94.54%	0.0291	0.49%	97.09%	0.0184	0.70%	98.16%
PS		1.1554	0.23%	-15.54%	0.1062	0.81%	89.38%	0.0456	1.01%	95.44%	0.0253	1.34%	97.47%	0.0171	1.97%	98.29%
PVC	1.0124	0.19%	-1.24%	0.0724	0.37%	92.76%	0.0330	1.57%	96.70%	0.0197	1.05%	98.03%	0.0142	1.34%	98.58%	
MGS1	1.1663	0.20%	-16.63%	0.0928	0.42%	90.72%	0.0460	0.67%	95.40%	0.0282	1.34%	97.18%	0.0200	1.00%	98.00%	

Table C.6: Dose reduction from 1 GeV carbon beams of all assessed materials with a shield thickness range of 20-100 cm. D_{norm} is the normalized dose, $E_{D_{norm}}$ is the error of the normalized dose and δD is the dose reduction.

Material	Particle	Shield thickness														
		20 cm			40 cm			60 cm			80 cm			100 cm		
		D_{norm}	$E_{D_{norm}}$	δD	D_{norm}	$E_{D_{norm}}$	δD	D_{norm}	$E_{D_{norm}}$	δD	D_{norm}	$E_{D_{norm}}$	δD	D_{norm}	$E_{D_{norm}}$	δD
LH2	carbon	0.9517	0.19%	4.83%	0.9038	0.21%	9.62%	0.8640	0.11%	13.60%	0.8291	0.23%	17.09%	0.8009	0.18%	19.91%
H2O		0.8351	0.11%	16.49%	0.7377	0.15%	26.23%	0.6633	0.21%	33.67%	0.5931	0.31%	40.69%	0.5088	0.19%	49.12%
Al		0.7734	0.16%	22.66%	0.6001	0.22%	39.99%	0.3531	0.20%	64.69%	0.2298	0.14%	77.02%	0.1473	0.32%	85.27%
Pb		0.3497	0.26%	65.03%	0.1652	0.32%	83.48%	0.0936	0.30%	90.64%	0.0553	0.23%	94.47%	0.0319	0.14%	96.81%
ABS		0.8743	0.18%	12.57%	0.7695	0.18%	23.05%	0.6714	0.20%	32.86%	0.5894	0.13%	41.06%	0.4481	0.14%	55.19%
ASA		0.8231	0.11%	17.69%	0.7208	0.13%	27.92%	0.6481	0.12%	35.19%	0.5797	0.14%	42.03%	0.4872	0.15%	51.28%
COC		0.8204	0.10%	17.96%	0.7212	0.09%	27.88%	0.6436	0.18%	35.64%	0.5721	0.16%	42.79%	0.4741	0.22%	52.59%
LCP		0.8134	0.12%	18.66%	0.7172	0.09%	28.28%	0.6432	0.17%	35.68%	0.5774	0.25%	42.26%	0.4837	0.14%	51.63%
PC		0.8043	0.20%	19.57%	0.6898	0.19%	31.02%	0.5937	0.27%	40.63%	0.4784	0.16%	52.16%	0.3666	0.15%	63.34%
PE		0.8165	0.17%	18.35%	0.7126	0.15%	28.74%	0.6285	0.24%	37.15%	0.5496	0.14%	45.04%	0.4299	0.16%	57.01%
PEEK		0.8161	0.12%	18.39%	0.7227	0.12%	27.73%	0.6556	0.16%	34.44%	0.5902	0.25%	40.98%	0.5130	0.12%	48.70%
PEI		0.8100	0.14%	19.00%	0.7039	0.22%	29.61%	0.6159	0.13%	38.41%	0.5259	0.20%	47.41%	0.4100	0.20%	59.00%
PEKK		0.8119	0.14%	18.81%	0.7039	0.13%	29.61%	0.6167	0.23%	38.33%	0.5257	0.26%	47.43%	0.4085	0.21%	59.15%
PET		0.8107	0.18%	18.93%	0.7033	0.24%	29.67%	0.6132	0.12%	38.68%	0.5218	0.25%	47.82%	0.4058	0.21%	59.42%
PI		0.8081	0.21%	19.19%	0.6998	0.15%	30.02%	0.6068	0.16%	39.32%	0.5039	0.18%	49.61%	0.3874	0.22%	61.26%
PLA		0.8023	0.13%	19.77%	0.6891	0.21%	31.09%	0.5923	0.20%	40.77%	0.4745	0.14%	52.55%	0.3643	0.18%	63.57%
PMMA		0.8166	0.22%	18.34%	0.7101	0.17%	28.99%	0.6179	0.13%	38.21%	0.5335	0.19%	46.65%	0.4136	0.27%	58.64%
POM		0.7878	0.11%	21.22%	0.6769	0.16%	32.31%	0.5804	0.20%	41.96%	0.4523	0.20%	54.77%	0.3493	0.21%	65.07%
PP		0.7965	0.17%	20.35%	0.6854	0.17%	31.46%	0.5874	0.22%	41.26%	0.4564	0.18%	54.36%	0.3518	0.14%	64.82%
PS		0.8212	0.16%	17.88%	0.7291	0.12%	27.09%	0.6621	0.16%	33.79%	0.5987	0.29%	40.13%	0.5298	0.25%	47.02%
PVC	0.8207	0.14%	17.93%	0.7198	0.18%	28.02%	0.6470	0.24%	35.30%	0.5747	0.13%	42.53%	0.4815	0.20%	51.85%	
MGS1	0.8352	0.18%	16.48%	0.7197	0.14%	28.03%	0.6224	0.20%	37.76%	0.5142	0.15%	48.58%	0.3803	0.22%	61.97%	



Dose Reduction Plots for All Assessed Materials for Varying Shield Thicknesses

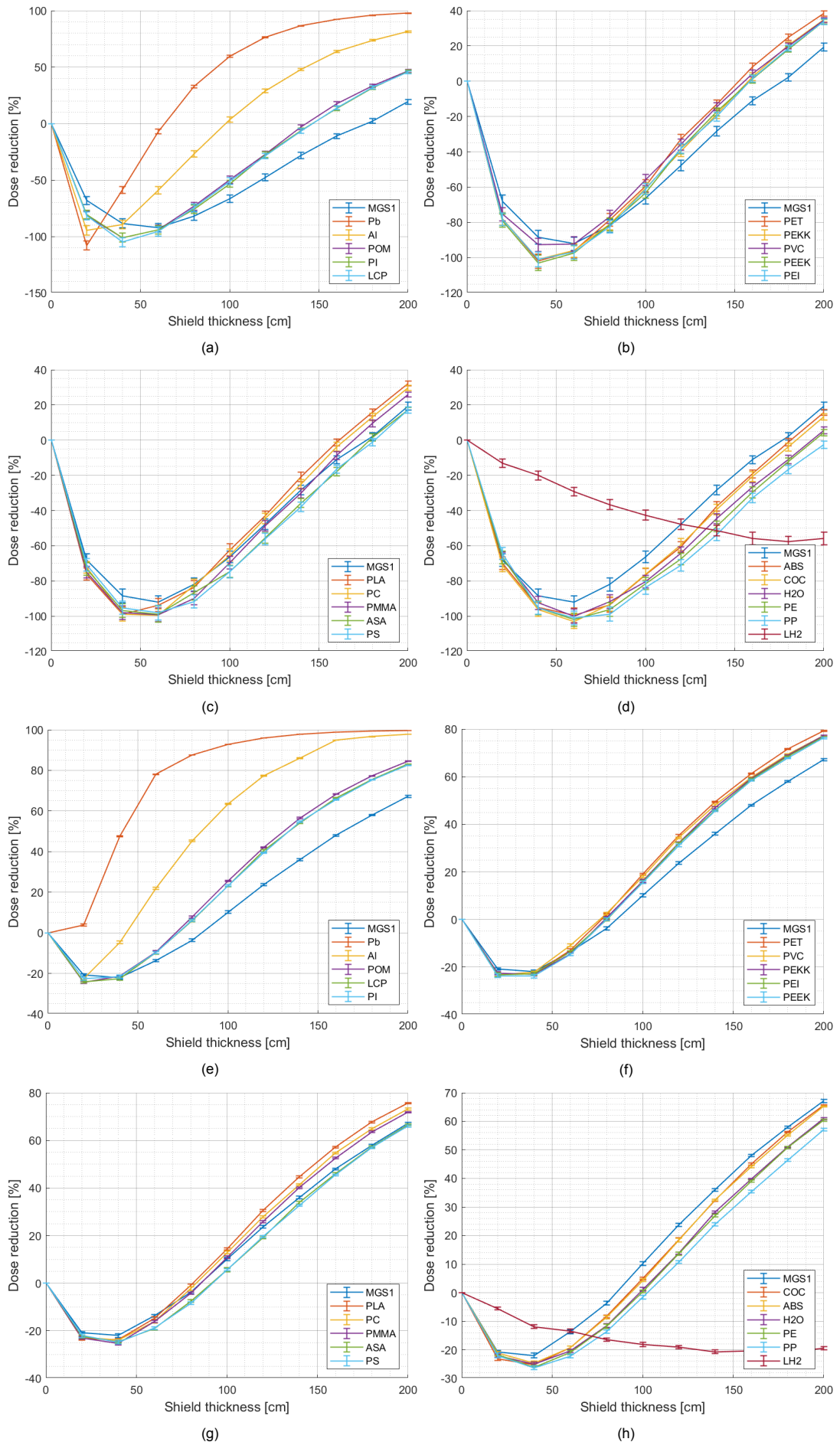


Figure D.1: The dose reduction (%) with respect to shield thickness (cm) for (a),(b),(c),(d) 740 MeV neutron and (e),(f),(g),(h) 1 GeV proton beams.

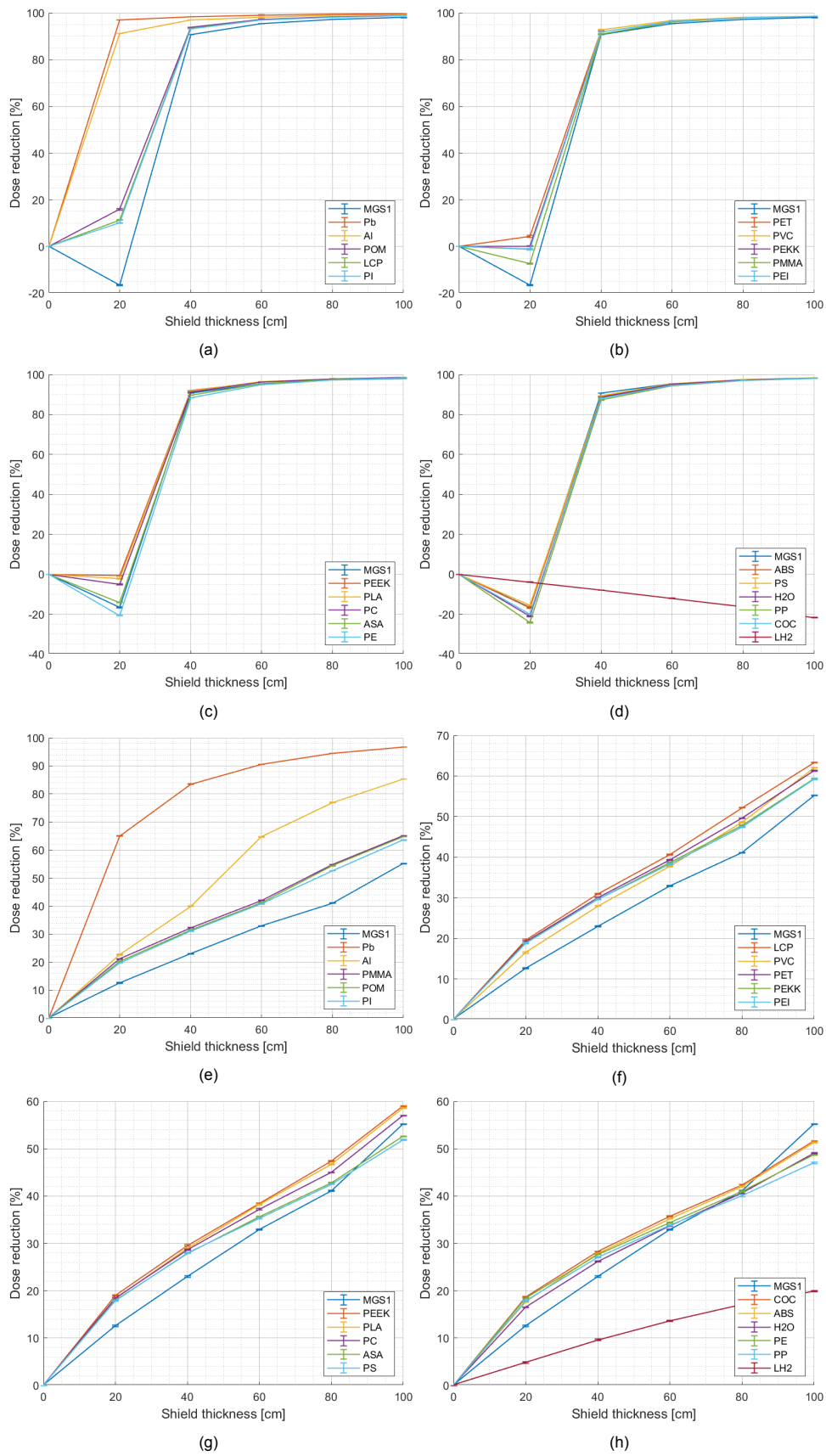
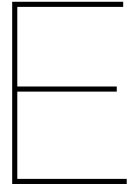


Figure D.2: The dose reduction (%) with respect to shield thickness (cm) for 1 GeV (a),(b),(c),(d) helium and (e),(f),(g),(h) carbon beams.



Dose Reduction Plots for All Assessed Materials for Varying Area Densities

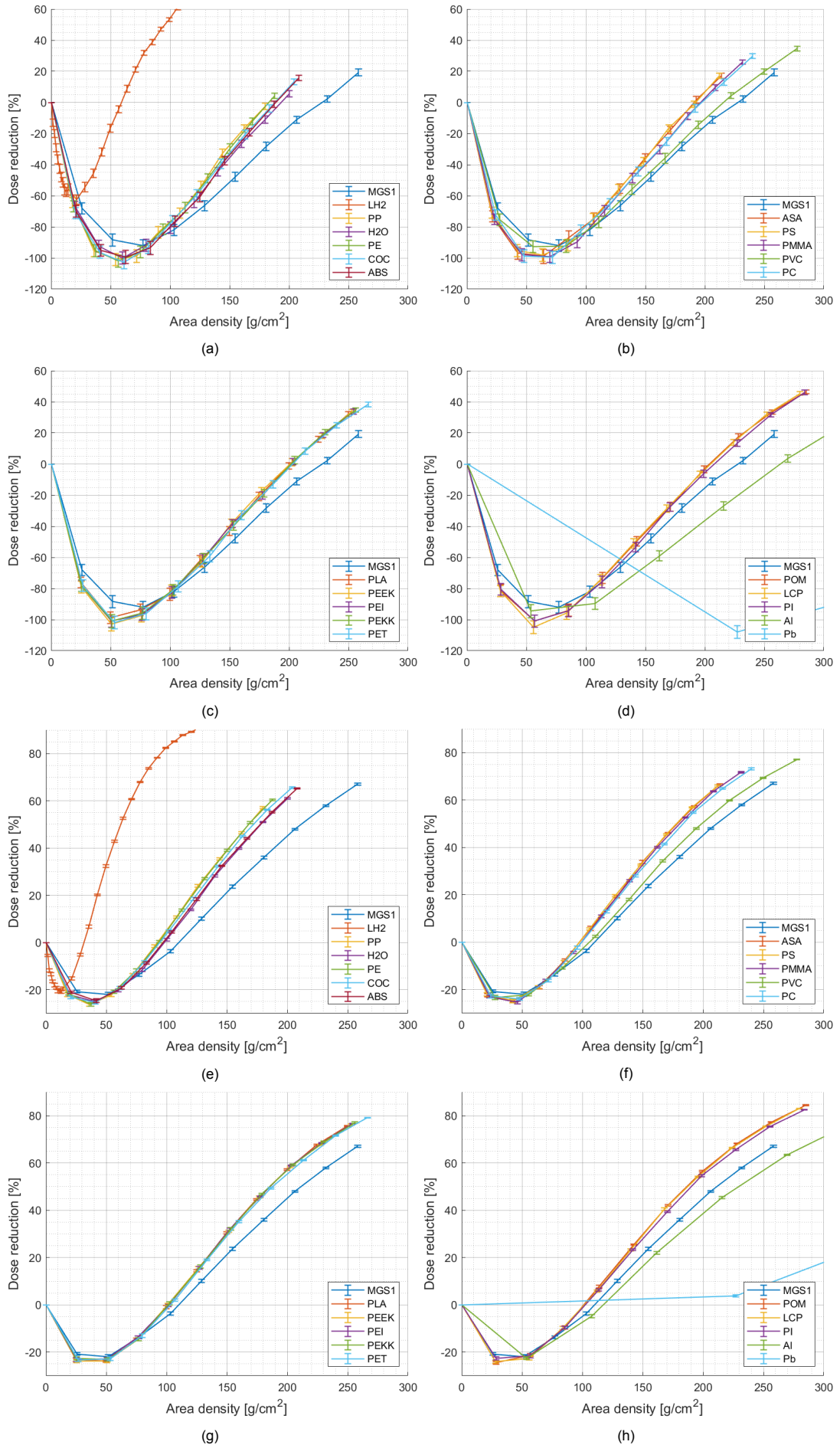


Figure E.1: The dose reduction (%) with respect to area density (g/cm^2) for (a),(b),(c),(d) 740 MeV neutron and (e),(f),(g),(h) 1 GeV proton beams.

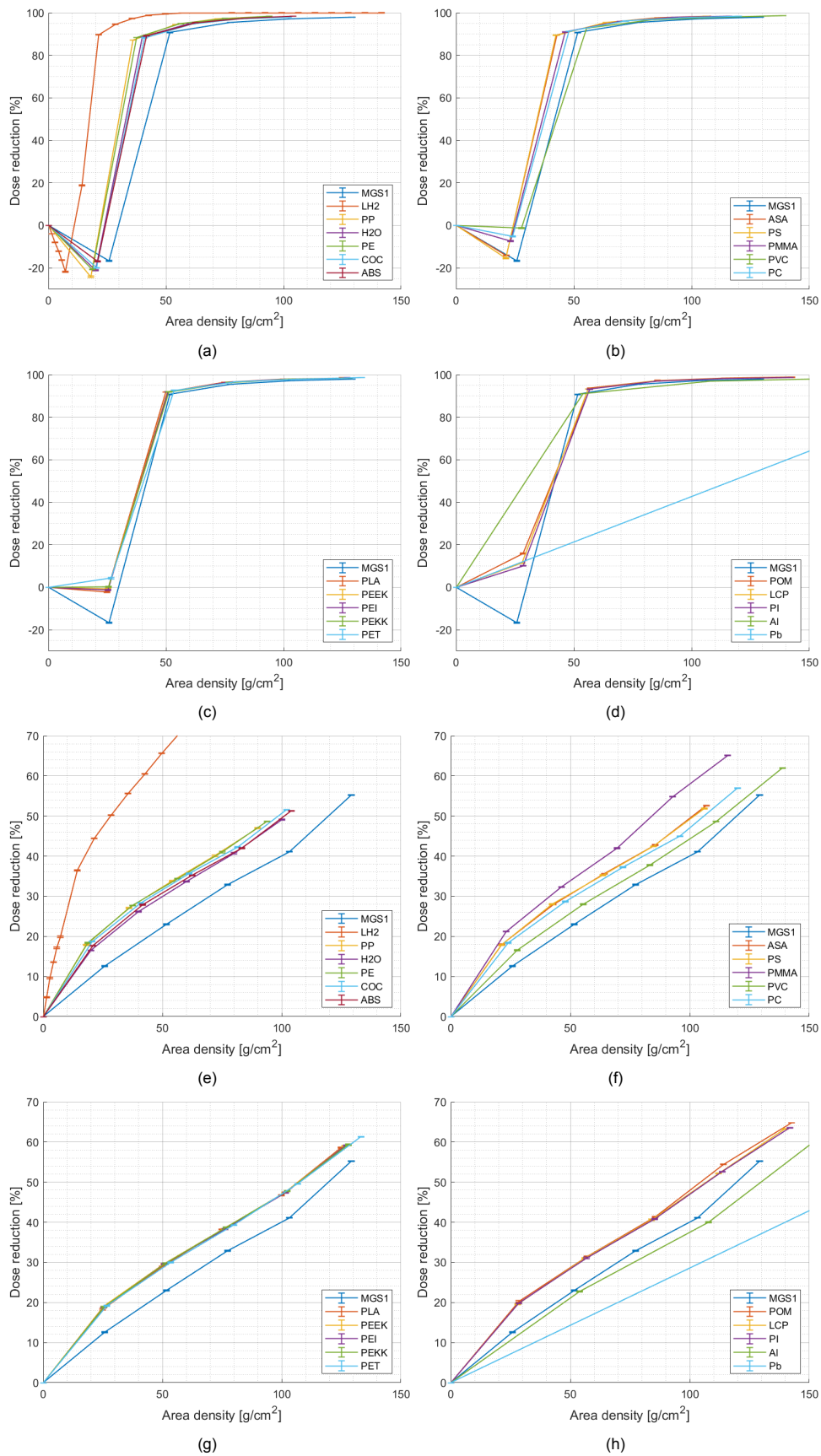
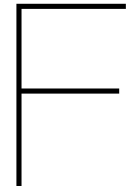


Figure E.2: The dose reduction (%) with respect to area density (g/cm^2) for 1 GeV (a),(b),(c),(d) helium and (e),(f),(g),(h) carbon beams.



Dose Reduction Tables for an MGS-1 Shield

Table F.1: Effect of the density for 740 MeV neutron and 1 GeV proton, helium, carbon, oxygen, silicon and iron beams on the dose reduction of an MGS-1 shield with a thickness range of 20-100 cm. D_{norm} is the normalized dose, $E_{D_{norm}}$ is the error of the normalized dose and δD is the dose reduction.

Particle	Density [g/cm ³]	Shield thickness														
		20 cm			40 cm			60 cm			80 cm			100 cm		
		D_{norm}	$E_{D_{norm}}$	δD	D_{norm}	$E_{D_{norm}}$	δD	D_{norm}	$E_{D_{norm}}$	δD	D_{norm}	$E_{D_{norm}}$	δD	D_{norm}	$E_{D_{norm}}$	δD
neutron	1.00	1.5898	2.18%	-58.98%	1.8191	1.98%	-81.91%	1.8969	1.95%	-89.69%	1.8736	2.13%	-87.36%	1.7651	2.12%	-76.51%
	1.29	1.6814	2.12%	-68.14%	1.8840	2.09%	-88.40%	1.9209	1.93%	-92.09%	1.8203	1.99%	-82.03%	1.6637	1.97%	-66.37%
	1.50	1.7640	1.96%	-76.40%	1.9498	1.97%	-94.98%	1.8950	2.08%	-89.50%	1.7359	2.03%	-73.59%	1.5472	1.95%	-54.72%
	2.00	1.8484	1.92%	-84.84%	1.9506	1.93%	-95.06%	1.7925	2.15%	-79.25%	1.5328	1.92%	-53.28%	1.2450	2.14%	-24.50%
	2.49	1.9295	2.03%	-92.95%	1.8947	1.94%	-89.47%	1.6146	1.98%	-61.46%	1.2964	2.04%	-29.64%	1.0012	1.90%	-0.12%
proton	1.00	1.1788	0.52%	-17.88%	1.2229	0.51%	-22.29%	1.1949	0.57%	-19.49%	1.1298	0.45%	-12.98%	1.0325	0.59%	-3.25%
	1.29	1.2078	0.44%	-20.78%	1.2204	0.68%	-22.04%	1.1368	0.53%	-13.68%	1.0371	0.64%	-3.71%	0.8980	0.77%	10.20%
	1.50	1.2109	0.50%	-21.09%	1.2080	0.55%	-20.80%	1.0992	0.66%	-9.92%	0.9578	0.63%	4.22%	0.7993	0.83%	20.07%
	2.00	1.2270	0.73%	-22.70%	1.1458	0.51%	-14.58%	0.9662	0.55%	3.38%	0.7669	0.56%	23.31%	0.5664	0.49%	43.36%
	2.49	1.2234	0.50%	-22.34%	1.0735	0.55%	-7.35%	0.8222	0.51%	17.78%	0.5866	0.62%	41.34%	0.3947	0.83%	60.53%
helium	1.00	1.1745	0.08%	-17.45%	0.5714	0.14%	42.86%	0.0703	1.15%	92.97%	0.0419	1.03%	95.81%	0.0285	1.35%	97.15%
	1.29	1.1663	0.20%	-16.63%	0.0928	0.42%	90.72%	0.0460	0.67%	95.40%	0.0282	1.34%	97.18%	0.0200	1.00%	98.00%
	1.50	1.0103	0.22%	-1.03%	0.0710	0.97%	92.90%	0.0356	0.65%	96.44%	0.0231	0.69%	97.69%	0.0172	1.14%	98.28%
	2.00	0.5727	0.14%	42.73%	0.0436	1.21%	95.64%	0.0246	0.75%	97.54%	0.0166	0.12%	98.34%	0.0114	1.19%	98.86%
	2.49	0.1000	0.63%	90.00%	0.0315	0.74%	96.85%	0.0185	1.18%	98.15%	0.0122	1.90%	98.78%	0.0079	1.24%	99.21%
carbon	1.00	0.8984	0.18%	10.16%	0.8099	0.17%	19.01%	0.7296	0.13%	27.04%	0.6544	0.20%	34.56%	0.5914	0.26%	40.86%
	1.29	0.8743	0.18%	12.57%	0.7695	0.18%	23.05%	0.6714	0.20%	32.86%	0.5894	0.13%	41.06%	0.4481	0.14%	55.19%
	1.50	0.8558	0.18%	14.42%	0.7361	0.18%	26.39%	0.6296	0.25%	37.04%	0.5145	0.30%	48.55%	0.3626	0.11%	63.74%
	2.00	0.8153	0.16%	18.47%	0.6661	0.24%	33.39%	0.5215	0.11%	47.85%	0.3389	0.21%	66.11%	0.2409	0.21%	75.91%
	2.49	0.7770	0.15%	22.30%	0.6109	0.20%	38.91%	0.3742	0.17%	62.58%	0.2477	0.23%	75.23%	0.1600	0.28%	84.00%
oxygen	1.00	0.8428	0.24%	15.72%	0.7303	0.16%	26.97%	0.6530	0.33%	34.70%	0.6038	0.20%	39.62%	0.3979	0.23%	60.21%
	1.29	0.8048	0.17%	19.52%	0.6854	0.16%	31.46%	0.6227	0.22%	37.73%	0.3878	0.17%	61.22%	0.2968	0.35%	70.32%
	1.50	0.7852	0.13%	21.48%	0.6580	0.10%	34.20%	0.5236	0.13%	47.64%	0.3259	0.13%	67.41%	0.2494	0.15%	75.06%
	2.00	0.7363	0.15%	26.37%	0.6140	0.32%	38.60%	0.3295	0.09%	67.05%	0.2335	0.32%	76.65%	0.1641	0.18%	83.59%
	2.49	0.6936	0.07%	30.64%	0.4144	0.12%	58.56%	0.2594	0.21%	74.06%	0.1698	0.12%	83.02%	0.1097	0.27%	89.03%
silicon	1.00	0.7722	0.20%	22.78%	0.6701	0.34%	32.99%	0.2973	0.28%	70.27%	0.2195	0.21%	78.05%	0.1787	0.36%	82.13%
	1.29	0.7432	0.16%	25.68%	0.4642	0.18%	53.58%	0.2284	0.26%	77.16%	0.1765	0.20%	82.35%	0.1410	0.35%	85.90%
	1.50	0.7411	0.27%	25.89%	0.2996	0.25%	70.04%	0.2015	0.41%	79.85%	0.1542	0.20%	84.58%	0.1186	0.23%	88.14%
	2.00	0.6701	0.21%	32.99%	0.2251	0.12%	77.49%	0.1561	0.14%	84.39%	0.1111	0.15%	88.89%	0.0782	0.26%	92.18%
	2.49	0.5036	0.31%	49.64%	0.1871	0.29%	81.29%	0.1233	0.28%	87.67%	0.0805	0.15%	91.95%	0.0522	0.44%	94.78%
iron	1.29	0.4896	0.23%	51.04%	0.1107	0.32%	88.93%	0.0865	0.33%	91.35%	0.0696	0.38%	93.04%	0.0565	0.50%	94.35%
	2.49	0.1141	0.34%	88.59%	0.0737	0.59%	92.63%	0.0503	0.39%	94.97%	0.0336	0.28%	96.64%	0.0221	0.36%	97.79%

Table F.2: Effect of the density for 740 MeV neutron and 1 GeV proton, helium, carbon, oxygen, silicon and iron beams on the dose reduction of an MGS-1 shield with a thickness range of 120-200 cm. D_{norm} is the normalized dose, $E_{D_{norm}}$ is the error of the normalized dose and δD is the dose reduction.

Particle	Density [g/cm ³]	Shield thickness														
		120 cm			140 cm			160 cm			180 cm			200 cm		
		D_{norm}	$E_{D_{norm}}$	δD	D_{norm}	$E_{D_{norm}}$	δD	D_{norm}	$E_{D_{norm}}$	δD	D_{norm}	$E_{D_{norm}}$	δD	D_{norm}	$E_{D_{norm}}$	δD
neutron	1.00	1.6611	2.00%	-66.11%	1.5242	2.11%	-52.42%	1.3561	2.20%	-35.61%	1.2228	2.18%	-22.28%	1.0878	2.10%	-8.78%
	1.29	1.4783	2.01%	-47.83%	1.2833	2.03%	-28.33%	1.1105	1.96%	-11.05%	0.9783	2.12%	2.17%	0.8072	2.72%	19.28%
	1.50	1.3362	2.08%	-33.62%	1.1417	1.95%	-14.17%	0.9575	2.17%	4.25%	0.7850	2.00%	21.50%	0.6460	2.64%	35.40%
	2.00	1.0080	1.95%	-0.80%	0.7903	1.98%	20.97%	0.6166	2.59%	38.34%	0.4823	2.25%	51.77%	0.3619	2.63%	63.81%
	2.49	0.7409	1.94%	25.91%	0.5457	2.33%	45.43%	0.4058	2.40%	59.42%	0.2864	2.44%	71.36%	0.2016	2.50%	79.84%
proton	1.00	0.9285	0.59%	7.15%	0.8351	0.62%	16.49%	0.7152	0.68%	28.48%	0.6216	0.80%	37.84%	0.5256	0.56%	47.44%
	1.29	0.7630	0.78%	23.70%	0.6404	0.77%	35.96%	0.5200	0.71%	48.00%	0.4200	0.80%	58.00%	0.3286	1.46%	67.14%
	1.50	0.6530	0.51%	34.70%	0.5158	0.48%	48.42%	0.4036	1.21%	59.64%	0.3006	0.92%	69.94%	0.2276	1.29%	77.24%
	2.00	0.4118	0.54%	58.82%	0.2948	1.24%	70.52%	0.1951	1.04%	80.49%	0.1312	1.15%	86.88%	0.0452	2.42%	95.48%
	2.49	0.2517	1.05%	74.83%	0.1503	1.06%	84.97%	0.0515	1.36%	94.85%	0.0335	1.60%	96.65%	0.0209	2.32%	97.91%
helium	1.00	0.0203	1.25%	97.97%	0.0155	1.08%	98.45%	0.0125	2.94%	98.75%	0.0101	1.87%	98.99%	0.0079	1.21%	99.21%
	1.29	0.0150	0.76%	98.50%	0.0116	1.91%	98.84%	0.0087	1.90%	99.13%	0.0066	1.90%	99.34%	0.0051	2.47%	99.49%
	1.50	0.0121	0.68%	98.79%	0.0093	1.32%	99.07%	0.0069	1.45%	99.31%	0.0050	1.16%	99.50%	0.0037	1.74%	99.63%
	2.00	0.0084	1.77%	99.16%	0.0055	1.55%	99.45%	0.0036	2.22%	99.64%	0.0025	3.57%	99.75%	0.0017	2.58%	99.83%
	2.49	0.0051	3.87%	99.49%	0.0031	2.92%	99.69%	0.0020	2.54%	99.80%	0.0012	3.85%	99.88%	0.0007	7.02%	99.93%
carbon	1.00	0.4992	0.32%	50.08%	0.3801	0.20%	61.99%	0.3114	0.22%	68.86%	0.2581	0.17%	74.19%	0.2107	0.21%	78.93%
	1.29	0.3409	0.14%	65.91%	0.2704	0.27%	72.96%	0.2114	0.22%	78.86%	0.1640	0.42%	83.60%	0.1267	0.33%	87.33%
	1.50	0.2767	0.35%	72.33%	0.2111	0.31%	78.89%	0.1593	0.43%	84.07%	0.1183	0.33%	88.17%	0.0873	0.55%	91.27%
	2.00	0.1691	0.17%	83.09%	0.1169	0.45%	88.31%	0.0810	0.42%	91.90%	0.0571	0.44%	94.29%	0.0397	0.44%	96.03%
	2.49	0.1033	0.30%	89.67%	0.0672	0.41%	93.28%	0.0445	0.57%	95.55%	0.0297	0.97%	97.03%	0.0201	0.86%	97.99%
oxygen	1.00	0.3146	0.24%	68.54%	0.2596	0.12%	74.04%	0.2145	0.20%	78.55%	0.1757	0.27%	82.43%	0.1435	0.24%	85.65%
	1.29	0.2356	0.25%	76.44%	0.1845	0.18%	81.55%	0.1439	0.13%	85.61%	0.1104	0.34%	88.96%	0.0851	0.34%	91.49%
	1.50	0.1902	0.25%	80.98%	0.1449	0.26%	85.51%	0.1079	0.55%	89.21%	0.0804	0.19%	91.96%	0.0596	0.29%	94.04%
	2.00	0.1144	0.52%	88.56%	0.0793	0.33%	92.07%	0.0555	0.45%	94.45%	0.0387	0.47%	96.13%	0.0271	0.46%	97.29%
	2.49	0.0706	0.40%	92.94%	0.0464	0.45%	95.36%	0.0305	0.39%	96.95%	0.0207	0.62%	97.93%	0.0137	0.62%	98.63%
silicon	1.00	0.1485	0.23%	85.15%	0.1228	0.34%	87.72%	0.1009	0.15%	89.91%	0.0828	0.35%	91.72%	0.0664	0.35%	93.36%
	1.29	0.1107	0.18%	88.93%	0.0870	0.35%	91.30%	0.0678	0.23%	93.22%	0.0523	0.20%	94.77%	0.0399	0.45%	96.01%
	1.50	0.0902	0.61%	90.98%	0.0679	0.26%	93.21%	0.0507	0.38%	94.93%	0.0377	0.42%	96.23%	0.0285	0.22%	97.15%
	2.00	0.0547	0.40%	94.53%	0.0379	0.33%	96.21%	0.0265	0.48%	97.35%	0.0187	0.40%	98.13%	0.0133	0.58%	98.67%
	2.49	0.0341	0.34%	96.59%	0.0225	0.31%	97.75%	0.0149	0.31%	98.51%	0.0098	0.71%	99.02%	0.0067	0.42%	99.33%
iron	1.29	0.0448	0.49%	95.52%	0.0355	0.25%	96.45%	0.0279	0.43%	97.21%	0.0216	0.59%	97.84%	0.0170	0.30%	98.30%
	2.49	0.0148	0.43%	98.52%	0.0099	0.32%	99.01%	0.0066	0.19%	99.34%	0.0044	0.60%	99.56%	0.0030	0.37%	99.70%

Table F.3: Effect of the density for 740 MeV neutron and 1 GeV proton, helium, carbon, oxygen, silicon and iron beams on the dose reduction of an MGS-1 shield with a thickness range of 220-300 cm. D_{norm} is the normalized dose, $E_{D_{norm}}$ is the error of the normalized dose and δD is the dose reduction.

Particle	Density [g/cm ³]	Shield thickness														
		220 cm			240 cm			260 cm			280 cm			300 cm		
		D_{norm}	$E_{D_{norm}}$	δD	D_{norm}	$E_{D_{norm}}$	δD	D_{norm}	$E_{D_{norm}}$	δD	D_{norm}	$E_{D_{norm}}$	δD	D_{norm}	$E_{D_{norm}}$	δD
neutron	1.00	0.9590	1.96%	4.10%	0.8363	2.24%	16.37%	0.7128	2.00%	28.72%	0.6267	2.06%	37.33%	0.5295	1.97%	47.05%
	1.29	0.6766	1.92%	32.34%	0.5558	2.17%	44.42%	0.4611	2.56%	53.89%	0.3906	2.25%	60.94%	0.3210	2.23%	67.90%
	1.50	0.5152	2.29%	48.48%	0.4173	2.47%	58.27%	0.3267	2.32%	67.33%	0.2604	2.34%	73.96%	0.2072	2.06%	79.28%
	2.00	0.2685	2.21%	73.15%	0.2002	2.20%	79.98%	0.1486	3.43%	85.14%	0.1130	2.67%	88.70%	0.0809	2.31%	91.91%
	2.49	0.1411	3.11%	85.89%	0.0931	2.57%	90.69%	0.0681	3.46%	93.19%	0.0467	4.89%	95.33%	0.0318	5.32%	96.82%
proton	1.00	0.4479	0.52%	55.21%	0.3662	1.06%	63.38%	0.3069	1.08%	69.31%	0.2494	1.30%	75.06%	0.2055	1.04%	79.45%
	1.29	0.2615	1.06%	73.85%	0.1997	1.27%	80.03%	0.1461	1.45%	85.39%	0.1105	0.67%	88.95%	0.0598	1.42%	94.02%
	1.50	0.1663	1.54%	83.37%	0.1169	0.73%	88.31%	0.0543	1.51%	94.57%	0.0295	0.85%	97.05%	0.0227	3.63%	97.73%
	2.00	0.0310	1.04%	96.90%	0.0209	2.26%	97.91%	0.0155	2.24%	98.45%	0.0102	3.79%	98.98%	0.0065	6.41%	99.35%
	2.49	0.0139	3.41%	98.61%	0.0089	4.51%	99.11%	0.0058	5.77%	99.42%	0.0040	4.33%	99.60%	0.0028	5.02%	99.72%
helium	1.00	0.0063	2.02%	99.37%	0.0047	2.51%	99.53%	0.0038	1.79%	99.62%	0.0030	4.83%	99.70%	0.0026	4.20%	99.74%
	1.29	0.0039	2.91%	99.61%	0.0029	2.02%	99.71%	0.0021	2.85%	99.79%	0.0017	2.73%	99.83%	0.0012	9.11%	99.88%
	1.50	0.0027	2.15%	99.73%	0.0020	4.50%	99.80%	0.0013	2.80%	99.87%	0.0010	3.33%	99.90%	0.0007	12.96%	99.93%
	2.00	0.0011	5.30%	99.89%	0.0009	3.72%	99.91%	0.0005	3.32%	99.95%	0.0004	10.06%	99.96%	0.0002	6.03%	99.98%
	2.49	0.0005	6.73%	99.95%	0.0003	10.19%	99.97%	0.0002	12.40%	99.98%	0.0001	19.53%	99.99%	0.0001	11.01%	99.99%
carbon	1.00	0.1717	0.35%	82.83%	0.1386	0.26%	86.14%	0.1112	0.34%	88.88%	0.0888	0.39%	91.12%	0.0708	0.27%	92.92%
	1.29	0.0969	0.40%	90.31%	0.0740	0.41%	92.60%	0.0568	0.31%	94.32%	0.0437	0.72%	95.63%	0.0336	0.84%	96.64%
	1.50	0.0652	0.19%	93.48%	0.0483	0.45%	95.17%	0.0365	0.84%	96.35%	0.0278	0.47%	97.22%	0.0207	1.12%	97.93%
	2.00	0.0278	0.42%	97.22%	0.0202	0.54%	97.98%	0.0144	0.70%	98.56%	0.0102	0.83%	98.98%	0.0073	2.16%	99.27%
	2.49	0.0136	1.26%	98.64%	0.0090	1.05%	99.10%	0.0062	1.29%	99.38%	0.0040	2.71%	99.60%	0.0026	1.71%	99.74%
oxygen	1.00	0.1158	0.06%	88.42%	0.0931	0.39%	90.69%	0.0739	0.47%	92.61%	0.0595	0.30%	94.05%	0.0477	0.68%	95.23%
	1.29	0.0657	0.31%	93.43%	0.0499	0.25%	95.01%	0.0383	0.29%	96.17%	0.0294	0.62%	97.06%	0.0228	0.65%	97.72%
	1.50	0.0443	0.39%	95.57%	0.0331	0.58%	96.69%	0.0248	0.75%	97.52%	0.0189	0.25%	98.11%	0.0141	1.28%	98.59%
	2.00	0.0193	0.63%	98.07%	0.0140	0.73%	98.60%	0.0097	0.62%	99.03%	0.0070	0.71%	99.30%	0.0049	0.95%	99.51%
	2.49	0.0093	0.41%	99.07%	0.0062	0.61%	99.38%	0.0042	0.79%	99.58%	0.0028	1.40%	99.72%	0.0018	1.37%	99.82%
silicon	1.00	0.0541	0.17%	94.59%	0.0432	0.41%	95.68%	0.0345	0.34%	96.55%	0.0277	0.39%	97.23%	0.0222	0.50%	97.78%
	1.29	0.0311	0.32%	96.89%	0.0236	0.72%	97.64%	0.0183	0.34%	98.17%	0.0141	1.08%	98.59%	0.0108	0.42%	98.92%
	1.50	0.0212	0.70%	97.88%	0.0159	0.59%	98.41%	0.0119	0.65%	98.81%	0.0091	0.42%	99.09%	0.0069	0.50%	99.31%
	2.00	0.0093	0.31%	99.07%	0.0067	0.42%	99.33%	0.0048	0.65%	99.52%	0.0034	0.45%	99.66%	0.0025	1.16%	99.75%
	2.49	0.0045	0.54%	99.55%	0.0029	1.19%	99.71%	0.0020	1.09%	99.80%	0.0013	1.43%	99.87%	0.0009	1.81%	99.91%
iron	1.29	0.0133	0.75%	98.67%	0.0102	0.39%	98.98%	0.0080	0.67%	99.20%	0.0063	0.46%	99.37%	0.0048	0.93%	99.52%
	2.49	0.0020	0.74%	99.80%	0.0014	0.91%	99.86%	0.0009	0.58%	99.91%	0.0006	1.06%	99.94%	0.0004	1.82%	99.96%

Table F.4: Effect of the density for 740 MeV neutron and 1 GeV proton, helium, carbon, oxygen, silicon and iron beams on the dose reduction of an MGS-1 shield with a thickness range of 320-400 cm. D_{norm} is the normalized dose, $E_{D_{norm}}$ is the error of the normalized dose and δD is the dose reduction.

Particle	Density [g/cm ³]	Shield thickness														
		320 cm			340 cm			360 cm			380 cm			400 cm		
		D_{norm}	$E_{D_{norm}}$	δD	D_{norm}	$E_{D_{norm}}$	δD	D_{norm}	$E_{D_{norm}}$	δD	D_{norm}	$E_{D_{norm}}$	δD	D_{norm}	$E_{D_{norm}}$	δD
neutron	1.00	0.4369	1.93%	56.31%	0.3768	2.64%	62.32%	0.3352	2.56%	66.48%	0.2834	1.97%	71.66%	0.2341	2.59%	76.59%
	1.29	0.2564	2.32%	74.36%	0.2031	3.59%	79.69%	0.1668	3.01%	83.32%	0.1421	2.58%	85.79%	0.1156	2.90%	88.44%
	1.50	0.1666	3.05%	83.34%	0.1330	3.61%	86.70%	0.1005	2.57%	89.95%	0.0749	3.60%	92.51%	0.0651	3.76%	93.49%
	2.00	0.0582	3.69%	94.18%	0.0442	4.64%	95.58%	0.0320	2.56%	96.80%	0.0236	6.20%	97.64%	0.0159	8.08%	98.41%
	2.49	0.0205	4.64%	97.95%	0.0140	9.48%	98.60%	0.0089	7.14%	99.11%	0.0058	5.19%	99.42%	0.0030	16.74%	99.70%
proton	1.00	0.1645	1.43%	83.55%	0.1259	1.22%	87.41%	0.1041	1.79%	89.59%	0.0682	1.60%	93.18%	0.0239	3.73%	97.61%
	1.29	0.0278	2.94%	97.22%	0.0198	1.64%	98.02%	0.0161	2.49%	98.39%	0.0118	4.69%	98.82%	0.0089	2.81%	99.11%
	1.50	0.0160	2.17%	98.40%	0.0120	2.07%	98.80%	0.0091	3.77%	99.09%	0.0067	3.14%	99.33%	0.0045	8.82%	99.55%
	2.00	0.0052	5.84%	99.48%	0.0031	6.10%	99.69%	0.0019	9.38%	99.81%	0.0017	14.24%	99.83%	0.0008	10.32%	99.92%
	2.49	0.0013	8.42%	99.87%	0.0007	11.69%	99.93%	0.0007	21.18%	99.93%	0.0004	32.02%	99.96%	0.0004	27.80%	99.96%
helium	1.00	0.0020	4.80%	99.80%	0.0015	3.51%	99.85%	0.0012	3.65%	99.88%	0.0009	5.67%	99.91%	0.0008	8.10%	99.92%
	1.29	0.0009	3.97%	99.91%	0.0008	7.52%	99.92%	0.0005	6.06%	99.95%	0.0004	14.40%	99.96%	0.0003	8.62%	99.97%
	1.50	0.0005	6.45%	99.95%	0.0005	10.08%	99.95%	0.0003	8.12%	99.97%	0.0002	17.63%	99.98%	0.0002	9.87%	99.98%
	2.00	0.0001	12.12%	99.99%	0.0001	10.72%	99.99%	0.0001	13.38%	99.99%	0.0000	17.12%	100.00%	0.0000	14.78%	100.00%
	2.49	0.0000	25.35%	100.00%	0.0000	10.12%	100.00%	0.0000	24.86%	100.00%	0.0000	33.02%	100.00%	0.0000	44.46%	100.00%
carbon	1.00	0.0568	0.53%	94.32%	0.0452	0.57%	95.48%	0.0362	0.58%	96.38%	0.0289	0.41%	97.11%	0.0234	1.20%	97.66%
	1.29	0.0262	0.75%	97.38%	0.0201	0.78%	97.99%	0.0158	0.86%	98.42%	0.0122	0.91%	98.78%	0.0095	1.13%	99.05%
	1.50	0.0156	0.52%	98.44%	0.0121	1.65%	98.79%	0.0093	1.06%	99.07%	0.0068	0.83%	99.32%	0.0054	1.10%	99.46%
	2.00	0.0052	1.44%	99.48%	0.0037	2.45%	99.63%	0.0027	1.34%	99.73%	0.0018	3.38%	99.82%	0.0013	2.25%	99.87%
	2.49	0.0017	2.56%	99.83%	0.0011	2.40%	99.89%	0.0008	4.42%	99.92%	0.0005	6.10%	99.95%	0.0003	2.73%	99.97%
oxygen	1.00	0.0379	0.79%	96.21%	0.0305	0.46%	96.95%	0.0240	0.40%	97.60%	0.0193	0.33%	98.07%	0.0155	1.19%	98.45%
	1.29	0.0178	0.15%	98.22%	0.0136	1.19%	98.64%	0.0108	0.43%	98.92%	0.0083	0.75%	99.17%	0.0063	0.44%	99.37%
	1.50	0.0109	0.95%	98.91%	0.0081	0.98%	99.19%	0.0063	0.59%	99.37%	0.0048	1.05%	99.52%	0.0036	1.63%	99.64%
	2.00	0.0035	2.19%	99.65%	0.0025	1.08%	99.75%	0.0018	2.38%	99.82%	0.0012	3.32%	99.88%	0.0009	3.17%	99.91%
	2.49	0.0012	2.39%	99.88%	0.0008	1.97%	99.92%	0.0005	1.21%	99.95%	0.0003	3.22%	99.97%	0.0002	4.37%	99.98%
silicon	1.00	0.0176	0.56%	98.24%	0.0140	0.72%	98.60%	0.0114	0.58%	98.86%	0.0092	0.45%	99.08%	0.0073	0.67%	99.27%
	1.29	0.0085	0.88%	99.15%	0.0066	0.30%	99.34%	0.0052	0.82%	99.48%	0.0040	1.01%	99.60%	0.0032	0.84%	99.68%
	1.50	0.0052	0.62%	99.48%	0.0040	0.57%	99.60%	0.0030	1.23%	99.70%	0.0023	1.11%	99.77%	0.0017	1.54%	99.83%
	2.00	0.0017	1.09%	99.83%	0.0012	0.71%	99.88%	0.0008	2.18%	99.92%	0.0006	0.99%	99.94%	0.0004	1.87%	99.96%
	2.49	0.0006	1.30%	99.94%	0.0004	3.21%	99.96%	0.0002	3.05%	99.98%	0.0002	1.51%	99.98%	0.0001	3.86%	99.99%
iron	1.29	0.0038	0.53%	99.62%	0.0030	0.23%	99.70%	0.0023	0.71%	99.77%	0.0019	0.77%	99.81%	0.0015	0.96%	99.85%
	2.49	0.0003	0.85%	99.97%	0.0002	1.07%	99.98%	0.0001	1.90%	99.99%	0.0001	2.91%	99.99%	0.0000	3.09%	100.00%

Bibliography

- [1] ESA. *Earth's protective shield*. 2014. URL: https://www.esa.int/ESA_Multimedia/Images/2014/02/Earth_s_protective_shield.
- [2] NASA. *OLTARIS: On-Line Tool for the Assessment of Radiation in Space*. Tech. rep. July 2010. URL: <https://oltaris.nasa.gov/links>.
- [3] M. Durante and F.A. Cucinotta. "Physical basis of radiation protection in space travel". In: *Reviews of Modern Physics* 83.4 (2011), pp. 1245–1281. DOI: 10.1103/revmodphys.83.1245.
- [4] N. Schetakis et al. "Overview of the main radiation transport codes". In: *Geoscientific Instrumentation, Methods and Data Systems* 9.2 (2020), pp. 407–415. DOI: 10.5194/gi-9-407-2020. URL: <https://gi.copernicus.org/articles/9/407/2020/>.
- [5] Brookhaven National Laboratory. *NSRL User Guide*. URL: <https://www.bnl.gov/nsrl/userguide/bragg-curves-and-peaks.php>.
- [6] V. Vlachoudis. *flair for FLUKA*. Tech. rep. 0.7. Sept. 2008. URL: http://www.fluka.org/web_archive/earchive/new-fluka-discuss/att-8425/flair.pdf.
- [7] A. Ferrari et al. *Fluka: a multi-particle transport code*. Tech. rep. May 2021. URL: <http://www.fluka.org/content/manuals/FM.pdf>.
- [8] M. Isachenkov et al. "Regolith-based additive manufacturing for sustainable development of lunar infrastructure – An overview". In: *Acta Astronautica* 180 (2021), pp. 650–678. DOI: 10.1016/j.actaastro.2021.01.005.
- [9] M Naser. "Extraterrestrial construction materials". In: *Progress in Materials Science* 105 (2019), p. 100577. DOI: 10.1016/j.pmatsci.2019.100577.
- [10] G. Cesaretti et al. "Building components for an outpost on the Lunar soil by means of a novel 3D printing technology". In: *Acta Astronautica* 93 (2014), pp. 430–450. DOI: 10.1016/j.actaastro.2013.07.034.
- [11] N. Kalapodis, G. Kampas, and O.J. Ktenidou. "A review towards the design of extraterrestrial structures: From regolith to human outposts". In: *Acta Astronautica* 175 (2020), pp. 540–569. DOI: 10.1016/j.actaastro.2020.05.038.
- [12] N. Leach. "3D Printing in Space". In: *Architectural Design* 84.6 (2014), pp. 108–113. DOI: 10.1002/ad.1840.
- [13] AI SpaceFactory. *AI SpaceFactory Builds 3D Printed Mars Prototype for NASA*. Feb. 2019. URL: https://www.archdaily.com/910764/ai-spacefactory-builds-3d-printed-mars-prototype-for-nasa?ad_medium=gallery.
- [14] NASA. *Overview: In-Situ Resource Utilization*. Apr. 2020. URL: <https://www.nasa.gov/isru/overview>.
- [15] 3devo. *3devo Precision 350*. 2021. URL: <https://all3dp.com/2/best-filament-extruder-maker-diy-buy/>.
- [16] *Spaceship EAC: 3D printing with lunar dust*. Mar. 2021. URL: <https://blogs.esa.int/exploration/spaceship-eac-3d-printing-with-lunar-dust/>.
- [17] Celanese. *Celanese Vectra® A950 datasheet*. Tech. rep. 2014. URL: <https://www.campusplastics.com/campus/en/datasheet/VECTRA+A950/Ticona/163/268267e7>.
- [18] David Karl et al. "Sintering of ceramics for clay in situ resource utilization on Mars". In: *Open Ceramics* 3 (2020), p. 100008. DOI: 10.1016/j.oceram.2020.100008.
- [19] M. Vuolo et al. "Exploring innovative radiation shielding approaches in space: A material and design study for a wearable radiation protection spacesuit". In: *Life Sciences in Space Research* 15 (2017), pp. 69–78. DOI: 10.1016/j.lssr.2017.08.003.
- [20] Lawrence H. Heilbronn et al. "Neutron yields and effective doses produced by Galactic Cosmic Ray interactions in shielded environments in space". In: *Life Sciences in Space Research* 7 (2015), pp. 90–99. DOI: 10.1016/j.lssr.2015.10.005.
- [21] ExolithLab. *MGS-1 Mars Global Simulant | Fact Sheet*. 2020. URL: <https://cdn.shopify.com/s/files/1/0398/9268/0862/files/mgs-1-spec-sheet-Nov2021.pdf?v=1637075679>.